

UNIVERSITY OF SHEFFIELD

**3D ultimate limit state analysis using
discontinuity layout optimization**

by

Samuel John Hawksbee

A thesis submitted in partial fulfillment for the
degree of Doctor of Philosophy

in the
Department of Civil and Structural Engineering

December 2012

Declaration of Authorship

I, Samuel John Hawksbee, declare that this thesis entitled, '3D ultimate limit state analysis using discontinuity layout optimization' and the work presented in it are my own. Where information has been derived from other sources, I confirm that this has been indicated in the thesis.

Signed:

Date:

SUMMARY

3D ultimate limit state analysis using discontinuity layout optimization

The recently developed discontinuity layout optimization (DLO) procedure uses limit analysis theory to directly obtain upper bounds on plane strain collapse loads of bodies and has successfully been applied to geotechnical problems. In this thesis, a new three-dimensional formulation of DLO is described. The new formulation is capable of directly estimating the collapse load of bodies involving Tresca and Mohr-Coulomb yield criteria, using efficient second order cone programming. The new formulation can be stated in kinematic, energy balance form or static, equilibrium form. The derivation from first principles of both kinematic and equilibrium forms is described, allowing full conceptualization of the DLO procedure. A number of simple benchmark problems are considered, demonstrating that good results can be obtained using the new formulation even when very coarse numerical discretisations are employed. The best reported upper bound for the compression of a purely cohesive block between two perfectly rough platens was improved upon.

In DLO, the yield condition is only checked on predefined discontinuities, used to discretize the problem. Consequently, the estimated collapse loads are greater than the ‘exact’ collapse load (*i.e.* they are ‘unsafe’). New methods generating continuous stress fields from discontinuous DLO solutions are developed based on the plane strain and three-dimensional equilibrium forms of DLO. These new fields are discretized in plane strain and three-dimensions using solid triangular and tetrahedral elements, respectively. The stress fields are explained in the context of determining alternative ‘lower bound’ forms of solution. An alternative method determining a continuum stress field directly (*i.e.* not from a DLO solution) was also developed.

Acknowledgements

I would like to thank all those who have helped me undertake the research presented in this thesis. I would particularly like to thank my supervisors, Matthew Gilbert and Colin Smith, for the invaluable guidance, support and encouragement throughout the various stages of this work. I would also like to thank members of the Computational Mechanics & Design and Geotechnical Engineering research groups for their companionship and friendship over the last few years.

I would like to thank my friends and family for their support and encouragement over so many years. In particular my parents who supported me through school and university, allowing me the opportunity to undertake this research. I would like thank my wife, Flora, for loving encouragement particularly through the writing process. I would also like to thank my church family particularly my Bible study group for their pray and support.

I would also like to acknowledge the financial support of the University of Sheffield.

Contents

Declaration of Authorship	iii
Summary	v
Acknowledgements	vii
List of Figures	xv
List of Tables	xix
1 Introduction	1
1.1 Background	1
1.2 Aims of research	3
1.3 Outline of thesis	4
2 Literature review	7
2.1 Introduction	7
2.2 Limit analysis	7
2.2.1 Introduction	7
2.2.2 Assumptions	8
2.2.3 Upper bound	10
2.2.4 Lower bound	11
2.3 Mathematical optimization	13
2.4 Direct methods	17
2.4.1 Introduction	17
2.4.2 Trial and error	18
2.4.3 Method of characteristics	19
2.4.4 Numerical methods	19
2.4.4.1 Introduction	19

2.4.4.2	Continuous methods	20
2.4.4.3	Hybrid	21
2.4.4.4	Discontinuous	22
2.5	Finite element limit analysis	24
2.5.1	Introduction	24
2.5.2	Volumetric locking	25
2.5.3	Enhancements	25
2.5.4	Optimization	27
2.6	Discontinuity layout optimization	28
2.6.1	Introduction	28
2.6.2	Kinematic formulation	29
2.6.2.1	Introduction	29
2.6.2.2	Compatibility	30
2.6.2.3	Flow rule and energy dissipation	32
2.6.2.4	Specification of loads	33
2.6.3	Equilibrium formulation	35
2.6.3.1	Adaptive nodal connection procedure	36
2.7	Three-dimensional limit analysis benchmarks	38
2.7.1	Introduction	38
2.7.2	Bearing capacity	39
2.7.3	Compression of a block	40
2.7.4	Anchors	41
2.7.5	Slopes	43
2.7.6	Summary	43
2.8	Conclusions	44
3	Application of discontinuity layout optimization to three-dimensional plasticity problems	47
3.1	Yield condition on three-dimensional discontinuities	48
3.2	Three-dimensional formulation of DLO	49
3.2.1	Compatibility	50
3.2.2	Flow rule	52
3.2.3	Dissipation function	52
3.2.4	Mathematical formulation	53
3.2.5	Boundary conditions and loads	54
3.2.6	Summary of procedure	55
3.3	Numerical Examples	56
3.3.1	Compression of a block	57
3.3.2	Punch indentation	58

3.3.3	Anchor in a purely cohesive soil ($\phi = 0$)	61
3.3.4	Anchor in a purely frictional soil	63
3.4	Discussion	65
3.5	Conclusions	65
4	Plane strain stress functions	67
4.1	Introduction	67
4.2	Background	68
4.2.1	Equilibrium equations	68
4.2.2	Translational equilibrium	68
4.2.3	Stress functions	71
4.3	Derivation of DLO equilibrium formulation	71
4.3.1	Translational stress functions	72
4.3.2	Integral form	74
4.3.3	Applying loads	76
4.3.4	Internal forces on a path	81
4.3.5	Enforcing the Mohr-Coulomb yield condition on a path	83
4.3.6	Discretization	84
4.3.7	Discussion	84
4.4	Pseudo lower bounds	85
4.4.1	Method I	88
4.4.2	Method II	89
4.5	Numerical examples	91
4.5.1	Compression of a block	93
4.5.2	Prandtl problem	93
4.5.3	Discussion	104
4.5.3.1	Method I	104
4.5.3.2	Method II	106
4.6	Conclusions	107
5	Three-dimensional stress functions	109
5.1	Introduction	109
5.2	Background	110
5.2.1	Equilibrium equations	110
5.2.2	Translational equilibrium	112
5.2.3	Stress functions	113
5.3	Derivation of DLO equilibrium formulation	114
5.3.1	Translational stress functions	114
5.3.2	Integral form	115
5.3.3	Application of loads	118

5.3.4	Internal forces on a surface	121
5.3.5	Enforcing the Mohr-Coulomb yield condition on a surface . .	124
5.3.6	Discretization	125
5.3.7	Discussion	125
5.4	Pseudo lower bound	127
5.5	Numerical Example	130
5.5.1	Results	131
5.5.2	Discussion	132
5.6	Conclusion	132
6	Discussion	135
6.1	Introduction	135
6.2	Equilibrium formulation of DLO and adaptive procedures	138
6.3	Potential enhancements	140
6.3.1	Introduction	140
6.3.2	Improving optimizer performance	140
6.3.3	Alternative adaptive procedures	141
6.3.4	Decomposition	142
6.4	Pseudo lower bounds	145
6.5	Rotations	145
7	Conclusions and future work	147
7.1	Introduction	147
7.2	Conclusions	147
7.3	Suggestions for future work	149
A	Sign convention for jumps in displacement	159
B	Sign convention for compatibility	161
C	Crossovers & Overlaps	163
C.1	Crossovers	163
C.2	Overlaps	163
D	Vector Calculus	167
D.1	Introduction	167
D.1.1	Two dimensional differential operators	168
D.1.2	Three dimensional differential operators	168

D.1.3	Vector calculus theorems	169
D.1.3.1	Gradient theorem	169
D.1.3.2	Stokes' theorem	170
D.1.3.3	Gauss's theorem	170
D.1.3.4	Miscellaneous relationships	171
E	Applying loads using functions \mathbf{P}^x and \mathbf{P}^y	173
E.1	Introduction	173
E.2	Loads applied to internal boundaries	173
E.3	Loads applied to external boundaries	177
E.4	Body forces	177

List of Figures

1.1	Rigid-plastic material model versus real soil behaviour	2
1.2	Pipeline and berm problem – LimitState:GEO 3.0 solution	3
2.1	Body forces g acting on a body M with applied loads f acting on boundary A_f and fixed displacements on boundary A_u	8
2.2	Plane strain Mohr-Coulomb yield condition and associated flow rule	9
2.3	Three-dimensional yield criteria	14
2.4	Comparison of RFEM and DLO using a simple example	24
2.5	Simple example illustrating the decompositional procedure of Pas- tor et al. (2009).	27
2.6	Stages in DLO procedure	29
2.7	Compatibility at a node	31
2.8	Compatibility at a ‘crossover’ point	32
2.9	Summation of dead loads	35
2.10	Relationship between discontinuity forces and equivalent nodal forces for a simple problem	37
2.11	Compression of a block – relative dimensions	41
2.12	Lower bounds from Merifield et al. (2003) on the break-out factor N_{0c} for a square anchor in a weightless cohesive soil	42
2.13	Break-out factors N_γ for a square anchor in a frictional soil	43
3.1	Mohr-Coloumb yield criteria on three-dimensional discontinuity . .	49
3.2	Solid bodies meeting at a common edge	51
3.3	Compression of a block – problem geometry	58
3.4	Compression of a block – typical failure mechanism	59
3.5	Punch indentation – problem geometry	60
3.6	Representative failure mechanism for a square punch indenter . . .	61
3.7	Anchor – problem geometry	62
3.8	Anchor in cohesive soil - break-out factors	63
3.9	Break-out factors for a square anchor in frictional soil	64

4.1	Sign convention: plane strain stress components	69
4.2	Coulomb wedge for a cohesive soil behind a smooth wall	70
4.3	Mohr's circle for a plane strain tensor	70
4.4	Functions ω^x , ε^x , ω^y and ε^y describing body force per unit area	73
4.5	Nodes, paths and regions within a body G	74
4.6	Application of loads f^x and f^y to body ABO	79
4.7	Loads applied to an inclined path AB	80
4.8	Internal forces on a path AB	82
4.9	Uniform distribution of stress across a path	83
4.10	Distribution of stresses exceeding yield locally on a path	85
4.11	Pseudo lower bound mesh and element	87
4.12	Compression of a block – ‘original grid’ and corresponding meshes	96
4.13	Compression of a plate – distribution of violation using method I, prior to scaling	97
4.14	Compression of a plate – proximity to yield on individual elements using method II	97
4.15	Prandtl punch – ‘original grid’ and corresponding meshes	98
4.16	Prandtl punch – distribution of yield violation, prior to scaling, using method I	98
4.17	Prandtl punch – proximity to yield on individual elements using method II	99
4.18	Selected results for Prandtl punch – mesh \tilde{A} for ‘original grid’ of 1,075 nodes	100
4.19	Solution to the Prandtl problem using a simple two block mechanism	105
4.20	Compression of a plate of equal height and width between two rough platens	105
5.1	Sign convention: three-dimensional stress components	111
5.2	Mohr's circles representing a symmetric stresses tensor	112
5.3	Shear stress τ plotted against normal stress σ_n for nonsymmetric tensors	113
5.4	A body U bounded by a closed surface V	116
5.5	A body with load f^y applied to boundary $CEFD$	119
5.6	Load applied to a surface \overrightarrow{ABC}	120
5.7	Internal forces on an arbitrary surface \overrightarrow{ABC}	122
5.8	A tetrahedral element j with vertices A , B , C and D	127
5.9	Solid angles θ_1 and θ_2 describing the inclination of an arbitrary plane with respect to the xy plane	131

6.1	Maximum number of potential discontinuities m_{up} in basic plane strain and three-dimensional DLO formulations	137
6.2	MOSEK v. 6 and Gurobi v. 5 performance for a linear programming slab problem	141
6.3	Plane strain example of decompositional procedure using overlapping regions	143
6.4	Plane strain example of decompositional procedure using master and slave subsets	144
A.1	Sign convention for jumps in displacement	160
C.1	Crossovers	164
C.2	Overlaps	165
E.1	Application of a load to an internal boundary	179
E.2	Body G with length dt and infinitesimal width ds	180
E.3	Application of a load to an external boundary	180
E.4	Application of self-weight to a column of material	181

List of Tables

2.1	Optimization classes enforcing the Mohr-Coulomb yield function . . .	16
2.2	Continuous, discontinuous and hybrid methods by limit analysis status	18
2.3	Applying plain strain flow rule conditions in DLO	33
2.4	Compression of a block – best published bounds	41
3.1	Discontinuity flow rule conditions - applicable constraints and vari- ables	53
3.2	Compression of a $2 \times 2 \times 1$ unit block (as depicted in Figure 3.3) - comparison with benchmark solutions	58
3.3	Compression of a $2 \times 2 \times 1$ unit block (as depicted in Figure 3.3) - use of different nodal grid spacings	59
3.4	Indentation of a 1×1 unit punch (as depicted in Figure 3.5) - comparison with benchmark solutions	60
4.1	Compression of a plate – pseudo lower bound method I	94
4.2	Compression of a plate – pseudo lower bound method II	101
4.3	Prandtl punch – pseudo lower bound method I	102
4.4	Prandtl punch – pseudo lower bound method II	103
5.1	Compression of a block – pseudo lower bounds	132
6.1	Prandtl punch problem – LimitState:GEO 3.0 results	135

1 Introduction

1.1 Background

In geotechnical design, two design criteria are typically considered: one avoiding collapse and the other limiting movements. These criteria are incorporated into modern design codes (such as Eurocode 7) via the ultimate limit state (ULS) and serviceability limit state (SLS). Ideally, these checks might be considered via a single elasto-plastic analysis. Accurate prediction of the collapse load and intermediate soil movements using elasto-plastic analysis requires the determination of numerous parameters due to the complex nature of soil behaviour. Additionally, different partial factors may apply to the different limit states. The elasto-plastic analysis itself is complicated and requires considerable user expertise. Consequently, elasto-plastic analysis is applied in practice only to a small percentage of projects.

Separating ULS and SLS checks allows the use of simplified limit analysis methods to determine collapse loads. In contrast to elasto-plastic analysis, the rigid-plastic material model assumed in limit analysis and shown in Figure 1.1 only requires strength parameters, readily determined from conventional shearbox and triaxial testing. The upper and lower bound theorems of limit analysis can be used to bound the collapse load directly, without intermediate steps. Relative to elasto-plastic methods, limit analysis allows engineers to be undertake ULS checks in a much more straightforward and efficient manner.

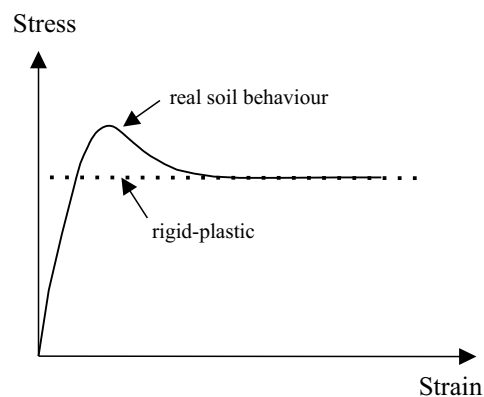


FIGURE 1.1: Rigid-plastic material model versus real soil behaviour

The application of limit analysis to geotechnical engineering dates back to the earth pressure theorems of Coulomb (1776) and Rankine (1857). Early applications consisted of simple hand-based calculations. Chen (1975) provides a comprehensive review of early limit analysis solutions to geotechnical problems. Early research found particular success using the method of characteristics (Sokolovski, 1965); however, this cannot be used to solve three-dimensional problems. Researchers, therefore, had to resort to simple trial and error hand calculations to solve three-dimensional problems. More recently, finite element limit analysis (FELA) has found favour among researchers (Lysmer, 1970; Bottero et al., 1980; Sloan, 1988; Makrodimopoulos and Martin, 2006). However, the quality of FELA solutions is sensitive to mesh layout in the region of stress singularities. Consequently, prior insight into the form of the solutions is required. Alternatively, adaptive refinement techniques maybe employed (Lyamin et al., 2005).

The recently developed discontinuity layout optimization (DLO) determines the critical mechanism from among a large number of potential mechanisms and may be stated in kinematic form or, alternatively, in equilibrium form (Smith and Gilbert, 2007). DLO automates this procedure making use of efficient convex optimization algorithms and is able to handle complex geometries and mechanisms involving thousands of sliding blocks (see Figure 1.2). Unlike FELA, DLO handles stress singularities without any need for tailoring of the mesh or nodal grid. DLO has successfully been implemented in the commercial software package LimitState:GEO (LimitState, 2012) and validated against numerous plane

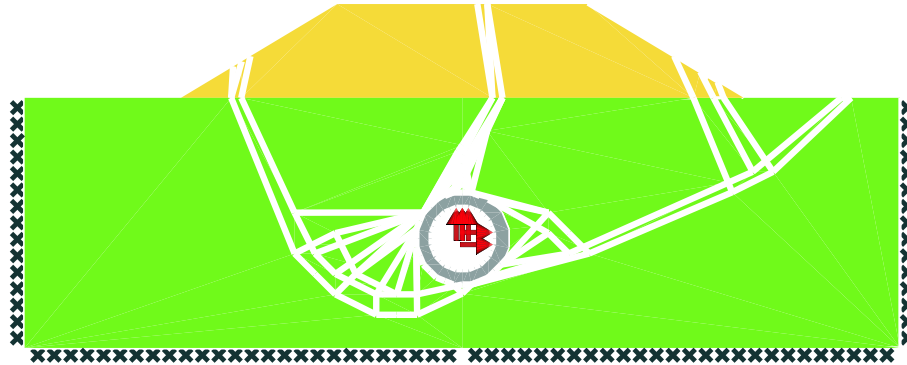


FIGURE 1.2: Pipeline and berm problem – LimitState:GEO 3.0 solution (courtesy of LimitState)

strain benchmarks. Figure 1.2 shows a critical mechanism obtained from LimitState:GEO for a problem involving complex geometry and boundary conditions.

Methods such as FELA can provide both upper and lower bounds on the ‘exact’ solution. DLO, however, can only provide upper bounds on the ‘exact’ limit load. A lower bound equivalent to DLO, retaining its advantages, is also desirable allowing the ‘exact’ limit load to be bracketed and solution accuracy estimated.

To date, the application of limit analysis to three-dimensional problems has been extremely limited. Researchers have focused primarily on three-dimensional FELA. Three-dimensional FELA has been limited by the computation expense involved and only relatively loose bounds have been achieved (Lyamin and Sloan, 2002a,b; Martin and Makrodimopoulos, 2008; Krabbenhøft et al., 2008). Other researchers have used predefined mechanisms to obtain upper bound solutions (Michalowski, 2001; Puzrin and Randolph, 2003; Michalowski and Drescher, 2009). Despite the successful application of DLO to plane strain problems, no three-dimensional formulation of DLO has yet been developed.

1.2 Aims of research

The principal aims of the research described in this thesis are to

-
- (i) develop a kinematic three-dimensional formulation of the DLO procedure;
 - (ii) validate the new three-dimensional formulation against existing benchmarks;
 - (iii) derive the equilibrium formulations of the plane strain and three-dimensional DLO formulations from first principles;
 - (iv) use the plane strain derivation to develop a lower bound type equivalent to plane strain DLO;
 - (v) use the insights, gained from the derivation of a lower bound type equivalent to plane strain DLO, to develop a lower bound type equivalent to the new three-dimensional formulation of DLO.

1.3 Outline of thesis

This thesis contains seven core chapters. This chapter (Chapter 1) provides an introduction as well as brief outline of subsequent chapters.

Chapter 2 provides an overview of the published literature and important fundamental concepts. Firstly, the fundamentals of the upper and lower bound theorems of limit analysis are presented allowing these to be placed in the context of mathematical optimization. Different direct methods of determining the limit load are then reviewed. Particular emphasis will be placed on the treatment of the problem domain as a continuum or discontinuum. A more detailed discussion of the issues involved in finite element limit analysis (FELA) is then presented, followed by an introduction to the fundamentals of the plane strain DLO procedure. Finally, three-dimensional benchmarks will be identified for validating a three-dimensional formulation of DLO.

In Chapter 3, a three-dimensional formulation of the DLO procedure is developed and validated against the benchmarks identified in Chapter 2. Chapter 3 is based on a paper¹ published in the *Proceedings of the Royal Society A*.

In Chapter 4, the dual, equilibrium formulation of the plane strain DLO formulation is derived from first principles using stress functions and vector calculus. Insights gained from this derivation allow the upper bound nature of the equilibrium formulation to be better understood. Finally, relaxed plane strain lower bound methods are developed and tested against benchmark problems.

In Chapter 5, the dual, equilibrium formulation of the new three-dimensional formulation of the DLO procedure is derived from first principles using stress functions and vector calculus. A relaxed lower bound method is then developed and tested against a benchmark problem.

Chapter 6 discusses the broader issues that are raised through the course of the thesis. In particular, computational aspects of the three-dimensional formulation are tackled, including recommendations for future enhancements. Finally, the merits of the relaxed lower bound methods developed in Chapters 4 and 5 are considered.

Chapter 7 summarises the key conclusion of this thesis and recommendations for future work.

¹Hawksbee, S., Smith, C. and Gilbert, M. (2013). “Application of discontinuity layout optimization to three-dimensional plasticity problems”, *Proc. R. Soc. A*, Vol. 469, pp. 1471-2946.

2 Literature review

2.1 Introduction

In the following chapter, the fundamental theorems of limit analysis are introduced and placed in the context of mathematical optimization. Direct methods are then reviewed in the context of these theorems. These methods are reviewed with particular emphasis on their discontinuum/continuum treatment of the problem domain, allowing DLO to be placed within a wider context. More detailed consideration is then given to finite element limit analysis (FELA) before an introduction to the plane strain DLO procedure. Finally, the literature is reviewed in order to identify suitable three-dimensional benchmarks.

2.2 Limit analysis

2.2.1 Introduction

Plastic methods have long been used to estimate the collapse load of geotechnical problems. Plastic methods make use of the simple rigid-plastic material model described in Chapter 1 to directly estimate the collapse load. The rigid-plastic model assumes that elastic strain at failure is insignificant when compared to the total plastic strain, as is the case for many geotechnical problems. Building on earlier plastic theory, Hill (1950) and Drucker et al. (1952) among others developed

a sophisticated theoretical framework, limit analysis, allowing an ‘exact’ collapse load to be bracketed.

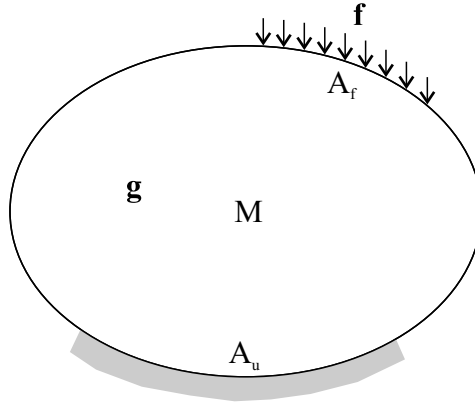


FIGURE 2.1: Body forces g acting on a body M with applied loads f acting on boundary A_f and fixed displacements on boundary A_u

Assume the rigid-plastic body M , shown in Figure 2.1, is at the point of impending plastic collapse; where the velocities $\dot{\mathbf{u}} = 0$ on A_u . Assuming body forces \mathbf{g} act on M and loads \mathbf{f} act on boundary A_f , \mathbf{g} and \mathbf{f} are defined as $\mathbf{g} = \lambda \mathbf{g}_0$ and $\mathbf{f} = \lambda \mathbf{f}_0$; where \mathbf{g}_0 and \mathbf{f}_0 are reference loads and λ is the exact limiting load multiplier. λ is chosen such that stress state on M is at the point of impending collapse. Limit analysis is concerned with bracketing the exact limiting load multiplier λ using the upper and lower bound theorems of limit analysis. The upper bound theorem allows the determination of ‘unsafe’ load multipliers $\lambda^+ \geq \lambda$. The lower bound theorem allows the determination of ‘safe’ load multipliers $\lambda^- \leq \lambda$. The exact limiting load multiplier λ is found when $\lambda^- = \lambda^+$.

2.2.2 Assumptions

The theorems of limit analysis rest on two key assumptions. The first of these states that a material’s yield function $f(\boldsymbol{\sigma}) = 0$, defining when yield occurs, must be convex. Any stress state within the yield function, $f(\boldsymbol{\sigma}) < 0$, is non-yielding and consistent with the rigid-plastic model, no strain will occur. $f(\boldsymbol{\sigma}) > 0$ is an

inaccessible region. Fortunately, the two most commonly used yield functions in geotechnics, the Tresca and Mohr-Coulomb yield functions, are convex.

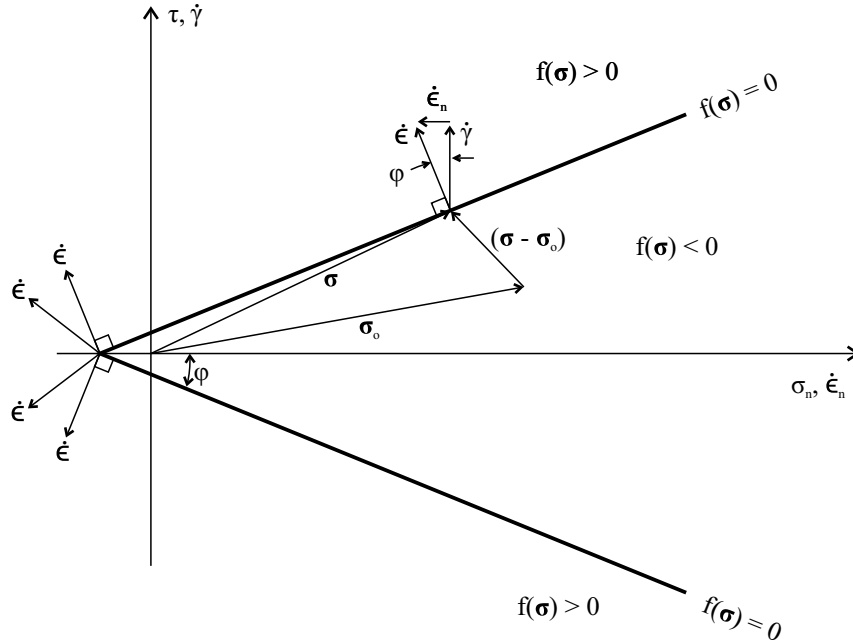


FIGURE 2.2: Plane strain Mohr-Coulomb yield surface and associated flow rule; where $f(\boldsymbol{\sigma}) = 0$ is the yield function; σ_n is the normal stress; τ is the shear stress; $\dot{\boldsymbol{\epsilon}}$ is the plastic strain rate; $\dot{\epsilon}_n$ is the normal component of the strain rate; $\dot{\gamma}$ is the shear component of the strain rate; $\boldsymbol{\sigma}$ is a stress state on the yield surface; and $\boldsymbol{\sigma}_0$ is a non-yielding stress state.

The second key assumption is that the increment of plastic strain $\dot{\boldsymbol{\epsilon}}$ must be normal to the yield surface $f(\boldsymbol{\sigma})$. This is known as the associated flow rule. The associated flow rule is demonstrated for the plane strain Mohr-Coulomb yield surface by Figure 2.2. Singularities, such as at the apex in Figure 2.2, are dealt with by assuming that $\dot{\boldsymbol{\epsilon}}$ must lie between the normals of the two surfaces adjacent to the singularity. The associated flow rule requires that dilation $\dot{\epsilon}_n = \dot{\gamma} \tan \phi$ and implies that shearing resistance is entirely due to dilation. In a real soil, shearing resistance will be due to a number of contributing factors. Consequently, the associated flow rule tends to over-predict dilation. It has, however, been found to produce good results for many geotechnical problems.

As demonstrated in Figure 2.2, it follows from these two assumptions that the angle between $(\boldsymbol{\sigma} - \boldsymbol{\sigma}^0)$ and $\dot{\boldsymbol{\epsilon}}$ must be less than 90° ; where $\boldsymbol{\sigma}$ is any stress state on the yield surface and $\boldsymbol{\sigma}^0$ any non-yielding stress state, $f(\boldsymbol{\sigma}) < 0$. This results in the principle of maximum plastic dissipation

$$(\boldsymbol{\sigma} - \boldsymbol{\sigma}^0) \cdot \dot{\boldsymbol{\epsilon}} \geq 0. \quad (2.1)$$

2.2.3 Upper bound

Before describing the upper bound theorem, it is necessary to define the kinematic and plastic admissibility of a strain rate field $\dot{\boldsymbol{\epsilon}}$ (Le, 2009). $\dot{\boldsymbol{\epsilon}}$ is kinematically admissible, when it satisfies compatibility

$$\dot{\boldsymbol{\epsilon}} = \mathbf{L}\dot{\mathbf{u}} \quad \text{in } M \quad (2.2)$$

and the kinematic boundary conditions

$$\dot{\mathbf{u}} = \mathbf{0} \quad \text{on } A_u; \quad (2.3)$$

where \mathbf{L} is a differential operator

$$\mathbf{L}^T = \begin{bmatrix} \frac{\partial}{\partial x} & 0 & 0 & \frac{\partial}{\partial y} & 0 & \frac{\partial}{\partial z} \\ 0 & \frac{\partial}{\partial y} & 0 & \frac{\partial}{\partial x} & \frac{\partial}{\partial z} & 0 \\ 0 & 0 & \frac{\partial}{\partial z} & 0 & \frac{\partial}{\partial y} & \frac{\partial}{\partial x} \end{bmatrix} \quad (2.4)$$

$\dot{\boldsymbol{\epsilon}}$ is said to be plastically admissible if it satisfies the associated flow rule and the rate of work done by the loads W_{ext} is positive:

$$W_{ext} = \int_M \mathbf{g}_0 \cdot \dot{\mathbf{u}} \, dM + \int_{A_f} \mathbf{f}_0 \cdot \dot{\mathbf{u}} \, dA_f \geq 0. \quad (2.5)$$

The upper bound theorem can now be used to determine a load multiplier λ^+ for a kinematically and plastically admissible strain rate field $\dot{\epsilon}$. From the equation of virtual work, the W_{ext} must equal the internal rate of dissipation D_{int} and

$$\lambda^+ = \frac{D_{int}}{W_{ext}}, \quad (2.6)$$

where

$$D_{int} = \max_{\sigma} \int_M \sigma \cdot \dot{\epsilon} \, dM \quad (2.7)$$

and σ is the stress field on M .

Le (2009) states the upper bound theorem of limit analysis as:

The exact collapse load multiplier λ is the smallest one among all possible kinematic solutions λ^+ corresponding to the set of all kinematically and plastically admissible velocity fields $\dot{\mathbf{u}}$, that is

$$\lambda \leq \lambda^+ \quad (2.8)$$

Therefore, the goal of an upper bound analysis can be written as:

$$\lambda^+ = \min D_{int}$$

subject to

$$\begin{aligned} \dot{\epsilon} &= \mathbf{L}\dot{\mathbf{u}} \quad \text{in } M; \\ \dot{\mathbf{u}} &= \mathbf{0} \quad \text{on } A_u; \\ W_{ext} &= 1. \end{aligned} \quad (2.9)$$

2.2.4 Lower bound

Before describing the lower bound theorem, it is necessary to define the static and plastic admissibility of a stress field σ . σ is statically admissible when it satisfies

the equilibrium equations

$$\mathbf{L} \cdot \boldsymbol{\sigma} = -\lambda^- \mathbf{g}_0 \quad \text{in } M \quad (2.10)$$

and stress boundary conditions

$$\mathbf{n} \cdot \boldsymbol{\sigma} = \lambda^- \mathbf{f}_0 \quad \text{on } A_f; \quad (2.11)$$

where \mathbf{n} is a matrix containing the components of the outward normal vector to M :

$$\mathbf{n} = \begin{bmatrix} n_x & 0 & 0 & n_y & 0 & n_z \\ 0 & n_y & 0 & n_x & n_z & 0 \\ 0 & 0 & n_z & 0 & n_y & n_x \end{bmatrix} \quad (2.12)$$

and λ^- is a statically admissible load multiplier (Le, 2009).

$\boldsymbol{\sigma}$ is plastically admissible when

$$f(\boldsymbol{\sigma}) \leq 0 \quad \text{in } M. \quad (2.13)$$

Assuming a statically and plastically admissible stress field $\boldsymbol{\sigma}$, the lower bound theorem allows load multiplier λ^- to be found from static equilibrium.

Le (2009) states the lower bound theorem of limit analysis as:

The exact collapse load multiplier λ is the largest one among all possible static solutions λ^- corresponding to the set of all statically and plastically admissible stress fields $\boldsymbol{\sigma}$, that is

$$\lambda^- \leq \lambda \quad (2.14)$$

Therefore, the goal of a lower bound analysis is to determine

$$\max \lambda^-$$

subject to

$$\begin{aligned} \mathbf{L} \cdot \boldsymbol{\sigma} &= -\lambda^- \mathbf{g}_0 \quad \text{in } M; \\ \mathbf{n} \cdot \boldsymbol{\sigma} &= \lambda^- \mathbf{f}_0 \quad \text{on } A_f; \\ f(\boldsymbol{\sigma}) &\leq 0 \quad \text{in } M. \end{aligned} \tag{2.15}$$

2.3 Mathematical optimization

Mathematical optimization is concerned with obtaining the minimum or maximum value of an objective function f_0 subject to equality and/or inequality constraints. A mathematical optimization problem typically takes the following form:

$$\min f_0(\mathbf{x})$$

subject to

$$f_i(\mathbf{x}) = 0 \quad \forall i \in \{1, \dots, m\}; \tag{2.16}$$

where $\mathbf{x}^T = \{x_1, \dots, x_n\}$ is a vector of optimization variables; $f_i \forall i \in \{1, \dots, m\}$ are constraint functions; and n and m are the total number of optimization variables and constraints, respectively.

The upper and lower bound theorems of limit analysis can readily be understood as mathematical optimization problems with an infinite number of constraints and variables (see equations (2.9) and (2.15)). Various discretization techniques, limiting the number of (pointwise) constraints, have been employed allowing upper and lower bounds to be obtained using optimization algorithms. The accuracy of these bounds will depend greatly on the discretization used. Limit analysis, typically, minimizes or maximises a linear objective function subject to linear equality constraints enforcing kinematic or static admissibility and convex equality and/or inequality constraints enforcing plastic admissibility. Limit analysis is, therefore, primarily concerned with convex optimization. The optimization algorithm used is a key factor in determining the computational efficiency of a particular numerical technique.

In limit analysis, the algorithm used is largely determined by the yield function. Yield functions including singularities, such as the three-dimensional Tresca and Mohr-Coulomb yield function (shown in Figure 2.3), are particularly problematic. The ability of different optimization classes to handle the Mohr-Coulomb yield condition are summarised in Table 2.1. Nonlinear programming (NLP), for example, cannot deal with the Mohr-Coulomb yield condition directly; although a smoothed approximation may be used. In recent years, conic programming has attracted particular attention due both to its efficiency and ability to handle the two- and three-dimensional Mohr-Coulomb yield conditions directly (Makrodimopoulos and Martin, 2006; Krabbenhøft et al., 2007; Krabbenhøft et al., 2008; Martin and Makrodimopoulos, 2008).

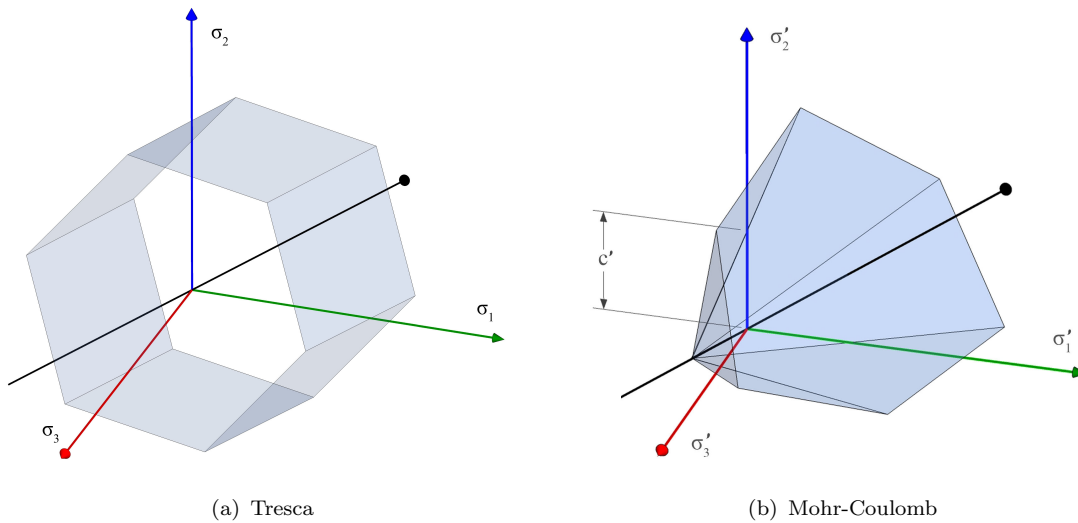


FIGURE 2.3: Three-dimensional yield surface (from Clarke (2009))

Conic programming is concerned with optimization problems of the form (Makrodimopoulos, 2010):

$$\begin{aligned}
 & \min \mathbf{c}^T \mathbf{x} \\
 & \text{subject to} \\
 & \mathbf{Ax} = \mathbf{b}; \\
 & \mathbf{x} \in \mathcal{K}_i \quad \forall i = 1, \dots, N;
 \end{aligned} \tag{2.17}$$

where \mathbf{c} and \mathbf{b} are vectors of problem coefficients; \mathbf{A} is a constraint matrix; \mathcal{K}_i is a cone; and N is the number of conic constraints. As with all convex optimization problems, the conic program in equation (2.17) can be stated in an equivalent, dual form:

$$\begin{aligned} & \max \mathbf{b}^T \mathbf{y} \\ & \text{subject to} \\ & \mathbf{A}^T \mathbf{y} + \mathbf{s} = \mathbf{c}; \\ & \mathbf{s} \in \mathcal{K}_i^* \quad \forall i \in \{1, \dots, N\}; \end{aligned} \tag{2.18}$$

where \mathbf{y} is a vector of dual optimization variables; \mathbf{s} is a vector of dual cone variables; and \mathcal{K}_i^* is the dual of cone \mathcal{K}_i .

The most relevant cones to limit analysis are summarized below.

- The non-negative orthant:

$$\mathcal{K} = \mathbb{R}_+^n = \{x | x \geq 0\}. \tag{2.19}$$

- The Lorentz cone:

$$\mathcal{K} = \mathcal{K}_q^n = \{x \in \mathbb{R}^n | x \geq \sqrt{x_2^2 + \dots + x_n^2}\}. \tag{2.20}$$

- The rotated quadratic cone:

$$\mathcal{K} = \mathcal{K}_r^n = \{x \in \mathbb{R}^n | 2x_1x_2 \geq x_2^2 + \dots + x_n^2, x_1, x_2 \geq 0\}. \tag{2.21}$$

- The semi-definite cone:

$$\mathcal{K} = S_+^n = \{\mathbf{X} \in \mathbb{R}^{n \times n} | \mathbf{X} \succeq 0, \mathbf{X} = \mathbf{X}^T\}; \tag{2.22}$$

where \succeq denotes that matrix \mathbf{X} is positive semi-definite (*i.e.* $\mathbf{z}^T \mathbf{X} \mathbf{z} \geq 0$, where \mathbf{z} is a vector of arbitrary real numbers).

TABLE 2.1: Optimization classes enforcing the Mohr-Coulomb yield function

optimization class	2D Discontinuity	2D Continuum	3D Discontinuity	3D Continuum
linear programming (LP)	●	○	○	
second order cone programming (SOCP)	●	●	●	
semidefinite programming (SDP)	●	●	●	●
nonlinear programming (NLP)	○	○	○	○

● yield condition can be exactly enforced; ○ yield condition can be enforced approximately.

\mathbb{R}_+^n , \mathcal{K}_q , \mathcal{K}_r and S_+^n are all self-dual cones; that is $\mathcal{K}_i = \mathcal{K}_i^*$.

Conic programming can be grouped into several classes: linear programming (LP) allowing consideration of $\mathcal{K} = R_+^n$; second order cone programming (SOCP) allowing consideration of $\mathcal{K} = \mathcal{K}_q$ and $\mathcal{K} = \mathcal{K}_r$ in addition to $\mathcal{K} = R_+^n$; and semi-definite programming (SDP) allowing consideration of $\mathcal{K} = S_+$ in addition to $\mathcal{K} = R_+^n$, $\mathcal{K} = \mathcal{K}_q$, $\mathcal{K} = \mathcal{K}_r$. Of these, SDP is the most general allowing consideration of SOCP and LP problems, and LP is the least general.

The efficiency of algorithms used to solve different classes of conic programs varies. LP technology is well established and LP algorithms are, generally, the most robust and efficient, followed by SOCP algorithms. LP problems can be solved using a choice of simplex or interior point optimizers. SOCP and SDP problems, on the other hand, can only be solved using interior point optimizers.

In Section 2.5.4, optimization algorithms are discussed further in the context of finite element limit analysis (FELA).

2.4 Direct methods

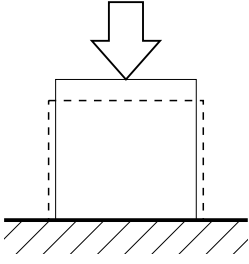
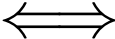
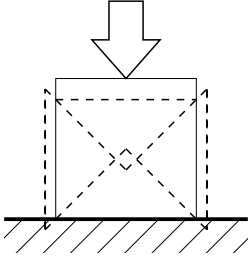
2.4.1 Introduction

Direct methods, such as limit analysis, estimate the collapse load directly. In limit analysis, upper bound methods, typically formulated in terms of strain and displacement, will always overestimate the collapse load. Lower bound methods, on the other hand, always underestimate the collapse load and are typically formulated in terms of stress. Alternatively, mixed formulations, typically, involve both stress and strains fields. The status of solutions obtained using mixed formulations are not known *a priori* and may be upper or lower bounds on the ‘exact’ collapse load. Differing definitions of term mixed exist. Henceforth, any method will be referred to as mixed, where the limit analysis status of the solution is not known *a priori*.

At collapse, discontinuities or jumps in the stress and velocity fields can develop. For certain classes of problem, the ability of a direct method to handle such discontinuities can greatly influence the accuracy of solutions obtained. Continuous methods allow smooth variations of stress or velocity, but discontinuities are not permitted. In continuous methods, discontinuities must be modelled by rapid changes in velocity or stress across narrow bands. Discontinuous methods allow discontinuities; however, smooth variations are not permitted. In discontinuous methods, smooth variations must be modelled using high concentrations of discontinuities. Hybrid methods are more versatile and allow both discontinuous and smooth variations. In Table 2.2, continuous, discontinuous and hybrid methods are grouped according to the limit analysis status of their solutions. Both discontinuous and hybrid methods allow direct consideration of discontinuities.

In the following sections, the relative strengths and weaknesses of commonly used direct methods will be reviewed. In particular, their ability to handle discontinuities will be emphasized. Their ability to solve three-dimensional problems will also be noted in passing.

TABLE 2.2: Continuous, discontinuous and hybrid methods by limit analysis status

	continuous	hybrid	discontinuous
limit analysis status			
upper bound	FELA MC LM	FELA MC	hand calc. RFEM DLO
mixed	finite difference meshless FELA		LEM
lower bound	FELA MC [†]	FELA MC [†]	hand calc.

[†] incomplete lower bound, stress field must be extended outside the mechanism

2.4.2 Trial and error

Simple hand based calculations have been widely used in geotechnical engineering to estimate the collapse load. In particular, the limit equilibrium method (LEM) has been widely used in slope stability analysis. In limit equilibrium, a simple discontinuous failure mechanism is investigated and a stress distribution assumed on the discontinuities. A collapse load is then calculated from equilibrium. The failure mechanism need not be plastically admissible and the resulting collapse load is not *a priori* an upper bound. The process is manually repeated for different mechanisms to obtain a minimum collapse load.

Similarly, the upper bound theorem allows the collapse load to be estimated by assuming simple discontinuous failure mechanisms. Unlike LEM, the assumed mechanism must be plastically admissible, allowing strict upper bounds to be

determined. Chen (1975) reviews a number of simple upper bound solutions to geotechnical problems. Trial and error methods involving more complex mechanisms including deforming regions have been used more recently by Michalowski (2001), Puzrin and Randolph (2003) and Michalowski and Drescher (2009) to obtain upper solutions to three-dimensional problems. Simple trial and error applications of the lower bound theorem are more involved and consequently less widely used.

2.4.3 Method of characteristics

The method of characteristics (MC) has been used to successfully obtain highly accurate, in some cases ‘exact’, solutions. Sokolovski (1965) provides solutions to a number of geotechnical problems. The method of characteristics allows both smooth or discontinuous variations of the stress and strain fields. However, it is necessary to know the general form of the solution. Consequently, only simple boundary and geometries are generally considered, considerably limiting its applicability.

Recently, Martin (2011) has used the MC to refine highly accurate finite element limit analysis (FELA) solutions, demonstrating a new potentially fruitful application. In MC, information on the stress field is limited to the plastically deforming regions. Therefore, it is necessary to find a compatible admissible stress field in any rigid regions to obtain a complete lower bound. Furthermore, the MC is not applicable to three-dimensional problems, an important limitation.

2.4.4 Numerical methods

2.4.4.1 Introduction

Numerical methods discretize the problem domain, allowing approximations to the limit load to be obtained. Optimization is, typically, employed to determine the best approximation possible for a particular discretization. Numerical methods

have proved popular among researchers and different numerical techniques have been developed variously considering the problem domain as continuum, discontinuum or a hybrid of the two. An overview of the methods applicable to continua, discontinua and hybrid continua/discontinua will be presented in the following sections. Of these methods, finite element limit analysis (FELA) has attracted the most attention among researchers (see Section 2.5).

2.4.4.2 Continuous methods

The finite difference method was among the first direct numerical methods developed (Koopman and Lance, 1965). In the finite difference method, nodes are distributed on a rectangular grid. While well-suited to rectangular problem domains and simple boundary conditions, consideration of arbitrary boundary conditions and geometry is complicated by the rectangular grid (Chakrabarty, 2006). In contrast, meshless methods use nodes scattered within the domain and on domain boundaries (Belytschko et al., 1994; Le, 2009; Le et al., 2012). While arbitrary geometries are possible, strict enforcement of the boundary conditions is not. The status of both finite difference and meshless solutions are not known *a priori*.

A major challenge to any continuous limit analysis method is avoiding volumetric locking. FELA using constant strain elements can result in volumetric locking unless elements are specially arranged (see Nagtegaal et al. (1974)), a significant limitation. Therefore, researchers have resorted to higher order elements or hybrid FELA to obtain rigorous upper bounds (Makrodimopoulos and Martin, 2007; Sloan, 1989). Vicente da Silva and Antão (2007) used specially arranged constant strain elements to consider three-dimensional problems. Martin and Makrodimopoulos (2008), Krabbenhøft et al. (2008) and Antão et al. (2012) used continuous higher order elements thus avoiding the need for specially arranged elements to obtain three-dimensional upper bounds.

Alternatively, mixed FELA may be used to obtain approximations to the limit load, avoiding volumetric locking. For example, the rigid-plastic finite element method relaxes the von Mises yield criteria by enforcing incompressibility only in

an average manner (Lee and Kobayashi, 1973; Tamura et al., 1984) and Capsoni and Corradi (1997) relax compatibility to overcome volumetric locking. Park and Kobayashi (1984) have developed a variant of the rigid-plastic finite element method for the incompressible von Mises yield criteria; which solves three-dimensional problems using a finite but large bulk modulus. All these methods require special measures to deal with rigid regions; either by eliminating these or locally adopting a linear elastic model. Other notable contributions are the mixed finite element formulations of Casciaro and Cascini (1982) and Christiansen (1981).

Another continuous method, the linear matching (LM) method, developed by Ponter and Carter (1997) and Ponter et al. (2000), uses linear elastic methods to iteratively obtain upper bound solutions. In each iteration, the elastic strain is matched to a stress state on the yield surface by spatially varying elastic moduli. These spatially varying moduli are used to produce a new linear elastic solution. The procedure is then repeated. Corners in the three-dimensional Tresca and Mohr-Coulomb yield criteria make selecting appropriate elastic material properties particularly problematic. The author is unaware of any applications of LM using these yield criteria.

2.4.4.3 Hybrid

Many continuous methods perform poorly when considering problems containing stress and strain singularities. Continuous FELA using linear stress or constant strain elements are such methods. By incorporating discontinuities between elements, hybrid FELA seeks to overcome this limitation. Hybrid FELA has the added benefit of improved performance with respect to volumetric locking. Following the pioneering work of Lysmer (1970) and Bottero et al. (1980), hybrid FELA has, typically, employed linear stress or constant strain elements (Sloan, 1988; Makrodimopoulos and Martin, 2006; Muñoz et al., 2009). However, the quality of solutions obtained from such discretizations is highly dependent on the location of inter-element discontinuities, particularly in the vicinity of stress and strain singularities. Therefore, effective mesh design requires the form of the ‘exact’ solution to be known *a priori*. Adaptive schemes seek to overcome these

shortcomings by automatically refining the mesh (see Section 2.5.3). Hybrid formulations using higher order elements, unsurprisingly, do not suffer from these limitations (Makrodimopoulos and Martin, 2008; Yu et al., 1994).

Recently, hybrid FELA methods for three-dimensional analysis have been developed using constant strain or linear stress elements (Lyamin and Sloan, 2002b,a; Vicente da Silva and Antão, 2008; Krabbenhøft et al., 2008); however, these suffer from the same shortcoming as their two-dimensional equivalents.

2.4.4.4 Discontinuous

The discontinuous, upper bound rigid finite element method (RFEM) has been developed recognizing the importance of discontinuities (van Rij and Hodge, 1978; Alwis, 2000). Deformations are only permitted along discontinuities at the boundaries of predefined solid elements. Unlike hybrid FELA, the elements themselves are not free to deform. Clearly, the range of mechanisms that can be identified is severely limited and accurate solutions are only possible for meshes closely that capture the ‘exact’ collapse mechanism. Therefore, an accurate solution requires the form of the ‘exact’ solution to be known *a priori*.

By considering yield only on the discontinuities, RFEM can adopt simpler, more efficient optimization algorithms relative to FELA. For example, the Mohr-Coulomb yield criteria can be enforced exactly on a plane strain discontinuity using LP, without need for any approximation; however, SOCP is needed to enforce the Mohr-Coulomb yield criteria exactly over a plane strain continuum (see Table 2.3). (Note linearization of the plane strain continuum yield function is possible but an accurate solution, typically, requires a large number of additional constraints). Similarly, the Mohr-Coulomb yield criteria can be enforced exactly on a three-dimensional discontinuity using SOCP; however, SDP is required over a three-dimensional continuum. Chen et al. (2003), for example, has used RFEM to obtain upper bounds to three-dimensional slope stability problems using sequential quadratic programming.

Unlike RFEM, discontinuity layout optimization (DLO) is posed entirely in terms of velocity discontinuities (Smith and Gilbert, 2007). DLO can be viewed as an automation of the simple hand based calculations discussed in Section 2.4.2; where optimization is used to determine the critical layout of the discontinuities (and associated upper bound) from among a large set of potential discontinuities. DLO retains the simpler, more efficient algorithms (relative to continuous or hybrid numerical methods) associated with RFEM; however unlike RFEM, a large number of potential mechanisms can be identified, allowing the procedure to be largely mesh independent. This is because in DLO discontinuities are no longer restricted to the boundaries of predefined solid elements but can connect any node to any other node. DLO and RFEM are compared in Figure 2.4 using a simple example. In Figures 2.4(c) and 2.4(d), a rectangular nodal grid is connected to form RFEM and DLO meshes, respectively; where the RFEM mesh consists of rigid triangular elements, separated by linear discontinuities, and the DLO mesh consists purely of linear discontinuities. Both the RFEM and DLO meshes allow the mechanism in Figure 2.4(e). However, mechanism in Figure 2.4(f) can only be identified using the DLO mesh.

Smith and Gilbert (2007) have validated DLO against a number of established plane strain benchmarks, obtaining accurate results at moderate computational expense. The plane strain DLO procedure has successfully been commercialized as software package LimitState:GEO (LimitState, 2012). The objective of the current research is to develop a three-dimensional implementation of this promising new procedure. A more detailed overview of the DLO will follow in Section 2.6.

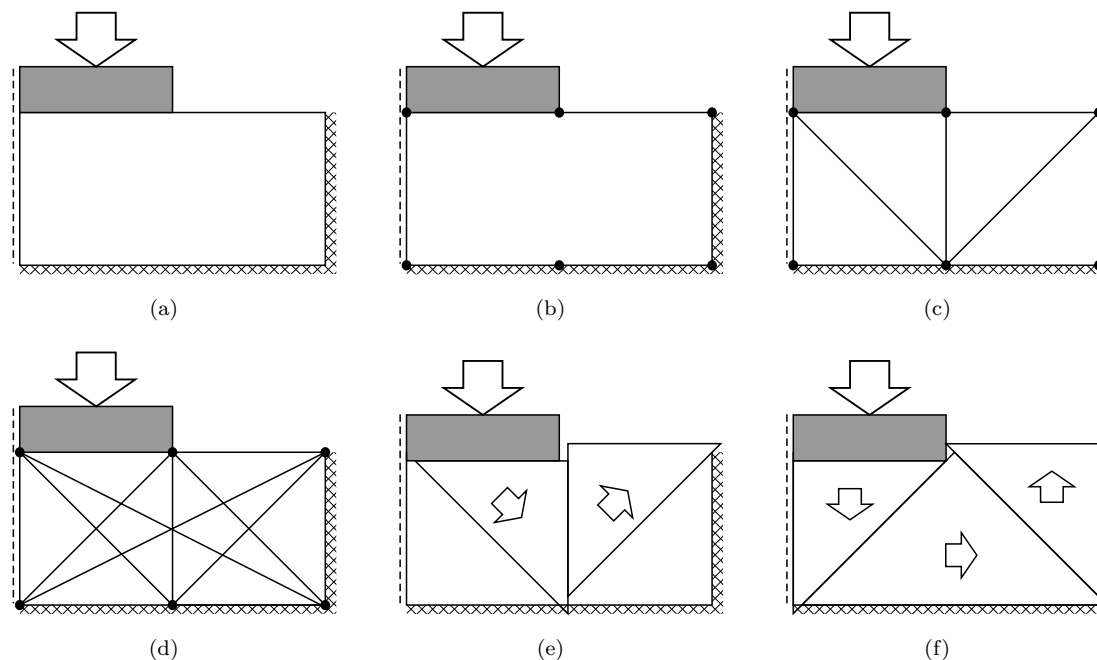


FIGURE 2.4: Comparison of RFEM and DLO using a simple example: (a) Starting problem – Prandtl problem (taking advantage of symmetry) (b) discretized using a rectangular grid of nodes. (c) shows a RFEM mesh formed from solid elements, separated by linear discontinuities, with the nodes in (b) as vertices. (d) shows a DLO mesh of linear discontinuities connecting every node in (b) to every other node in (b). (e) shows a mechanism identifiable by both the RFEM mesh in (c) and the DLO mesh in (d); however, the mechanism shown in (f) can only be identified by the DLO mesh in (d).

2.5 Finite element limit analysis

2.5.1 Introduction

In recent years, limit analysis research, particularly three-dimensional applications of, has focused on finite element limit analysis (FELA), both continuous (Vicente da Silva and Antão, 2007; Martin and Makrodimopoulos, 2008; Krabbenhøft et al., 2008) and hybrid (Lyamin and Sloan, 2002a,b; Krabbenhøft et al., 2008). In the following sections, FELA will be examined in more depth, focusing on three aspects: (i) volumetric locking, (ii) enhancements to improve solution accuracy or computational efficiency, (iii) optimization algorithms.

2.5.2 Volumetric locking

The problem of volumetric locking was first identified by Nagtegaal et al. (1974). Volumetric locking phenomena is normally associated with incompressible materials; however, similar difficulties are encountered when considering the Mohr-Coulomb material model. Volumetric locking occurs in upper bound analysis when the constraints enforcing the flow rule exceed the available degrees of freedom. Consequently, a feasible mechanism cannot be identified. Nagtegaal et al. (1974) demonstrated that many conventional elements result in locking, particularly lower order elements. A number of strategies have been developed to overcome locking.

- (i) Lower order elements arranged in specific layouts. These arrangement reduce the number of constraints necessary to enforce the flow rule (Nagtegaal et al., 1974; Vicente da Silva and Antão, 2007). However, this places an important restriction on the class of mechanism that can be identified.
- (ii) Hybrid FELA is, perhaps, the most commonly used strategy (Sloan, 1989; Lyamin and Sloan, 2002b; Krabbenhøft et al., 2008). The introduction of discontinuities results in additional degrees of freedom. However, some attention to the layout of elements is still needed to avoid locking.
- (iii) Higher order elements are the most robust and effective approach for avoiding locking (Yu et al., 1994; Makrodimopoulos and Martin, 2007). However, higher order elements result in increased computational cost.
- (iv) Mixed finite elements have also been used to avoid locking (Casciaro and Cascini, 1982; Capsoni and Corradi, 1997). However, the status of solutions is no longer known *a priori*.

2.5.3 Enhancements

In the following section, two enhancements to FELA will be reviewed: adaptive remeshing and decompositional procedures. These procedures can be used to

improve the accuracy of solutions or, alternatively, reduce computational effort and/or runtime.

Adaptive remeshing aims to improve accuracy of the solution in the most cost effective manner. In adaptive remeshing, an initial mesh is successively improved, guided by specific criteria. An improved mesh may be achieved by (i) locally substituting higher order elements for lower order elements, (ii) locally rearranging the geometry of existing elements or (iii) locally splitting existing elements into smaller elements. The last is the most commonly adopted strategy in FELA and differing criteria have been used to select candidates for refinement. For example, Borges et al. (2001) and Lyamin et al. (2005) have used local directional error estimates to guide the adaptive procedure. Muñoz et al. (2009) have used the contribution of individual elements and discontinuities to the gap between upper and lower bound solutions to select candidates for refinement. Christiansen and Pedersen (2001) and Martin (2011) present adaptive procedures guided by strain rate; however, these adaptive procedures may not converge toward the global optimum. Martin (2011) has used this procedure to obtain highly accurate bounds for some traditionally difficult benchmark problems. Alternatively, Christiansen and Pedersen (2001) also use proximity to yield to guide the adaptive procedure; however, a large proportion of elements are, typically, close to yield, resulting in a large number of candidates for refinement.

In recent years, improved parallel processing technology has stimulated interest in decompositional procedures. Decompositional procedures seek to split a problem into smaller subproblems. Ideally, these sub-problems could be solved in parallel, exploiting parallel processing. Pastor et al. (2009) and Kammoun et al. (2010) have developed a decompositional procedure based on overlapping regions and allowing highly accurate upper and lower bounds to be obtained. Figure 2.5 illustrates this procedure using a simple example.

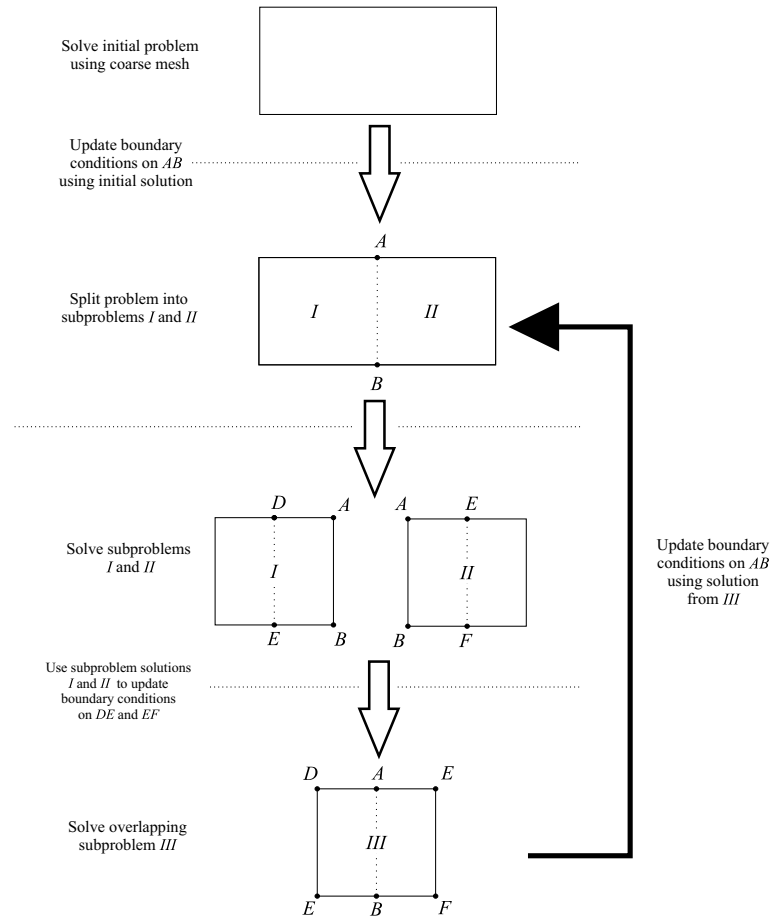


FIGURE 2.5: Simple example illustrating the decompositional procedure of Pastor et al. (2009).

2.5.4 Optimization

The computational efficiency of a FELA formulation is normally closely linked to that of its optimization algorithm. Suitable optimization techniques for the Mohr-Coulomb yield criterion are summarised in Table 2.3. Linearization of the three-dimensional Mohr-Coulomb yield function for a continuum is not straightforward; however, the two-dimensional Mohr-Coulomb yield condition for a continuum can be approximated using predefined linear constraints (Bottero et al., 1980; Sloan, 1988, 1989). This linearization allows efficient LP algorithms to be used. A large number of constraints is, typically, required for accurate solution, resulting in increased computational expense. Observing that very few of these constraints

are active, Lysmer (1970) used a small number of constraints to iteratively approximate the yield function. These constraints are adjusted using the solution from the previous iteration; however, such an approach may result in cycling or instability. Alternatively, the cutting plane method may be used (Kelley, 1960). In the cutting plane method, constraints are added based on previous iterations; however, existing constraints remain unchanged thus avoiding the cycling and instability, observed in Lysmer's approach. Krabbenhøft and Damkilde (2000) have successfully applied the cutting plane method to plates using the Nielsen yield criterion.

Zouain and Herskovits (1993), Lyamin and Sloan (2002a,b) and Krabbenhøft and Damkilde (2003) have used nonlinear programming (NLP) to consider limit analysis problems. NLP allows nonlinear constraints to be included directly in the optimization, provided these constraints are differentiable everywhere. The Mohr-Coulomb yield function, however, cannot be handled directly as this is not differentiable at its apex. Instead, Lyamin and Sloan (2002a,b) have used NLP with smoothed approximations to the two- and three-dimensional Mohr-Coulomb yield functions.

Alternatively, conic programming may be used to directly enforce the Mohr-Coulomb yield condition (see Section 2.3 and Table 2.1). For example, Makrodimopoulos and Martin (2006, 2007, 2008) and Krabbenhøft et al. (2007) have used efficient SOCP to consider the two-dimensional Mohr-Coulomb yield condition. Martin and Makrodimopoulos (2008) and Krabbenhøft et al. (2008) have used SDP to consider the three-dimensional Mohr-Coulomb yield condition.

2.6 Discontinuity layout optimization

2.6.1 Introduction

Discontinuity layout optimization (DLO), developed by Smith and Gilbert (2007) for plane strain, allows translational mechanisms to be identified. (DLO has been

extended to including rotations (Gilbert et al., 2010a; Smith, 2012); however, these extensions are not covered in the current overview.) DLO determines the critical layout of velocity discontinuities, with the least upper bound solution, from among a large set of potential discontinuities. From duality principles, two equivalent formulations of DLO are possible, known as the kinematic and equilibrium formulations, respectively.

2.6.2 Kinematic formulation

2.6.2.1 Introduction

The DLO procedure for plane strain problems is outlined in Figure 2.6. Firstly, the initial problem is discretized using nodes distributed across the body under consideration. Potential discontinuity lines (*i.e.* ‘slip lines’), along which jumps in rate of displacements \mathbf{d} can occur, are created by linking each node to every other node and linear programming is used to identify the subset of discontinuities active in the critical failure mechanism. (Note that henceforth, ‘energy dissipation’ and ‘displacement’ will be used as shorthand for ‘rate of energy dissipation’ and ‘rate of displacement’, respectively.) Provided a sufficiently large number of nodes are employed, this allows a very wide range of potential mechanisms to be considered.

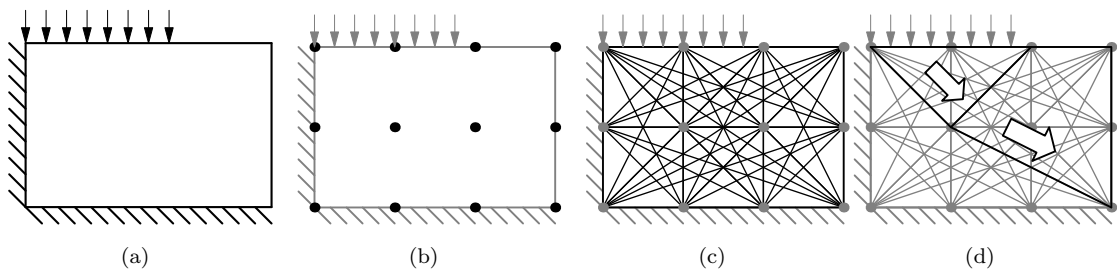


FIGURE 2.6: Stages in DLO procedure: (a) starting problem (surcharge applied to block of soil close to a vertical cut); (b) discretization of soil using nodes; (c) interconnection of nodes with potential discontinuities; (d) identification of critical subset of potential discontinuities using optimisation (giving the layout of slip-lines in the critical failure mechanism) (after Gilbert et al. (2010b))

In mathematical terms, the corresponding kinematic formulation is given in equations (2.23-2.27), posed entirely in terms of potential discontinuities (after Smith and Gilbert (2007)).

$$\min \lambda \mathbf{f}_L^T \mathbf{d} = -\mathbf{f}_D^T \mathbf{d} + \mathbf{g}^T \mathbf{p} \quad (2.23)$$

subject to

$$\mathbf{B} \mathbf{d} = \mathbf{0}, \quad (2.24)$$

$$\mathbf{N} \mathbf{p} - \mathbf{d} = \mathbf{0}, \quad (2.25)$$

$$\mathbf{f}_L^T \mathbf{d} = \mathbf{1}, \quad (2.26)$$

$$\mathbf{p} \geq \mathbf{0}; \quad (2.27)$$

where λ is a multiplier on the live load; \mathbf{f}_D and \mathbf{f}_L are vectors containing live and dead loads, respectively; \mathbf{d} is a vector containing relative jumps in displacement at the discontinuities; and \mathbf{g} is a vector of dissipation coefficients. \mathbf{B} is a global compatibility matrix; \mathbf{N} is a global matrix enforcing the flow rule; and \mathbf{p} is a vector of plastic multipliers.

2.6.2.2 Compatibility

The kinematic formulation identifies the critical mechanism from among a wide range of potential mechanisms. These mechanisms are constructed from rigid-blocks separated by discontinuities. At each discontinuity i , a shear jump s_i in displacement and normal jump n_i in displacement are permitted. In equation (2.24), compatibility of the mechanism is enforced by constraints at each node.

This is illustrated with the help of Figure 2.7, showing all discontinuities meeting at a single node. Examining Figure 2.7, it is clear that the following summations

$$\sum_{i=1}^5 \alpha_i s_i - \beta_i n_i = 0, \quad (2.28)$$

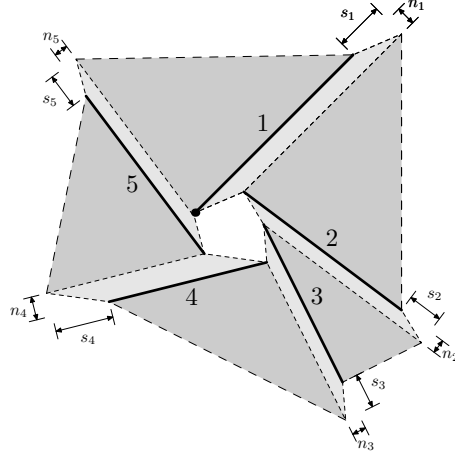


FIGURE 2.7: Compatibility at a node (from Smith and Gilbert (2007))

$$\sum_{i=1}^5 \beta_i s_i + \alpha_i n_i = 0 \quad (2.29)$$

must hold at the node for compatibility; where $\alpha_i = \cos \theta_i$ and $\beta_i = \sin \theta_i$; and θ_i is the anticlockwise angle between discontinuity i and the x axis. Repeating summations (2.28) and (2.29) at each node, equation (2.24) is constructed; where \mathbf{B} is a $2n \times 2m$ global compatibility matrix, containing direction cosines; $\mathbf{d}^T = \{s_1, n_1, s_2, \dots, n_m\}$; and n, m are the total number of nodes and discontinuities, respectively.

In DLO, intersections or ‘crossovers’ between potential discontinuities arise naturally at locations other than the original nodes. Compatibility, while not explicitly enforced at the ‘crossovers’, is implicitly maintained. This is illustrated with the help of Figure 2.8, showing the ‘crossover’ or intersection between two discontinuities (1 & 2). Discontinuities 1 and 2 are split into halves $1', 1''$ and $2', 2''$, respectively, either side of the ‘crossover’. Obviously, $\theta_{1''} = \theta_{1'} + 180^\circ$, $\theta_{2''} = \theta_{2'} + 180^\circ$. The displacement jumps s_1, n_1, s_2 and n_2 remain unchanged. Applying a summation procedure similar to equations (2.28) and (2.29) at the ‘crossover’ point, the displacements jumps on $1'$ and $1''$ cancel out as do the displacements jumps on $2'$ and $2''$. It can, therefore, be concluded that compatibility is always maintained at a ‘crossover’.

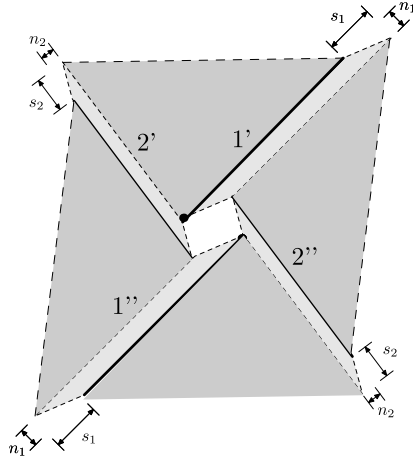


FIGURE 2.8: Compatibility at a 'crossover' point

2.6.2.3 Flow rule and energy dissipation

Energy dissipation from all the discontinuities is included in the objective function, enforcing work balance, via global vectors $\mathbf{g} = \{\mathbf{g}_1, \mathbf{g}_2, \dots, \mathbf{g}_m\}$ and \mathbf{p} . The energy dissipation on a discontinuity i is simply $c_i l_i |s_i|$, where c_i is the shear strength on discontinuity i and l_i is the length of discontinuity i . $c_i l_i |s_i| = \mathbf{g}_i^T \mathbf{p}_i = \{c_i l_i, c_i l_i\} \{p_i^1, p_i^2\}^T$, where the optimizer minimizes the energy dissipated so that either $p_i^1 = |s_i|, p_i^2 = 0$ or $p_i^1 = 0, p_i^2 = |s_i|$.

For the solution to be an upper bound, the associated flow rule must be satisfied. In DLO, the flow rule is enforced by equations (2.25) and (2.27). Locally on a discontinuity i , equations (2.25) and (2.27) enforce the associated Mohr-Coulomb flow rule

$$\mathbf{N}_i \mathbf{p}_i - \mathbf{d}_i = \begin{bmatrix} 1 & -1 \\ \tan \phi_i & \tan \phi_i \end{bmatrix} \begin{bmatrix} p_i^1 \\ p_i^2 \end{bmatrix} - \begin{bmatrix} s_i \\ n_i \end{bmatrix} = \mathbf{0}; \quad (2.30)$$

where ϕ_i is the angle of friction on discontinuity i ; $p_i^1, p_i^2 \geq 0$ are plastic multipliers; \mathbf{N}_i is a local plastic flow matrix; and \mathbf{p}_i is a vector containing the plastic multipliers. \mathbf{N}_i and \mathbf{p}_i on discontinuities $i (i = 1, 2, \dots, m)$ are assembled to form the global matrix \mathbf{N} and the global vector $\mathbf{p}^T = \{p_1^1, p_1^2, p_2^1, \dots, p_m^2\}$, respectively. The flow rule is always strictly enforced as either $p_i^1 = |s_i|, p_i^2 = 0$ or $p_i^1 = 0, p_i^2 = |s_i|$ in the critical solution.

Boundary conditions can now be conveniently applied by including variables (and corresponding columns) and constraints, as demonstrated by Table 2.3.

TABLE 2.3: Applying plain strain flow rule conditions in DLO

	Apply Eq. (2.30)	Include n_i	Include s_i	Include p_i^1, p_i^2
Interior discontinuity				
$\phi_i > 0, c_i \geq 0$	•	•	•	•
$c_i, \phi_i = 0$			•	
$c_i > 0, \phi_i = 0^*$	•		•	•
Boundary discontinuity				
free		•	•	
symmetry			•	
rigid	•	•	•	•

Key: * only include the top half of equation 2.30

2.6.2.4 Specification of loads

Dead loads are specified via vector \mathbf{f}_D in the objective function or work balance, equation (2.23); where $\mathbf{f}_D^T = \{f_{D1}^s, f_{D1}^n, f_{D2}^s, f_{D2}^n, \dots, f_{Dm}^n\}$; and f_{Di}^s, f_{Di}^n are the shear and normal dead loads, respectively, on discontinuity i ($i = 1, \dots, m$). Live loads are applied via vector \mathbf{f}_L in equation (2.26); where $\mathbf{f}_L^T = \{f_{L1}^s, f_{L1}^n, f_{L2}^s, f_{L2}^n, \dots, f_{Lm}^n\}$; and f_{Li}^s, f_{Li}^n are the shear and normal live loads, respectively, on discontinuity i .

At external boundaries, displacement jumps must be identical to absolute displacement. For a discontinuity i on an external boundary, $\mathbf{f}_{Di}^T = \{f_{Di}^s, f_{Di}^n\}$ and $\mathbf{f}_{Li} = \{f_{Li}^s, f_{Li}^n\}$ simply contain the dead and live loads, respectively, applied directly to discontinuity i . Within a body, displacement jumps no longer equal absolute displacement. Therefore, loads applied within a body must be applied via a summation. For self-weight, this is illustrated with the help of Figure 2.9.

Figure 2.9(a) shows a vertical column slice through a simple DLO mesh. The vertical slice is traversed by four discontinuities 1 – 4. Examining this vertical slice more closely in Figure 2.9(b), it becomes clear that discontinuities 1 – 4 divide the slice into three solids (A , B and C) with self-weights w_A , w_B and w_C , respectively. Figure 2.9(c) shows the same slice but this time through a deformed mechanism. Solids A , B and C are now associated with absolute vertical displacements V_A , V_B and V_C , respectively. As the lower boundary is rigid, $V_A = -\beta_1 s_1 - \alpha_1 n_1$, $V_B = V_A - \beta_2 s_2 - \alpha_2 n_2$ and $V_C = V_B - \beta_3 s_3 - \alpha_3 n_3$. Therefore, the work Ω done by the column self-weight is

$$\begin{aligned}\Omega &= V_A w_A + V_B w_B + V_C w_C \\ &= (-\beta_1 s_1 - \alpha_1 n_1) w_A + (-\beta_1 s_1 - \alpha_1 n_1 - \beta_2 s_2 - \alpha_2 n_2) w_B \\ &\quad + (-\beta_1 s_1 - \alpha_1 n_1 - \beta_2 s_2 - \alpha_2 n_2 - \beta_3 s_3 - \alpha_3 n_3) w_C.\end{aligned}\quad (2.31)$$

Rearranging equation (2.31)

$$\begin{aligned}\Omega &= (-\beta_1 s_1 - \alpha_1 n_1)(w_A + w_B + w_C) \\ &\quad + (-\beta_2 s_2 - \alpha_2 n_2)(w_B + w_C) + (-\beta_3 s_3 - \alpha_3 n_3)(w_C) \\ &= W_1(-\beta_1 s_1 - \alpha_1 n_1) + W_2(-\beta_2 s_2 - \alpha_2 n_2) + W_3(-\beta_3 s_3 - \alpha_3 n_3); (2.32)\end{aligned}$$

where $W_1 = w_A + w_B + w_C$, $W_2 = w_B + w_C$ and $W_3 = w_C$ are the total weight of the material lying vertically above discontinuities 1, 2 and 3, respectively. Therefore, the contribution made by discontinuity i to the work balance is simply:

$$\mathbf{f}_{D_i}^T \mathbf{d}_i = \begin{bmatrix} -W_i \beta_i & -W_i \alpha_i \end{bmatrix} \begin{bmatrix} s_i \\ n_i \end{bmatrix} \quad (2.33)$$

where W_i is the total weight of the material lying vertically above discontinuity i . (Note that loads applied to external boundaries are not included in W_i .) The summation need not be vertical, but could be carried out in an arbitrary direction Smith and Cubrinovski (2011a).

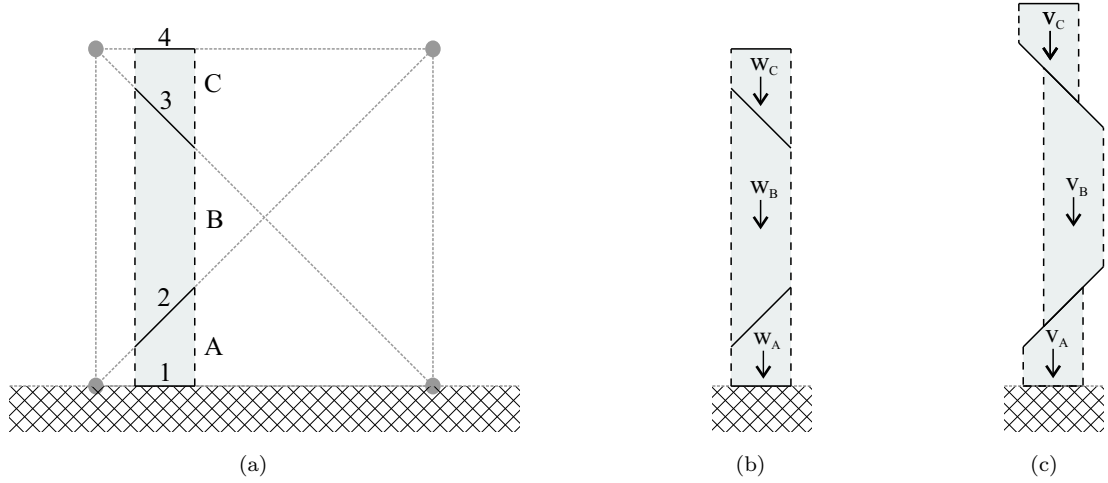


FIGURE 2.9: Summation of dead loads. (a) Vertical strip through a DLO mesh, split into three solids A , B , and C by discontinuities 1-4. (b) Solids A , B , and C are associated with self-weights w_A , w_B and w_C . (c) Deformed vertical strip with absolute vertical displacements V_A , V_B , and V_C for the solids.

2.6.3 Equilibrium formulation

Smith and Gilbert (2007) used duality principles to derive the following dual, equilibrium formulation:

$$\max \lambda \quad (2.34)$$

subject to

$$\mathbf{B}^T \mathbf{t} + \lambda \mathbf{f}_L - \mathbf{q} = -\mathbf{f}_D, \quad (2.35)$$

$$\mathbf{N}^T \mathbf{q} \leq \mathbf{g}; \quad (2.36)$$

where $\mathbf{t} = \{t_1^x, t_1^y, t_2^x, t_2^y, \dots, t_n^y\}$; t_j^x and t_j^y were interpreted as equivalent nodal forces in the x and y directions, respectively, on nodes j ($j = 1, \dots, n$); $\mathbf{q}^T = \{S_1, N_1, S_2, N_2, \dots, N_m\}$, where S_i and N_i are the internal shear and normal forces acting on discontinuity i .

On a discontinuity i , equations (2.35) and (2.36) enforce an equilibrium condition

$$\begin{bmatrix} \alpha_i & \beta_i & -\alpha_i & -\beta_i \\ -\beta_i & \alpha_i & \beta_i & -\alpha_i \end{bmatrix} \begin{bmatrix} t_A^x \\ t_A^y \\ t_B^x \\ t_B^y \end{bmatrix} + \lambda \begin{bmatrix} f_{Li}^s \\ f_{Li}^n \end{bmatrix} - \begin{bmatrix} S_i \\ N_i \end{bmatrix} = - \begin{bmatrix} f_{Di}^s \\ f_{Di}^n \end{bmatrix} \quad (2.37)$$

and an average yield condition

$$\begin{bmatrix} 1 & \tan \phi_i \\ -1 & \tan \phi_i \end{bmatrix} \begin{bmatrix} S_i \\ N_i \end{bmatrix} \leq \begin{bmatrix} c_i l_i \\ c_i l_i \end{bmatrix} \quad (2.38)$$

respectively; where tensile forces are taken as positive. The relationship between discontinuity forces and the equivalent nodal forces is illustrated in Figure 2.10 using a simple example.

2.6.3.1 Adaptive nodal connection procedure

Millions of potential discontinuities may be required to obtain accurate solutions using DLO (Smith and Gilbert, 2007). The total number m_{all} of potential discontinuities grows disproportionately with n ; where m_{all} is bounded by $m_{all} \leq n(n-1)/2$. Solution of LP problems involving such large numbers of variables and constraints is not possible using the current generation of personal computers and LP solvers. Fortunately, the equilibrium formulation allows the yield condition to be checked on discontinuities not included in the original LP problem. This can be achieved by rearranging equation (2.37).

$$\begin{bmatrix} \tilde{S}_i \\ \tilde{N}_i \end{bmatrix} = \begin{bmatrix} \alpha_i & \beta_i & -\alpha_i & -\beta_i \\ -\beta_i & \alpha_i & \beta_i & -\alpha_i \end{bmatrix} \begin{bmatrix} t_A^x \\ t_A^y \\ t_B^x \\ t_B^y \end{bmatrix} + \lambda \begin{bmatrix} f_{Li}^s \\ f_{Li}^n \end{bmatrix} + \begin{bmatrix} f_{Di}^s \\ f_{Di}^n \end{bmatrix} \quad (2.39)$$

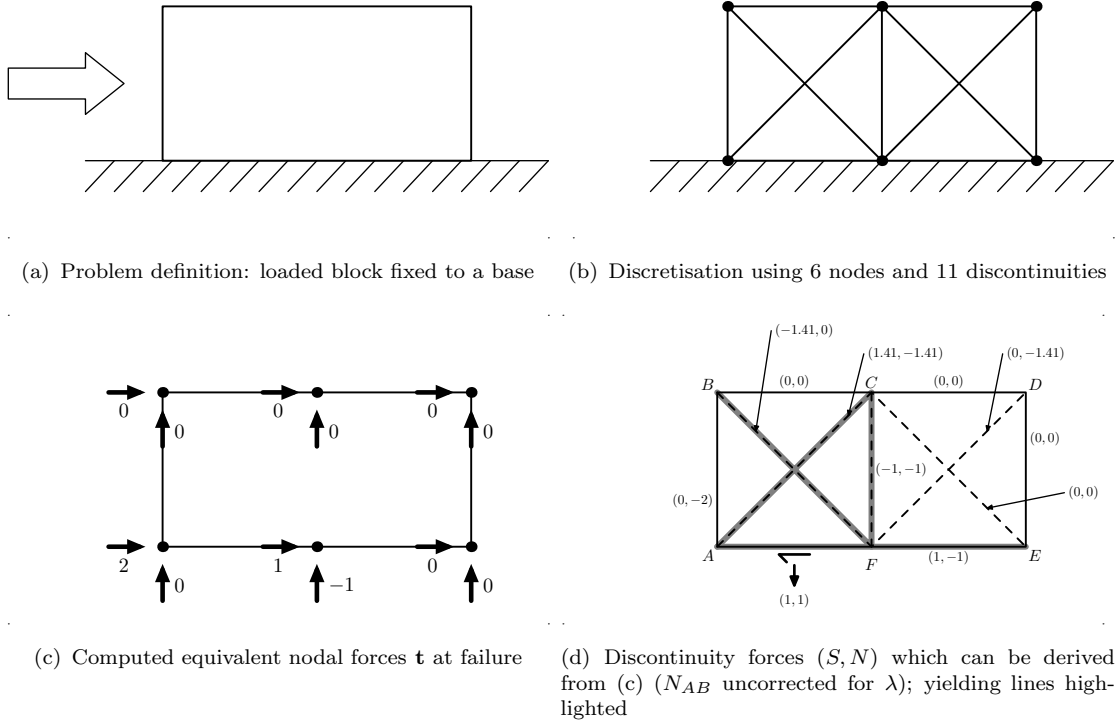


FIGURE 2.10: Relationship between discontinuity forces and equivalent nodal forces for a simple problem (2×1 unit block composed of weightless material possessing unit cohesive strength)(from Smith and Gilbert (2007))

where \tilde{S}_i and \tilde{N}_i are identical to S_i and N_i , respectively, but are not variables in the LP problem. \mathbf{f}_{Di} , \mathbf{f}_{Li} , α_i and β_i are purely functions of discontinuity geometry or problem specification and, therefore, known *a priori*. t_A^x , t_A^y , t_B^x , t_B^y and λ can be obtained by solving a LP problem including only a small subset of m_{all} ; therefore, \tilde{S}_i , \tilde{N}_i can be determined and violation of the yield condition, equation (2.38), checked. This procedure can be repeated for all discontinuities not included in the LP problem. The subset used in the LP problem must include at least one discontinuity per node; otherwise, t^x and t^y values will not be available at every node.

Smith and Gilbert (2007) developed an adaptive procedure, based on the philosophy of Gilbert and Tyas (2003), termed adaptive nodal connection, whereby a

percentage of the potential discontinuities most exceeding yield are added to the original LP problem. The procedure is then repeated using the new LP solution. The adaptive procedure can be summarised as follows:

- (i) select an initial subset of potential discontinuities;
- (ii) set up an LP problem using this initial set;
- (iii) solve the LP problem;
- (iv) check violation of the yield condition on discontinuities not include the LP problem;
- (v) add discontinuities most violating yield to the LP problem and repeat from (iii) or terminate adaptive procedure;

The adaptive procedure is terminated when no violations of the yield condition are detected on the discontinuities not included in the LP problem. Therefore, the final solution is a global optimum for the LP problem including all m_{all} discontinuities. Adaptive nodal connection allows efficient solution of problems involving very large numbers of potential discontinuities.

2.7 Three-dimensional limit analysis benchmarks

2.7.1 Introduction

One or more benchmarks testing the following scenarios are required for validation purposes.

- (i) Weightless cohesive soil ($\mathbf{c} > \mathbf{0}$, $\phi = \mathbf{0}$, $\gamma = \mathbf{0}$) – many cohesive problems are insensitive to self-weight and are, therefore, ideal for initial validation.
- (ii) Cohesive soil with self-weight ($\mathbf{c} > \mathbf{0}$, $\phi = \mathbf{0}$, $\gamma > \mathbf{0}$) – cohesive problems sensitive to self-weight are ideal for verifying self-weight is correctly applied.

- (iii) Frictional soil with self-weight ($\mathbf{c} = \mathbf{0}$, $\phi > \mathbf{0}$, $\gamma > \mathbf{0}$) – frictional problems allow dilation to be verified.
- (iv) Cohesive-frictional problem ($\mathbf{c} > \mathbf{0}$, $\phi > \mathbf{0}$, $\gamma \geq \mathbf{0}$)

where c is the cohesive strength, ϕ the angle of shearing resistance and γ the unit weight. The published literature has been reviewed to identify suitable three-dimensional benchmarks. Problems should be fully three-dimensional (*i.e.* not axially symmetrical or spherically symmetrical) and have simple geometry.

2.7.2 Bearing capacity

Geotechnical engineers have traditionally used the bearing capacity equation

$$q = c(s_c d_c N_c) + q_0(s_q d_q N_q) + \frac{1}{2}\gamma B(s_\gamma d_\gamma N_\gamma) \quad (2.40)$$

to determine the bearing capacity of shallow foundations; where N_c , N_q and N_γ are plane strain bearing capacity factors; s_c , s_q and s_γ are shape factors; d_c , d_q and d_γ are depth factors; B is the foundation width; q is the bearing pressure and q_0 is the overburden pressure. N_c , N_q and N_γ for a three-dimensional foundation will be redefined, henceforth, as $N_c = s_c d_c N_c$, $N_q = s_q d_q N_q$ and $N_\gamma = s_\gamma d_\gamma N_\gamma$, respectively, and equation (2.40) rewritten as

$$q = cN_c + q_0N_q + \frac{1}{2}\gamma BN_\gamma. \quad (2.41)$$

N_c , N_q and N_γ for a particular foundation geometry can be determined by considering ($c > 0$, $\phi = 0$, $\gamma = 0$, $q_0 = 0$), ($c = 0$, $\phi > 0$, $\gamma = 0$, $q_0 > 0$) and ($c = 0$, $\phi > 0$, $\gamma > 0$, $q_0 = 0$), respectively. Due to symmetry, only one-eighth of a square foundation (or punch) needs to be modelled. Therefore, a square foundation on the soil surface is a useful standard problem for validation purposes.

N_c ($c > 0$, $\phi = 0$, $\gamma = 0$, $q_0 = 0$)

The best available lower bound $N_c = 5.523$ and upper bound $N_c = 6.051$ are due to Salgado et al. (2004) and Vicente da Silva and Antão (2007, 2008), respectively. Salgado et al. (2004) used FELA to determine upper and lower bound N_c values for different combinations of foundation embedment and geometry. Vicente da Silva and Antão (2008) used FELA to determined upper bound N_c values for rectangular foundations on the soil surface. N_c is independent of self-weight and is, therefore, an ideal benchmark for the $c > 0$, $\phi = 0$ and $\gamma = 0$ scenario.

 N_q ($c = 0$, $\phi > 0$, $\gamma = 0$, $q_0 > 0$)

Michalowski (2001) used ‘horn’ shaped mechanisms to obtain upper bound N_q values; while Antão et al. (2012) used FELA to obtain upper bound N_q values. Lyamin et al. (2007) combined the last two terms of the bearing capacity formula to determine upper and lower bound values of s_q using FELA. The results of Lyamin et al. (2007) are not directly comparable with those of Michalowski (2001) and Antão et al. (2012). However, a large gap between available upper and lower bounds is suggested; consequently, N_q has not been selected.

 N_γ ($c = 0$, $\phi > 0$, $\gamma > 0$, $q_0 = 0$)

Michalowski (2001) used ‘horn’ shaped mechanisms to obtain upper bound N_γ values; while Antão et al. (2012) used FELA to determine upper bound N_γ values. Lyamin et al. (2007) and Krabbenhøft et al. (2008) used FELA to determined upper and lower bound N_γ values. N_γ has not been selected due the large gap (>25%) between published upper and lower bounds.

2.7.3 Compression of a block

Martin and Makrodimopoulos (2008) have obtained bounds for the unconfined compression of a block, shown in Figure 2.11, between two rough platens; the best bounds for which are presented in Table 2.4. The quantity of interest for this problem is the ratio q/c ; where q is the average bearing pressure. Both cases in

Table 2.4 have been selected for validating a new three-dimensional formulation. For ($c = 1$, $\phi = 30^\circ$, $\gamma = 0$), the gap between upper and lower bounds is large; however, the author is unaware of any alternative three-dimensional benchmarks for cohesive-frictional materials.

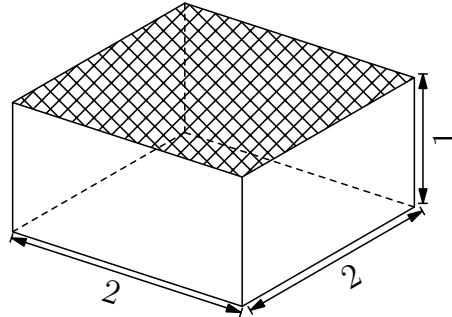


FIGURE 2.11: Compression of a block – relative dimensions

TABLE 2.4: Compression of a block – best published bounds (Martin and Makrodimopoulos, 2008)

c	$\phi(^{\circ})$	γ	Upper bound q/c	Lower bound q/c
1	0	0	2.305	2.230
1	30	0	10.06	8.352

2.7.4 Anchors

Cohesive soil ($c > 0$, $\phi = 0^\circ$, $\gamma \geq 0$)

The break-out factor

$$N_c = \frac{q}{c} = N_{c0} + \frac{\gamma H}{c} \quad (2.42)$$

for an anchor in cohesive soil; where N_{c0} is the break-out factor for a weightless material; H is the depth of embedment and q is the ultimate bearing pressure. The superposition of the self-weight term onto N_{c0} term is ideal for testing the correct application of self-weight (*i.e.* the $c > 0$, $\phi = 0^\circ$, $\gamma \geq 0$ scenario). Due to symmetry, only one-eighth of a square anchor needs to be modelled. Therefore, a square anchor at different depths of embedment is a useful standard problem for

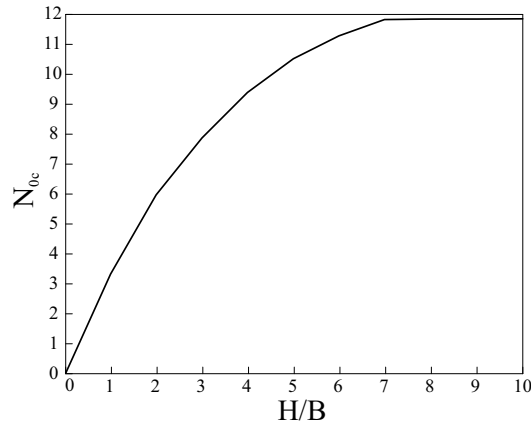


FIGURE 2.12: Lower bounds from Merifield et al. (2003) on the break-out factor N_{0c} for a square anchor in a weightless cohesive soil

validation purposes. Merifield et al. (2003) has obtained lower bound estimates of N_{c0} for rectangular, perfectly rough, anchors embedded at different H/B ratios; where B is the anchor width. Merifield et al. (2003)'s results for a square anchor are presented in Figure 2.12.

Frictional soil ($c = 0$, $\phi > 0^\circ$, $\gamma \geq 0$)

Merifield et al. (2006) determined lower bound estimates of the break-out factor $N_\gamma = q/\gamma H$ for square, perfectly rough, anchors at different depths of embedment H using FELA. Murray and Geddes (1987) proposed the upper bound

$$N_\gamma = 1 + \frac{H}{B} \tan \phi \left(2 + \frac{\pi}{3} H \tan \phi \right), \quad (2.43)$$

assuming a simple, rigid block mechanism; where B is the anchor width. These upper and lower bounds N_γ are presented in Figure 2.13. The problem of a square anchor embedded in a frictional soil has been selected for validation purposes as this allows consideration of the $c = 0$, $\phi > 0^\circ$, $\gamma \geq 0$ scenario.

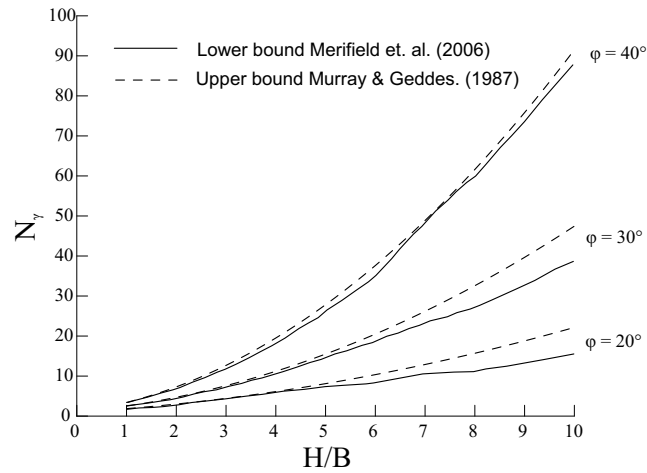


FIGURE 2.13: Break-out factors N_γ for a square anchor in a frictional soil

2.7.5 Slopes

Consideration of slope problems, generally, requires complex problem geometry (due to the foot of the slope). Slope problems have, therefore, been discarded for initial validation but may prove useful for additional validation. See Li et al. (2009), Michalowski and Drescher (2009), Michalowski (2010) and Chen et al. (2003) for examples of three-dimensional slope problems solved using limit analysis.

2.7.6 Summary

The following benchmarks have been selected as suitable for validation purposes:

- (i) $\mathbf{c} > \mathbf{0}$, $\phi = \mathbf{0}$, $\gamma = \mathbf{0}$ –
 - (a) bearing capacity of a square foundation or punch,
 - (b) unconfined compression of a square block between two rough platens;
- (ii) $\mathbf{c} > \mathbf{0}$, $\phi = \mathbf{0}$, $\gamma > \mathbf{0}$ – breakout of a square anchor;
- (iii) $\mathbf{c} = \mathbf{0}$, $\phi > \mathbf{0}$, $\gamma \geq \mathbf{0}$ – breakout of a square anchor;

- (iv) $\mathbf{c} > \mathbf{0}$, $\phi > \mathbf{0}$, $\gamma \geq \mathbf{0}$ – unconfined compression of a square block between two rough platens.

2.8 Conclusions

- (i) The upper and lower bound theorems of limit analysis allow an ‘exact’ collapse load to be bounded directly. The upper and lower theorems are conveniently framed as mathematical optimization problems; allowing numerical formulations of limit analysis to be solved using powerful optimization algorithms.
- (ii) The efficiency of a numerical direct method is largely determined by the optimization algorithm used. The choice of optimization algorithm is constrained by the dimensionality of the problem, yield surface and representation of the problem domain. Direct methods using a discontinuous representation of the problem domain can make use of simpler, more efficient optimization algorithms relative to continuous or hybrid methods.
- (iii) For certain classes of problem, the ability of direct methods to accurately model the discontinuities developing at failure is critical to the accuracy of solutions obtained. Discontinuous and hybrid continuous/discontinuous methods model these discontinuities directly. However, these methods are typically very sensitive to discontinuity orientation. Therefore, considerable insight into the form of the solution is required. Alternatively, complex adaptive schemes may be used. Discontinuity layout optimization (DLO) allows very large numbers of potential discontinuities at a wide range of orientations to be considered, overcoming this limitation.
- (iv) Plane strain DLO has successfully been tested against numerous benchmarks and allows consideration of complex boundary conditions. An adaptive procedure based on the dual, equilibrium formulation allows very large problems to be solved efficiently. The objective of the current research is to develop a three-dimensional formulation of DLO.

- (v) Three-dimensional benchmarks suitable for validation have been selected from the literature.

3 Application of discontinuity layout optimization to three-dimensional plasticity problems¹

In Chapter 2, the plane strain formulation of discontinuity layout optimization (DLO) was introduced. In plane strain, DLO is capable of obtaining accurate upper bounds on the collapse load at moderate computational expense. To date, no three-dimensional formulation of DLO has been developed. In the following sections, a new three-dimensional formulation of DLO is described in kinematic form. Firstly, the yield condition and flow rule on a three-dimensional discontinuity are examined. The three-dimensional formulation of DLO is then developed in kinematic form, considering compatibility and energy dissipation, where the discontinuities in this new formulation are polygonal rather than line segments (as plane strain). The new formulation is then summarized before validating the new formulation against the benchmark problems selected in Section 2.7.

¹based on Hawksbee, S., Smith, C. and Gilbert, M. (2013). “Application of discontinuity layout optimization to three-dimensional plasticity problems”, *Proc. R. Soc. A*, Vol. 469, pp. 1471-2946.

3.1 Yield condition on three-dimensional discontinuities

DLO is formulated entirely in terms of potential discontinuities and yield/deformation is only permitted along these potential discontinuities. Therefore in three-dimensions, DLO can be cast as a second order cone program (SOCP) (see Table 2.1).

It is now convenient to use an orthogonal coordinate system local to each discontinuity, comprising axes \mathbf{n} , \mathbf{s} and \mathbf{t} , where \mathbf{n} is a unit vector normal to the discontinuity and \mathbf{s} and \mathbf{t} are unit vectors in the plane of the discontinuity. Considering translational mechanisms, the Mohr-Coulomb yield criterion can now be enforced for stress resultants acting on the plane of the discontinuity by equations (3.1) and (3.2):

$$P + N \tan \phi \leq ac, \quad (3.1)$$

$$P = \sqrt{S^2 + T^2}, \quad (3.2)$$

where c and ϕ are the material cohesion and angle of shearing resistance and a is the face area of the discontinuity. N , S and T denote respectively the normal force and shear traction components along the \mathbf{n} , \mathbf{s} and \mathbf{t} axes respectively, and P is the maximum shear traction on the discontinuity, as indicated in Figure 3.1.

Similarly, the associative flow rule for a Mohr-Coulomb material can be expressed by equations (3.3) and (3.4):

$$p \tan \phi - n = 0, \quad (3.3)$$

$$p \geq \sqrt{s^2 + t^2}, \quad (3.4)$$

where n , s and t denote the component of the relative jump in displacement rate across the discontinuity in the \mathbf{n} , \mathbf{s} and \mathbf{t} directions respectively, and p is a plastic multiplier, as indicated in Figure 3.1. (Note that henceforth, ‘energy dissipation’ and ‘displacement’ will be used as shorthand for ‘rate of energy dissipation’ and

‘rate of displacement’, respectively.) Using equation (3.4), it is now possible to formulate three-dimensional DLO as a SOCP problem.

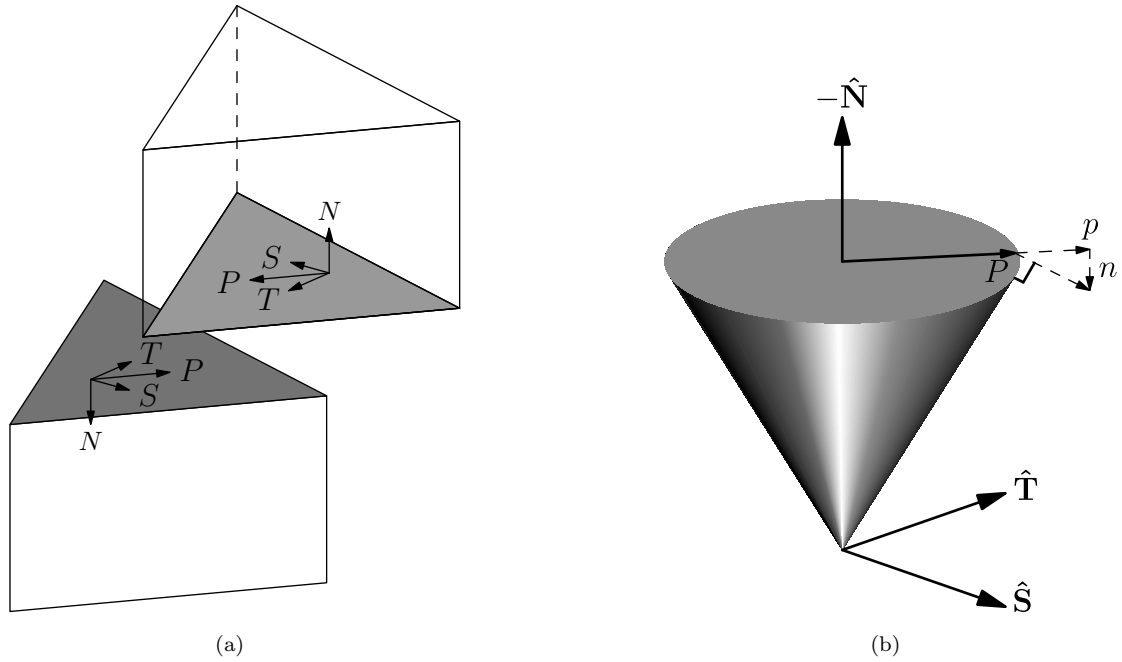


FIGURE 3.1: Mohr-Coloumb yield criteria: (a) yielding discontinuity between two rigid blocks showing: normal force N , resultant shear force P and its components S and T ; (b) conic yield surface, where \hat{N} is normal axis (tension positive) and \hat{S} and \hat{T} are orthogonal shear axes. The displacement jump orthogonal to the yield surface, is shown, where n is the normal component of the displacement jump and p is a plastic multiplier.

3.2 Three-dimensional formulation of DLO

In the following sections, a three-dimensional kinematic formulation of DLO is developed using a three-dimensional grid of nodes and polygonal discontinuities. While any simple polygonal shape or combination of simple polygonal shapes may be used for the discontinuities, triangular discontinuities provide the most flexibility and will be used in the numerical examples. However, for the purposes of explaining the method, discontinuities of both rectangular and triangular shape will be used. In general when using triangular discontinuities all combinations of

three nodes are connected to create a total of $n(n-1)(n-2)/6$ discontinuities, where n is the total number of nodes used to discretize the problem (cf. a total of $n(n-1)/2$ discontinuities in plane strain problems). As in plane strain problems, this results in a rich field of potential translational mechanisms and reduces the need to refine the mesh in the region of singularities.

3.2.1 Compatibility

A scheme guaranteeing compatibility is required. In plane strain DLO, compatibility is enforced on a nodal basis. In three-dimensional DLO, compatibility is conveniently enforced along shared edges. Figure 3.2 shows a set of triangular prisms sharing a common edge OO' and with absolute displacements, \mathbf{v}_{AB} to \mathbf{v}_{EA} . The prisms are separated by rectangular discontinuities $O'OXX'$, where $X = A, B \dots E$. Each discontinuity $O'OXX'$ has a normal \mathbf{n}_X and a relative displacement jump $\Delta\mathbf{v}_X$ that denotes the difference in absolute displacement of the prisms meeting at this discontinuity. It follows from this definition that Equation (3.5), which involves summing all relative displacement jumps around edge OO' , must hold:

$$(\mathbf{v}_{EA} - \mathbf{v}_{AB}) + (\mathbf{v}_{AB} - \mathbf{v}_{BC}) + (\mathbf{v}_{BC} - \mathbf{v}_{CD}) + (\mathbf{v}_{CD} - \mathbf{v}_{DE}) + (\mathbf{v}_{DE} - \mathbf{v}_{EA}) = \mathbf{0} \quad (3.5)$$

A sign convention for determining the directions of \mathbf{n}_A to \mathbf{n}_E and $\Delta\mathbf{v}_A$ to $\Delta\mathbf{v}_E$ is presented in Appendix A. Using this sign convention and the vertex ordering in Figure 3.2(b), the following must also be true along edge OO' :

$$\Delta\mathbf{v}_A + \Delta\mathbf{v}_B + \Delta\mathbf{v}_C + \Delta\mathbf{v}_D + \Delta\mathbf{v}_E = \mathbf{0} \quad (3.6)$$

Compatibility can be similarly enforced along the remaining edges, using the sign convention given in Appendix B. Moreover, equation (3.6) can be reformulated along edge j ($j = 1, 2, \dots, l$) in terms of coordinate systems local to each discontinuity i and defined as follows:

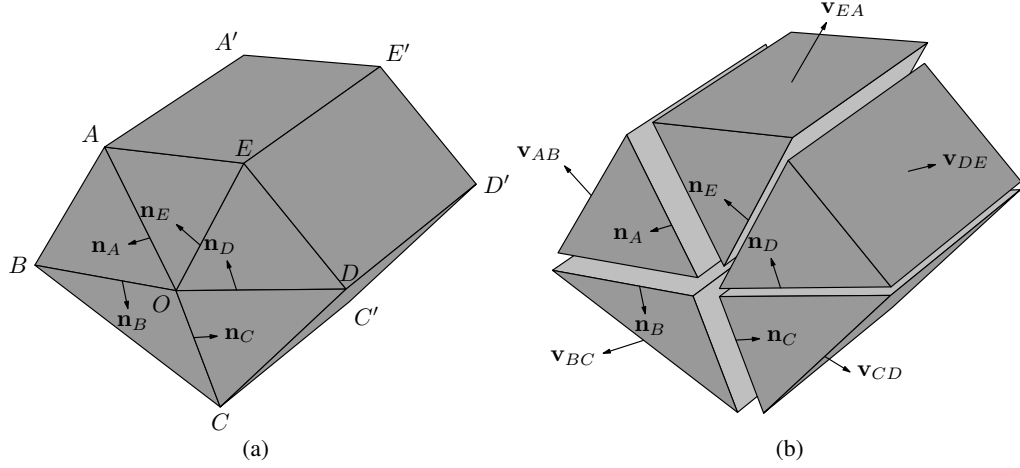


FIGURE 3.2: Solid bodies meeting at a common edge, (a) prior to, and (b) after movement, with prisms separated by discontinuities $\overrightarrow{O'OX'X'}$, where $X = A, B \dots E$. For clarity O' has not been shown, but lies in in the plane $A'B'C'D'E'$.

$$\sum_{i \in S_j} \mathbf{B}_{ij} \mathbf{d}_i = \mathbf{0} \quad (3.7)$$

where l is the total number of edges used to discretize the problem; S_j is a subset of the total number of discontinuities m and contains all discontinuities meeting at edge j .

$$\mathbf{d}_i = \mathbf{T}_i^T \Delta \mathbf{v}_i; \quad (3.8)$$

where \mathbf{T}_i is a 3×3 transformation matrix converting local to global displacement jumps. \mathbf{T}_i is chosen such that one axis aligns with \mathbf{n}_i , the unit column vector in the normal direction using the ‘righthand screw rule’; the two remaining orthogonal axes, \mathbf{s}_i and \mathbf{t}_i , are in plane of discontinuity i such that $\mathbf{T}_i = \{\mathbf{n}_i \ \mathbf{s}_i \ \mathbf{t}_i\}$. And where $\mathbf{d}_i = \{n_i \ s_i \ t_i\}^T$, where n_i , s_i and t_i are the local displacement jumps across discontinuity i in the \mathbf{n}_i , \mathbf{s}_i and \mathbf{t}_i directions respectively. \mathbf{B}_{ij} is a local compatibility matrix equal to $k_{ij} \mathbf{T}_i$, where the k_{ij} is defined in Appendix B.

The DLO procedure results in intersections and overlaps between discontinuities that do not coincide with nodal connections, however compatibility at these is inherently enforced, as demonstrated in Appendix C.

3.2.2 Flow rule

The local coordinate system described allows the associative flow rule for a Mohr-Coulomb material to be enforced using equations (3.3) and (3.4). Taking advantage of SOCP, the flow rule on a discontinuity i can be restated as follows:

$$p_i \tan \phi_i - n_i = 0 \quad (3.9)$$

$$p_i \geq \sqrt{s_i^2 + t_i^2} \quad (3.10)$$

where p_i is a plastic multiplier; ϕ_i is the angle of friction on discontinuity i . Equation (3.9) is a linear constraint and equation (3.10) is a second order cone. In matrix form equation (3.9) can be stated as follows:

$$\mathbf{N}\mathbf{p} - \mathbf{d}_n = \mathbf{0} \quad (3.11)$$

where \mathbf{d}_n is a subset of \mathbf{d} containing only the displacement jumps normal to discontinuities i ($i = 1, \dots, m$), \mathbf{p} is a global vector containing plastic multipliers and m is now the total number of discontinuities in the problem. \mathbf{N} is a global $m \times m$ matrix enforcing the flow rule and equal to $\text{diag}(\tan \phi_1, \tan \phi_2, \dots, \tan \phi_m)$. It is noted that it is not always necessary to apply constraint equations (3.9) and/or (3.10). The relevant combinations are summarized shown in the first half of Table 3.1.

3.2.3 Dissipation function

The energy dissipated on a given discontinuity i is simply $g_i p_i$, where g_i is a dissipation coefficient equal to $\int_i c \, da$, the integral of the cohesive strength over the area a of discontinuity i . In the case of uniform cohesive strength across

TABLE 3.1: Discontinuity flow rule conditions - applicable constraints and variables

	Constraints		Variables		
	Eq. (3.9)	Eq. (3.10)	n_i	s_i & t_i	p_i
Interior discontinuity					
$\phi_i > 0, c_i \geq 0$	•	•	•	•	•
$c_i, \phi_i = 0$				•	
$c_i > 0, \phi_i = 0$		•		•	•
Boundary discontinuity					
free			•	•	
symmetry				•	
rigid	•	•	•	•	•

discontinuity i , the dissipation coefficient $g_i = a_i c_i$, where a_i and c_i are respectively the area and cohesion of the discontinuity.

On overlapping regions, the upper bound nature of the solution is maintained, as demonstrated in Appendix C.2.

3.2.4 Mathematical formulation

A three-dimensional kinematic formulation for a cohesive-frictional body discretized using m polygonal discontinuities and l edges can be summarised as follows:

$$\min \lambda \mathbf{f}_L^T \mathbf{d} = -\mathbf{f}_D^T \mathbf{d} + \mathbf{g}^T \mathbf{p} \quad (3.12)$$

subject to

$$\mathbf{B}\mathbf{d} = \mathbf{0} \quad (3.13)$$

$$\mathbf{N}\mathbf{p} - \mathbf{d}_n = \mathbf{0} \quad (3.14)$$

$$\mathbf{f}_L^T \mathbf{d} = \mathbf{1} \quad (3.15)$$

$$p_i \geq \sqrt{s_i^2 + t_i^2} \quad \forall i \in \{1, \dots, m\} \quad (3.16)$$

where \mathbf{f}_D and \mathbf{f}_L are vectors containing, respectively, the specified dead and live loads; \mathbf{d} contains displacement jumps across the discontinuities, $\mathbf{d}^T = \{n_1, s_1, t_1, n_2, s_2, t_2, \dots, t_m\}$, where n_i is the displacement jump normal to discontinuity i and s_i and t_i are the displacement jumps within the plane of discontinuity i ; \mathbf{g} is a vector of dissipation coefficients. \mathbf{B} is a suitable $3l \times 3m$ compatibility matrix; \mathbf{N} is a suitable $m \times m$ flow matrix; \mathbf{d}_n (a subset of \mathbf{d}) is a vector containing the normal displacement jumps, $\mathbf{d}_n^T = \{n_1, n_2, \dots, n_m\}$; and \mathbf{p} is a vector of plastic multipliers, $\mathbf{p}^T = \{p_1, p_2, \dots, p_m\}$, where p_i is the plastic multiplier for discontinuity i given by equation (3.16). The optimization variables are the displacement jumps in \mathbf{d} (and \mathbf{d}_n) and the plastic multipliers in \mathbf{p} . The objective function and the first three constraints are linear. The final constraints on the plastic multipliers p_i are second order cones, so that the formulation is amenable to solution using SOCP. The problem can also be posed in an equilibrium form, established using duality principles (see e.g. Boyd and Vandenberghe (2004)).

3.2.5 Boundary conditions and loads

Many common boundary conditions can readily be modelled by using a reduced number of variables and constraints, as indicated in Table 3.1. This shows that a discontinuity on a rigid boundary is dealt with in exactly the same manner as a discontinuity in the interior of a domain.

Dead and live loads \mathbf{f}_D^T and \mathbf{f}_L^T , in equations (3.12) and (3.15), are now defined such that $\mathbf{f}_D^T = \{f_{D1}^n, f_{D1}^s, f_{D1}^t, f_{D2}^n, \dots, f_{Dm}^t\}$ and $\mathbf{f}_L^T = \{f_{L1}^n, f_{L1}^s, f_{L1}^t, f_{L2}^n, \dots, f_{Lm}^t\}$, where f_{Di}^n , f_{Di}^s , f_{Di}^t and f_{Li}^n , f_{Li}^s , f_{Li}^t are, respectively, the dead and live loads

acting in the \mathbf{n}_i , \mathbf{s}_i and \mathbf{t}_i directions on discontinuity i . Areas of flexible loading can be applied directly to the discontinuities with no special treatment. Rigid loads can be applied using a discontinuity covering the whole loaded area and reducing the degrees of freedom of underlying discontinuities appropriately.

At an external boundary, after taking account of any overlapping regions, displacement jumps must equal the absolute displacement of that boundary. Hence \mathbf{f}_{Di} and \mathbf{f}_{Li} are simply the local dead and live loads on discontinuity i resolved to the local coordinate system when applied at boundary discontinuity i . For discontinuities within a body, the contents of \mathbf{f}_{Di} and \mathbf{f}_{Li} can be obtained by summing up the total overlying dead or live loads, excluding boundary loads. For example, for the case where dead loads are due to self weight only, and this is applied in the negative z direction, the contribution to the summation made by discontinuity i is as follows:

$$\mathbf{f}_{Di}^T \mathbf{d}_i = \mathbf{W}_i \mathbf{d}_i, \quad (3.17)$$

where \mathbf{W}_i is a 1×3 row vector containing the components in the \mathbf{n}_i , \mathbf{s}_i and \mathbf{t}_i directions of the total weight of the column lying vertically above discontinuity i .

3.2.6 Summary of procedure

Steps in the DLO procedure for three-dimensional problems can be summarised as follows:

- (i) discretize the problem using nodes;
- (ii) connect nodes to create edges;
- (iii) join edges to create polygonal discontinuities;
- (iv) set up problem, using equations (3.12) - (3.16);
- (v) solve the resulting SOCP problem.

3.3 Numerical Examples

In order to verify the potential of the method, various three-dimensional examples are now considered (*i.e.* the benchmarks selected in Section 2.7). All computations were performed using 2.6 GHz AMD Opteron 6140 processors equipped with 8 GB RAM and running 64 bit Scientific Linux. The MOSEK interior point solver with SOCP capability was used (Mosek, 2011). The default settings of the optimizer were used, including the pre-solve feature. The CPU times reported are for the optimizer only and include the optimizer's pre-solve routine, but exclude the time taken to read in and set up a given problem.

Prior to solving, various measures were taken to condition and/or reduce the size of a given problem. Firstly the coefficients in the objective function (3.12) and unit displacement constraint (3.15) were scaled to ensure the problem was well posed. Secondly, as overlapping edges do not provide any extra degrees of freedom, these were removed. Thirdly, discontinuities covering areas which could be reconstructed by combining several discontinuities covering smaller areas were removed. Fourthly, noting that the formulation naturally results in $3(n - 1)$ linear dependencies in the constraint matrix, where n is the total number of nodes, such linear dependencies were identified and removed prior to passing the problem to the optimizer. Lastly, while the basic DLO procedure involves positioning nodes on a Cartesian grid, the use of other nodal arrangements is possible, and, where clearly indicated, regular grids with differing x , y and z spacings are used in this paper. However, it should be noted that an adaptive solution procedure capable of dramatically reducing problem size (of the sort described in Smith and Gilbert (2007) for plane strain problems) was not utilized. Thus the size of a problem increases rapidly as nodal resolution is increased, and consequently details of only relatively small problems are reported here.

3.3.1 Compression of a block

The unconfined compression of a square block with shear strength parameters c , ϕ between two perfectly rough rigid platens (see Section 2.7.3) has previously been considered by Martin and Makrodimopoulos (2008), who have obtained upper and lower bound solutions which can be used to benchmark the proposed 3D DLO procedure. For the geometry shown in Figure 3.3, the objective is to find the ratio of the average bearing pressure q to cohesive shear strength c .

Symmetry means that only one-sixteenth of the block needs to be modelled, as indicated in Figure 3.3. Nodes were initially positioned on a Cartesian grid (equal nodal spacings in the x , y and z directions) and solutions are presented in Table 3.2, along with the results obtained by Martin and Makrodimopoulos (2008) taken as benchmark. For $\phi = 0^\circ$, the new solutions presented are close (within 0.39%) to the benchmark upper bound solutions of Martin and Makrodimopoulos (2008). A representative collapse mechanism is shown in Figure 3.4. In the case of $\phi = 30^\circ$, the new solution compares less favourably with the benchmark (diff. 10%).

Noting that the active discontinuities in Figure 3.4 radiate from the centre, the use of different nodal spacings for $\phi = 0^\circ$ have been used in the x direction to those in the y and z directions. By reducing nodal spacings in the x direction and increasing them in the y and z directions, it has been possible to improve on the upper bound obtained by Martin and Makrodimopoulos (2008). Results for various nodal spacings are presented in Table 3.3.

Firstly it is evident that a solution matching the best reported value of 2.314 presented previously could be obtained in only 0.22 seconds (Table 3.3), compared with 9700 seconds previously (Table 3.2). This is because only a small subset of the discontinuities present previously are now present. Secondly it is evident that it has been possible to improve on the upper bound obtained by Martin and Makrodimopoulos (2008).

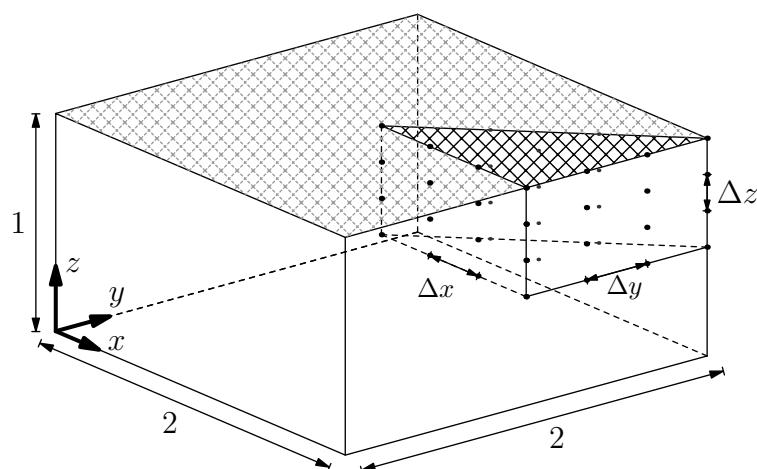


FIGURE 3.3: Compression of a block – problem geometry, nodal spacings Δx , Δy and Δz , and one-sixteenth of the problem taking advantage of symmetry

TABLE 3.2: Compression of a $2 \times 2 \times 1$ unit block (as depicted in Figure 3.3) - comparison with benchmark solutions

ϕ ($^\circ$)	Benchmark		Spacing Δ	Discontinuities		Solution	Diff (%)	CPU (s)
	UB	LB		Total no.	Active (%)			
0	2.305	2.230	$1/4$	7,704	2.7	2.319	0.60	12
			$1/6$	117,936	2.7	2.314	0.39	9,700
30	10.06	8.352	$1/4$	7,704	10	12.48	18	2.0
			$1/6$	117,936	4.0	11.69	10	5,000

Key: UB & LB = upper & lower bound solutions from Martin and Makrodimopoulos (2008); the UB has been used to benchmark the present solutions; $\Delta = \Delta x = \Delta y = \Delta z$.

3.3.2 Punch indentation

The bearing capacity of a perfectly rough square indenter resting on the surface of a purely cohesive Tresca material is now considered (see Section 2.7.2). The value of interest is once again the ratio q/c , otherwise known as the bearing capacity factor N_c . Salgado et al. (2004) have established upper and lower bounds for a variety of indenter embedment depths and geometries using finite element limit analysis. Michalowski (2001) and Vicente da Silva and Antão (2008) have also established upper bounds for a number of indenter geometries bearing onto the

TABLE 3.3: Compression of a $2 \times 2 \times 1$ unit block (as depicted in Figure 3.3) - use of different nodal grid spacings

ϕ ($^\circ$)	Benchmark		Spacing $\Delta y, \Delta z$	Discontinuities		Solution	Diff %	CPU (s)
	UB	LB		Total no.	Active (%)			
0	2.305	2.230	$1/4$	356	29	2.319	0.60	0.04
			$1/6$	1,500	30	2.314	0.39	0.22
			$1/8$	4,452	26	2.309	0.18	1.9
			$1/12$	23,100	21	2.307	0.072	50
			$1/18$	133,884	16	2.304	-0.043	1,800

Key: UB & LB = upper & lower bound solutions from Martin and Makrodimopoulos (2008); the UB has been used to benchmark the present solutions; $\Delta x = 1$.

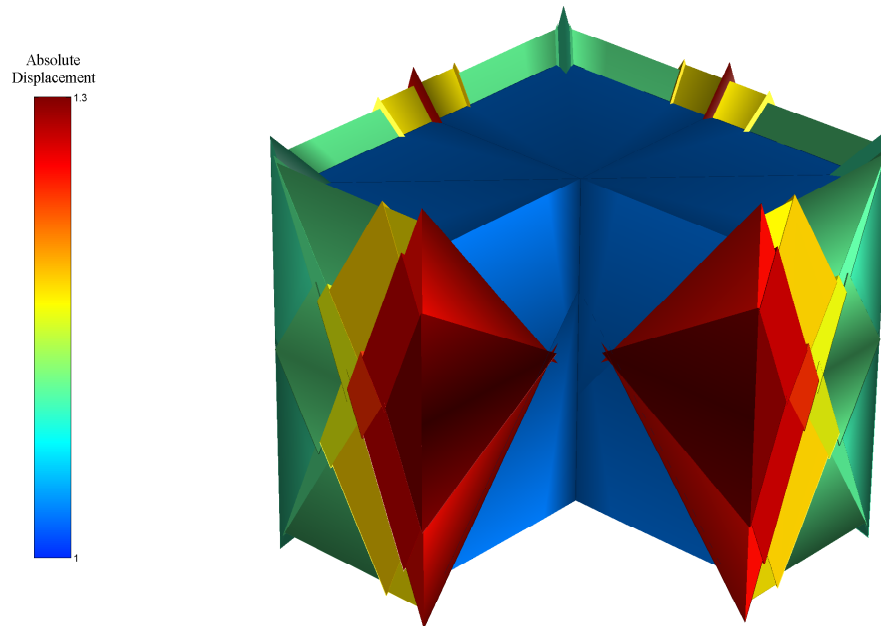


FIGURE 3.4: Compression of a $2 \times 2 \times 1$ unit block (as depicted in Figure 3.3) - typical failure mechanism for $\phi = 0^\circ$ case ($\Delta x, \Delta y, \Delta z = \frac{1}{4}$)

material surface. The best reported upper and lower bounds for a square indenter are included in Table 3.4.

The problem geometry used is shown in Figure 3.5. Taking advantage of symmetry, only one-eighth of the problem needs to be modelled, as shown in Figure

3.5. Table 3.4 presents new solutions for three nodal spacings, with all nodes positioned on a Cartesian grid (equal nodal spacings in the x , y and z directions). These solutions compare well with the best reported upper bound, especially considering the comparatively low nodal resolutions employed. A representative failure mechanism is shown in Figure 3.6. It should be noted that the critical mechanisms for all three nodal grids extend up to the fixed boundaries. However, extending the problem domain relative to the foundation quickly leads to impractically large problem sizes, so this issue was not investigated further.

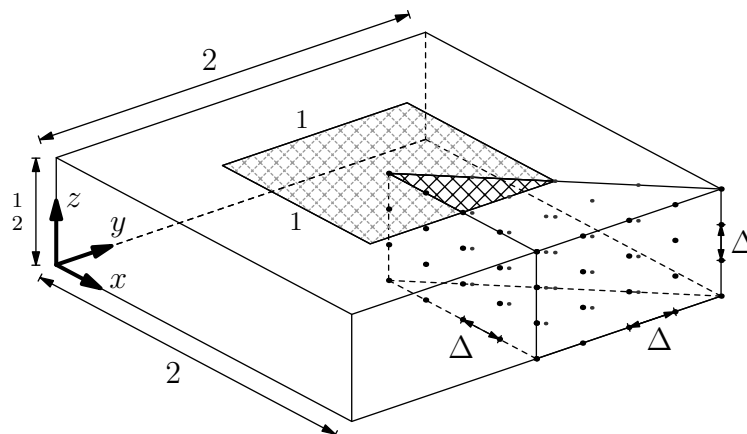


FIGURE 3.5: Punch indentation – problem geometry, nodal spacing Δ and one-eighth of the problem taking advantage of symmetry

TABLE 3.4: Indentation of a 1×1 unit punch (as depicted in Figure 3.5) - comparison with benchmark solutions

Benchmark		Spacing	Discontinuities		Solution	Diff	CPU
UB	LB	Δ	Total no.	Active (%)		%	(s)
6.051	5.52	$1/2$	157	17	6.521	7.8	0.02
		$1/4$	7,365	4.6	6.405	5.9	13
		$1/6$	114,310	1.6	6.226	2.9	6,400

Key: UB & LB = upper & lower bound solutions respectively from Vicente da Silva and Antão (2008) and Salgado et al. (2004); the UB has been used to benchmark the present solutions.

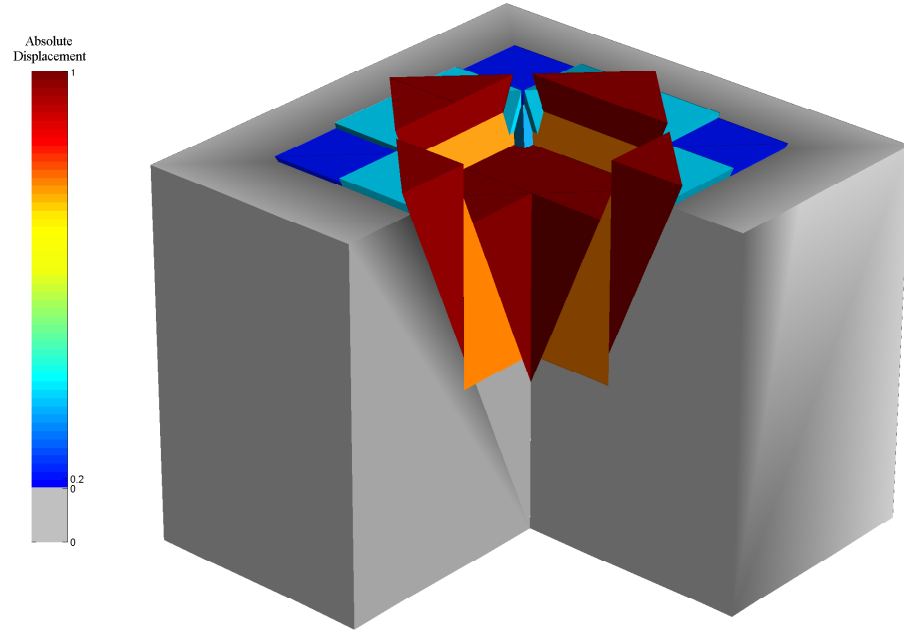


FIGURE 3.6: Indentation of a 1×1 unit punch (as depicted in Figure 3.5) - representative failure mechanism ($\Delta = \frac{1}{2}$, $\phi = 0$) (Note for presentation the extent of the stationary region has been increased)

3.3.3 Anchor in a purely cohesive soil ($\phi = 0$)

Consider a perfectly rough anchor of width B embedded at a depth H in a purely cohesive Tresca soil (see Section 2.7.4), as shown in Figure 3.7. Immediate break-away (no suction or transmission of tensile stresses) is assumed between the anchor base and the soil. Taking advantage of symmetry, only one-eighth of the problem needs to be modelled, as shown in Figure 3.7. Various H/B ratios have been considered by fixing $B = 2$, $W = 10$, $\Delta x = \Delta y = 1$, $\Delta z = H/4$ and varying H .

Merifield et al. (2003) used lower bound finite element limit analysis to establish bounds on the break-out factor at various embedment depths. The break-out factor N_{c0} for an anchor in a weightless cohesive soil is defined as average bearing pressure q divided by the cohesive strength c . For a soil with unit weight γ , Merifield et al. (2003) defined the break-out factor $N_{c\gamma}$ as:

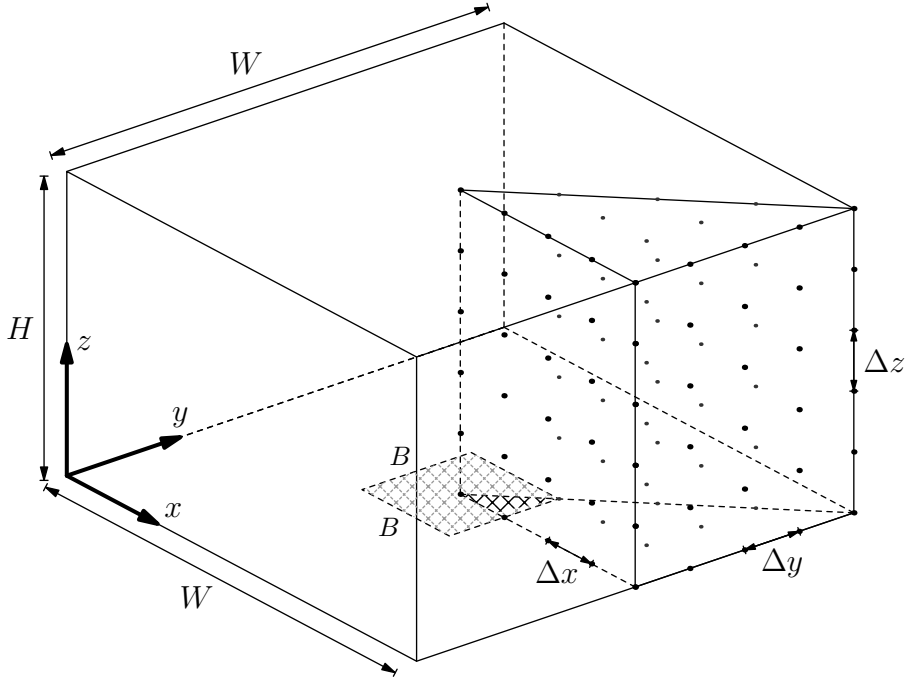


FIGURE 3.7: Anchor – problem geometry, nodal spacings, Δx , Δy and Δz , and the one-eighth of the volume modelled, due to symmetry

$$N_{c\gamma} = N_{c0} + \frac{\gamma H}{c} \quad (3.18)$$

Failure mechanisms can be classified as ‘shallow’, where the failure mechanism extends up from the anchor to the soil surface, and ‘deep’, where the mechanism involves only localized deformations around the anchor, and where the break-out factor N_{c*} is independent of the embedment depth H . For a given ratio γ/c , the deep mechanism becomes critical at depths greater than or equal to H_{cr} . If both deep and shallow mechanisms are considered, $N_{c\gamma}$ must be less than or equal to N_{c*} . Merifield et al. (2003) established a lower bound on $N_{c*} \approx 11.9$. For $\gamma/c = 0$, Merifield et al. (2003) found $H_{cr} \approx 7$.

Figure 3.8 shows break-out factors for shallow failures at various embedment depths. These show good agreement with those of Merifield et al. (2003) when $\gamma/c = 0$ and $H < H_{cr}$. Furthermore the results for $\gamma/c = 1$ and $\gamma/c = 2$ are consistent with the relationship described in equation (3.18). The mechanisms

developed did not extend to the lateral fixed boundary, suggesting that N_c and $N_{c\gamma}$ were not influenced by the extent of the domain modelled.

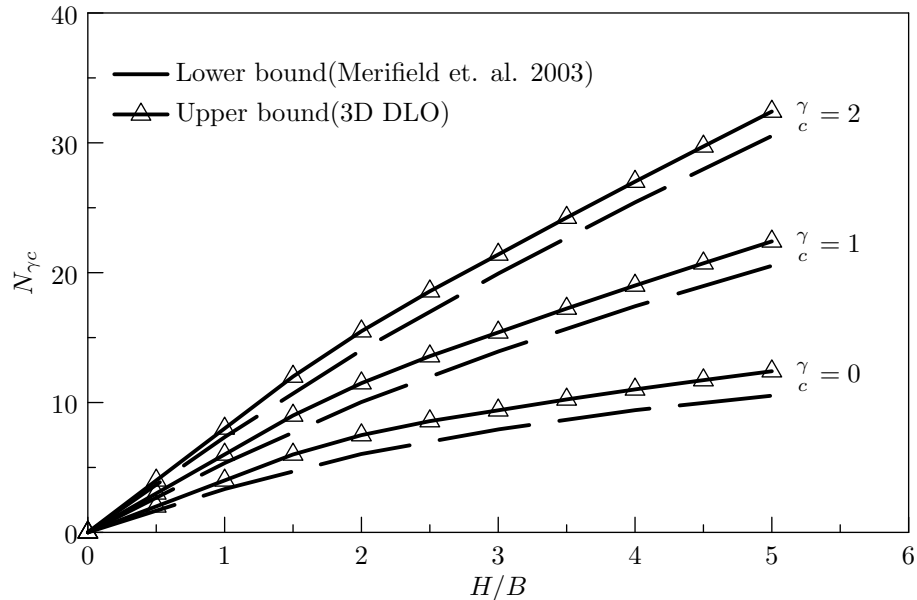


FIGURE 3.8: Anchor in cohesive soil - break-out factors

3.3.4 Anchor in a purely frictional soil

Now, consider a perfectly rough anchor of width B embedded at depth H in a purely frictional soil with an angle of friction $\phi = 30^\circ$ and a unit self weight γ (see Section 2.7.4). Assuming an associative flow rule, only mechanisms that extend to the surface are possible. The break-out factor N_γ in this case can be expressed as:

$$N_\gamma = \frac{q}{\gamma H} \quad (3.19)$$

where q is the average pressure on the anchor. Merifield et al. (2006) used a lower bound finite element analysis procedure to establish bounds on the break-out factor for various angles of friction and embedment depths. Murray and Geddes

(1987) proposed the upper bound in equation (3.20), assuming a simple rigid block mechanism.

$$N_\gamma = 1 + \frac{H}{B} \tan \phi \left(2 + \frac{\pi}{3} H \tan \phi \right) \quad (3.20)$$

Using nodal grids of the general form in Figure 3.7 and fixing $B = 2$, $W = 10$, $\Delta x = \Delta y = 1$, $\Delta z = H/4$ (denoted GRID 1) and varying H , a very close fit, shown in Figure 3.9, to equation (3.20) has been found for $0.5 \leq H/B \leq 2.5$. Above this range, the mechanism reaches the lateral fixed boundary and no solution was obtained. The critical mechanism is relatively simple and very similar results can be obtained using an alternative grid, where $B = 2$, $W = 16$, $\Delta x = \Delta y = 1$, $\Delta z = H$ (denoted GRID 2). GRID 2 also has been used to determine N_γ for $2.5 < H/B \leq 5$, which also compare well with equation (3.20).

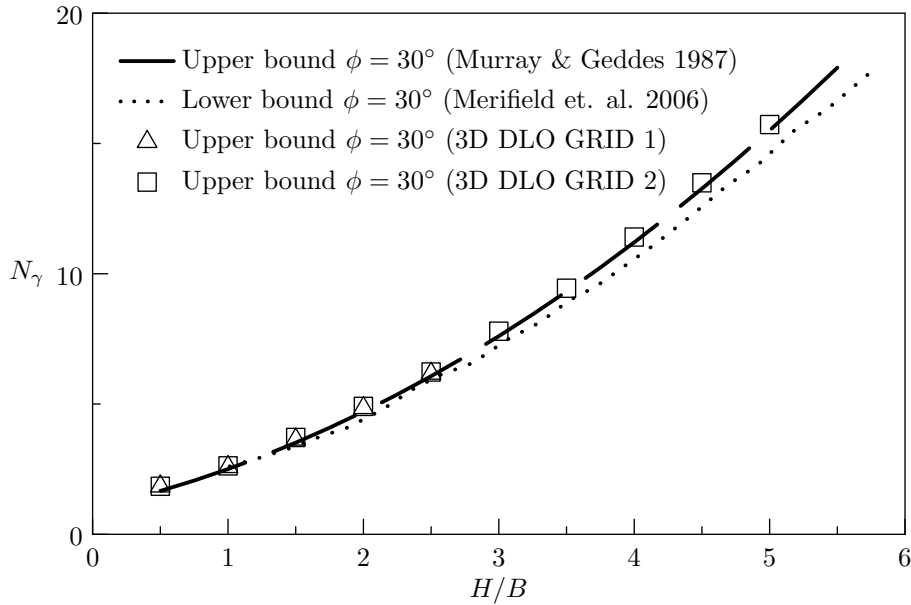


FIGURE 3.9: Break-out factors for a square anchor in frictional soil using two different nodal grids: GRID 1 and GRID 2

3.4 Discussion

As can be seen in the previous section, three-dimensional DLO is capable of obtaining results comparable with those found in the literature. In one case, an improved upper bound solution was obtained. However, refining the nodal grid even slightly leads to a large increase in the number of potential discontinuities, and problems quickly become impractically large using currently available computational power, and enhancements to improve performance are required.

3.5 Conclusions

- (i) A new three-dimensional kinematic formulation of discontinuity layout optimization (DLO) has been described that can be used to solve general three-dimensional plasticity problems. In this new formulation, unlike the existing plane strain formulation, compatibility is enforced along the edges between discontinuities. The formulation makes use of efficient second order cone programming to handle the Mohr-Coulomb flow rule, and to directly determine optimal translational collapse mechanisms. These collapse mechanisms are based on an optimal subset of planar discontinuities drawn from a large set of potential planar triangular discontinuities whose corners are located on nodes within a three-dimensional grid of nodal points in the problem domain.
- (ii) Good correlation was found with benchmarks available in the literature despite the low nodal resolutions employed. The best reported upper bound for the compression of a purely cohesive block between two perfectly rough platens was improved upon.

4 Plane strain stress functions

4.1 Introduction

In Chapter 3, a three-dimensional discontinuity layout optimization (DLO) formulation was developed. In the kinematic formulation presented, the sum of the energy dissipated in the material and the work done by the dead loads was minimized. However, an equivalent problem, maximizing the load factor applied to the live loads, can be derived from duality principles. Valuable insights into the plane strain DLO formulation have been gained by understanding the dual form of the plane strain formulation (see Section 2.6.3). Direct derivation of the three-dimensional dual formulation from first principles appears to have the potential to lead to similar insights, potentially allowing more efficient solution schemes to be developed. However, before proceeding to investigate the three-dimensional formulation in more detail, the dual, equilibrium, plane strain formulation will be explored.

Smith and Gilbert (2007) used linear programming duality principles to derive the equilibrium plane strain DLO formulation. This appears to resemble a traditional lower bound formulation, but in fact produces upper bound solutions identical to those obtained using the primal, kinematic, formulation. In the following sections, the plane strain equilibrium formulation will be derived again but here using vector calculus (see Appendix D) and so-called ‘stress functions’. Differences between the plane strain equilibrium formulation and formulations complying with the lower bound theorem will be explored, and relaxed lower bounds, referred to as pseudo lower bounds, developed. In Chapter 5, a similar derivation will be employed to

find the dual of the three-dimensional formulation, and to develop a pseudo lower bound method.

4.2 Background

4.2.1 Equilibrium equations

A body in plane strain equilibrium must satisfy the following equilibrium equations

$$\nabla \cdot \boldsymbol{\sigma}^x + p_x = 0 \quad (4.1)$$

$$\nabla \cdot \boldsymbol{\sigma}^y + p_y = 0 \quad (4.2)$$

$$\sigma_{xy} = \sigma_{yx} \quad (4.3)$$

where p_x and p_y are components of body force in the x and y directions, respectively;

$$\boldsymbol{\sigma}^x = \sigma_{xx}\mathbf{i} + \sigma_{yx}\mathbf{j}; \quad (4.4)$$

$$\boldsymbol{\sigma}^y = \sigma_{xy}\mathbf{i} + \sigma_{yy}\mathbf{j}; \quad (4.5)$$

and the sign convention is given by Figure 4.1. Equation (4.3) requires that the stress tensor

$$\boldsymbol{\sigma} = \begin{bmatrix} \sigma_{xx} & \sigma_{xy} \\ \sigma_{yx} & \sigma_{yy} \end{bmatrix} \quad (4.6)$$

must be symmetric.

4.2.2 Translational equilibrium

In simple upper bound methods, rotational mechanisms are often assumed not to occur. For example, a classical Coulomb wedge mechanism is shown in Figure 4.2. Here the wedge is assumed to slide along a straight rupture surface, and

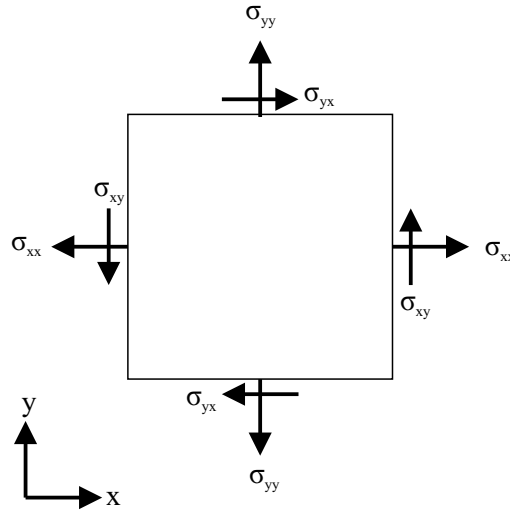


FIGURE 4.1: Sign convention: plane strain stress components

therefore only translational movements are involved. For sake of simplicity assuming a weightless Tresca material, the limiting surface load F on the wedge in translational equilibrium can be found from

$$S \cos \theta - N \sin \theta = 0 \quad (4.7)$$

$$F = S \sin \theta + N \cos \theta \quad (4.8)$$

where S and N are the shear and normal forces on the rupture surface. A further check, taking moments about a point, is necessary to ensure rotational equilibrium. However, the true limit analysis collapse load for this problem can be found from equations (4.7) and (4.8) by varying angle θ to find minimum F and setting $S = cl$, where c is the shear strength of the soil and l the length of the rupture surface.

This approach is equivalent to equating the energy dissipated along the rupture surface to the work done by F .

In equilibrium terms, equations (4.7) and (4.8) are equivalent to enforcing equations (4.1) and (4.2). However, equation (4.3) and, therefore, symmetry of the stress tensor σ is not enforced. In which case, the Mohr's circle representation of

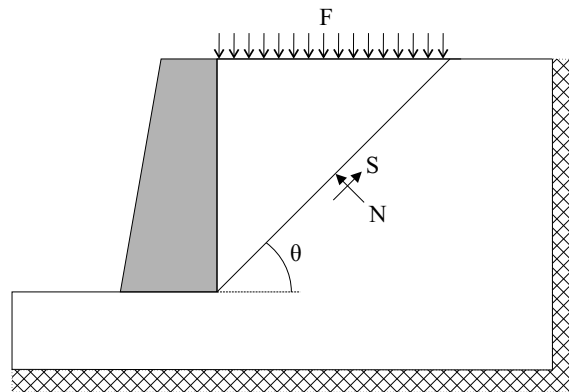


FIGURE 4.2: Coulomb wedge for a cohesive soil behind a smooth wall

the stress state (assumed the same everywhere) is displaced a distance

$$h = \frac{1}{2}(\sigma_{yx} - \sigma_{xy}) \quad (4.9)$$

above or below the normal stress σ -axis as shown in Figure 4.3 (see, for example, Iordache and Willam (1998) and Coelho and C. (2008)). An antisymmetric tensor is simply a special case, *i.e.* where $\sigma_{yx} = \sigma_{xy}$ and $h = 0$.

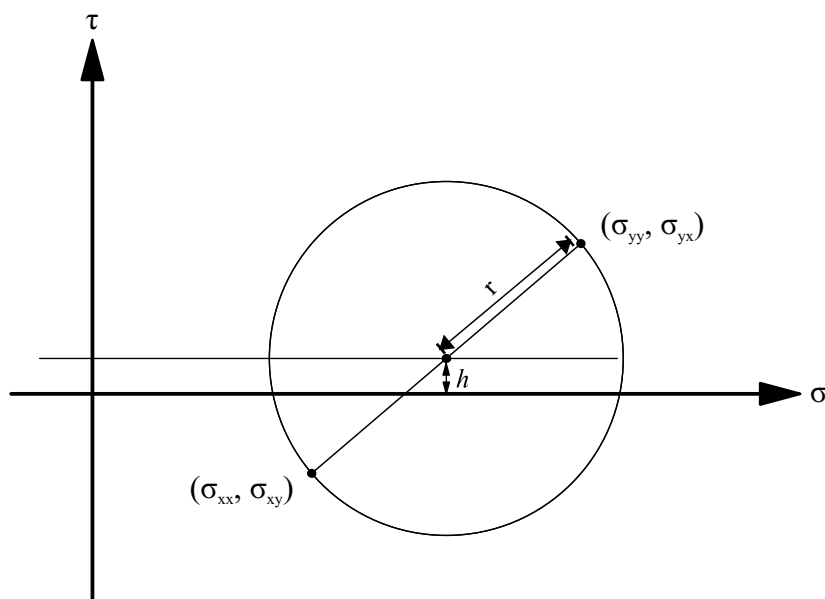


FIGURE 4.3: Mohr's circle for a plane strain tensor

Purely translational problems, such as the Coulomb wedge problem, represent an important subset of geotechnical problems, including strip footings. Therefore, purely translational analysis can be a valuable tool for a number of commonly occurring problems. Additionally, these purely translational mechanisms will always be upper bounds and can, therefore, be used to bound the true collapse load.

4.2.3 Stress functions

Stress functions are functions automatically satisfying the equilibrium equations. Stress functions were commonly used by engineers in the past to solve a variety of engineering problems. A well known example of a stress function is Airy's stress function given by equations (4.10), where Ω satisfies equations (4.11). Airy's stress function satisfies plane strain equilibrium, equations (4.1-4.3).

$$\sigma_{xx} = \frac{\partial^2 \phi}{\partial y^2} + \Omega; \quad \sigma_{yy} = \frac{\partial^2 \phi}{\partial x^2} + \Omega; \quad \sigma_{xy} = \sigma_{yx} = -\frac{\partial^2 \phi}{\partial x \partial y} \quad (4.10)$$

$$p_x = -\frac{\partial \Omega}{\partial x}; \quad p_y = -\frac{\partial \Omega}{\partial y} \quad (4.11)$$

In the following sections, stress functions automatically satisfying translational equilibrium will be used to derive the translational, equilibrium form of DLO. These stress functions will not necessarily satisfy rotational equilibrium, equation (4.3).

4.3 Derivation of DLO equilibrium formulation

In the following sections, the plane strain equilibrium DLO formulation will be derived. The derivation will be framed in terms of vector calculus and stress functions, allowing the use of the powerful theorems in Appendix D. Firstly, a set of stress functions satisfying translation equilibrium will be derived in Section 4.3.1. In Section 4.3.2, the integral forms of the translational equilibrium equations will be developed. In Sections 4.3.3 and 4.3.4, these integral forms will be used

to find the applied loads and internal forces on a path, leading to equation (2.37). (Note the term ‘path’ is used for consistency with vector calculus, but the term ‘discontinuity’ could equally be used.) These internal forces will then be used to enforce the Mohr-Coulomb yield condition on a path. Finally, the equilibrium formulation will be found by discretizing the problem domain and setting up a constrained optimization problem. In Section 4.3.7, the status of the equilibrium formulation in the context of the formal theorems of limit analysis will be discussed in light of this derivation.

4.3.1 Translational stress functions

In Section 4.3.2, the integral form of the translational equilibrium equations will be used to find the total body forces acting on a body, and the total change in the internal stresses across it. For this translational stress functions are required, satisfying equations (4.1) and (4.2).

Assuming that

$$p_x = \nabla \cdot \mathbf{P}^x, \quad (4.12)$$

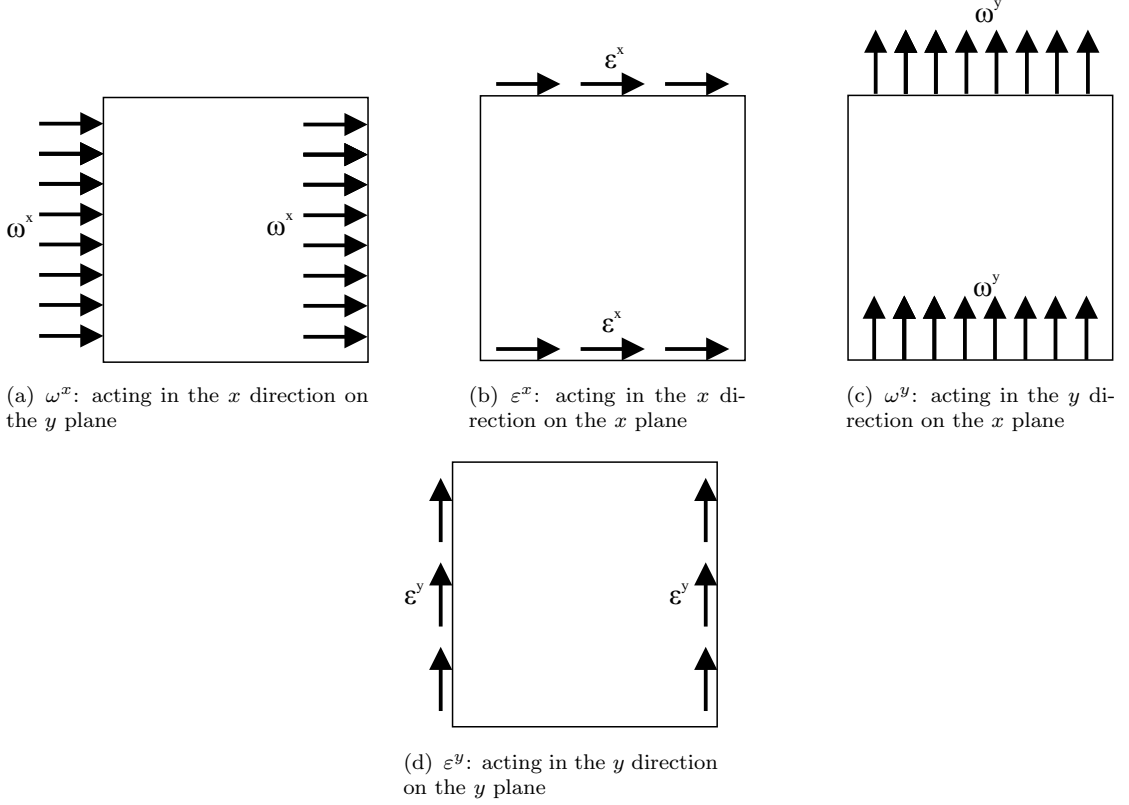
$$p_y = \nabla \cdot \mathbf{P}^y, \quad (4.13)$$

where

$$\mathbf{P}^x = \omega^x \mathbf{i} + \varepsilon^x \mathbf{j}, \quad (4.14)$$

$$\mathbf{P}^y = \varepsilon^y \mathbf{i} + \omega^y \mathbf{j}; \quad (4.15)$$

and where ω^x is a function describing the force per unit area acting in the x direction on the y plane; ε^x is a function describing the force per unit area acting in the x direction on the x plane; ω^y is a function describing the force per unit area acting in the y direction on the x plane; and ε^y is a function describing the force per unit area acting in the y direction on the y plane. ω^x , ε^x , ω^y and ε^y are illustrated in Figure 4.4.

FIGURE 4.4: Functions ω^x , ε^x , ω^y and ε^y describing body force per unit area

Equations (4.1) and (4.2) are satisfied by stress functions t^x and t^y , where

$$\sigma_{xx} = -\omega^x + \frac{\partial t^x}{\partial y}, \quad \sigma_{yx} = -\varepsilon^x - \frac{\partial t^x}{\partial x}, \quad (4.16a)$$

$$\sigma_{yy} = -\omega^y + \frac{\partial t^y}{\partial x}, \quad \sigma_{xy} = -\varepsilon^y - \frac{\partial t^y}{\partial y}. \quad (4.16b)$$

Now σ^x , σ^y and σ can be rewritten as

$$\sigma^x = \nabla \times \Phi^x - \mathbf{P}^x = \left(-\omega^x + \frac{\partial t^x}{\partial y}\right)\mathbf{i} + \left(-\varepsilon^x - \frac{\partial t^x}{\partial x}\right)\mathbf{j}, \quad (4.17)$$

$$\sigma^y = \nabla \times \Phi^y - \mathbf{P}^y = \left(-\varepsilon^y + \frac{\partial t^y}{\partial y}\right)\mathbf{i} + \left(-\omega^y - \frac{\partial t^y}{\partial x}\right)\mathbf{j}, \quad (4.18)$$

$$\boldsymbol{\sigma} = \begin{bmatrix} -\omega^x + \frac{\partial t^x}{\partial y} & -\varepsilon^x - \frac{\partial t^x}{\partial x} \\ -\varepsilon^y + \frac{\partial t^y}{\partial y} & -\omega^y - \frac{\partial t^y}{\partial x} \end{bmatrix}; \quad (4.19)$$

where $\boldsymbol{\sigma}$ is, generally, not symmetric and

$$\Phi^x = (0)\mathbf{i} + (0)\mathbf{j} + (t^x)\mathbf{k}, \quad (4.20)$$

$$\Phi^y = (0)\mathbf{i} + (0)\mathbf{j} + (t^y)\mathbf{k}. \quad (4.21)$$

4.3.2 Integral form

In the following section, the integral forms of equations (4.1) and (4.2), with stress functions t^x and t^y substituted in, will be found by considering a body G , shown in Figure 4.5(a). These integral forms will be used in Sections 4.3.3 and 4.3.4, to determine the external and internal forces on an arbitrary path.

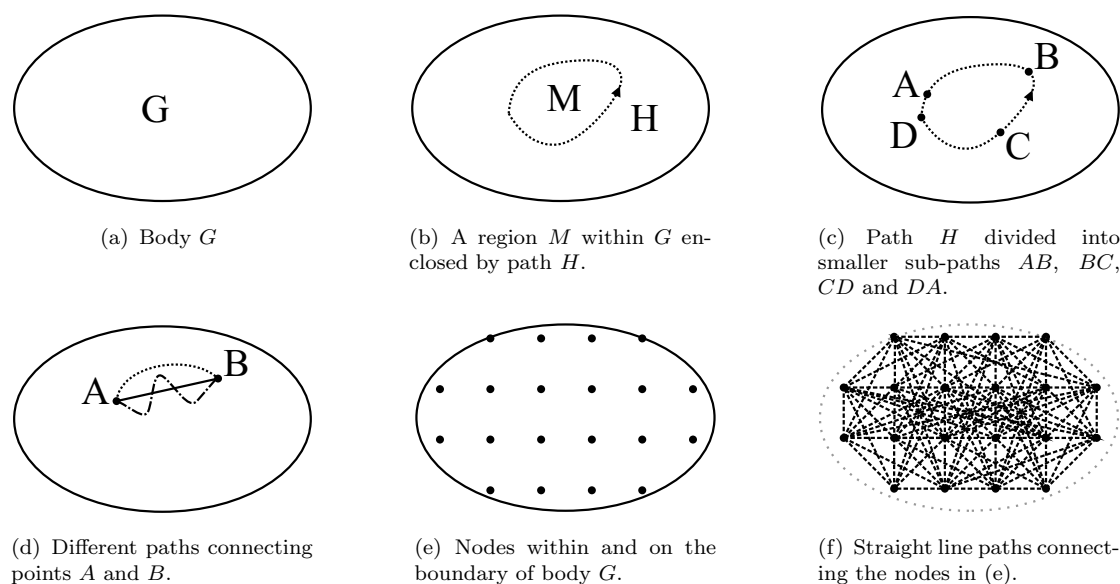


FIGURE 4.5: Nodes, paths and regions within a body G

For body G to be in translational equilibrium, any arbitrary region M (shown in Figure 4.5(b)), enclosed by a path H , must satisfy equations (4.1) and (4.2). Integrating equations (4.1) and (4.2) over M leads to equations (4.22) and (4.23)

being obtained, where the right hand sides equal the total body forces on M in the x and y directions respectively. The left hand sides of the equations equal the negative of the total change in the internal stress over M in the x and y directions respectively.

$$-\iint_M \nabla \cdot \boldsymbol{\sigma}^x \, dxdy = \iint_M \nabla \cdot \mathbf{P}^x \, dxdy \quad (4.22)$$

$$-\iint_M \nabla \cdot \boldsymbol{\sigma}^y \, dxdy = \iint_M \nabla \cdot \mathbf{P}^y \, dxdy \quad (4.23)$$

Equations (4.22) and (4.23) are necessary but not sufficient to ensure translational equilibrium. As t^x , t^y , $\nabla \cdot \mathbf{P}^x$ and $\nabla \cdot \mathbf{P}^y$ from Section 4.3.1 satisfy translational equilibrium, these must also satisfy equations (4.22) and (4.23).

Considering the left hand and right hand sides separately, the total body forces on M can be found using Stokes' theorem (note that anticlockwise closed paths are taken as positive throughout this chapter):

$$\iint_M \nabla \cdot \mathbf{P}^x \, dxdy = \oint_H \mathbf{P}^x \cdot d\mathbf{r} = - \oint_H \varepsilon^x \, dx + \oint_H w^x \, dy, \quad (4.24)$$

$$\iint_M \nabla \cdot \mathbf{P}^y \, dxdy = \oint_H \mathbf{P}^y \cdot d\mathbf{r} = - \oint_H w^y \, dx + \oint_H \varepsilon^y \, dy. \quad (4.25)$$

The total change in the internal forces on M in the x and y directions, respectively, can also be found using Stokes' theorem:

$$\begin{aligned} \iint_M \nabla \cdot \boldsymbol{\sigma}^x \, dxdy &= \oint_H \boldsymbol{\sigma}^x \cdot d\mathbf{r} & (4.26) \\ &= \oint_H \nabla \times \boldsymbol{\Phi}^x \cdot d\mathbf{r} - \oint_H \mathbf{P}^x \cdot d\mathbf{r} \\ &= - \oint_H \left(-\frac{\partial t^x}{\partial x}\right) dx + \oint_H \left(-\frac{\partial t^x}{\partial y}\right) dy - \oint_H \mathbf{P}^x \cdot d\mathbf{r} \\ &= \oint_H \nabla t^x \cdot d\mathbf{r} - \oint_H \mathbf{P}^x \cdot d\mathbf{r}, \end{aligned}$$

$$\begin{aligned}
\iint_M \nabla \cdot \boldsymbol{\sigma}^y \, dx dy &= \oint_H \boldsymbol{\sigma}^y \cdot d\mathbf{r} & (4.27) \\
&= \oint_H \nabla \times \boldsymbol{\Phi}^y \cdot d\mathbf{r} - \oint_H \mathbf{P}^y \cdot d\mathbf{r} \\
&= - \oint_H \left(-\frac{\partial t^y}{\partial x}\right) dx + \oint_H \left(-\frac{\partial t^y}{\partial y}\right) dy - \oint_H \mathbf{P}^x \cdot d\mathbf{r} \\
&= \oint_H \nabla t^y \cdot d\mathbf{r} - \oint_H \mathbf{P}^y \cdot d\mathbf{r},
\end{aligned}$$

This reveals that $\oint_H \nabla t^x \cdot d\mathbf{r} = 0$ and $\oint_H \nabla t^y \cdot d\mathbf{r} = 0$, as would be expected from vector calculus, and therefore that $\oint_H \nabla \times \boldsymbol{\Phi}^x \cdot d\mathbf{r} = 0$ and $\oint_H \nabla \times \boldsymbol{\Phi}^y \cdot d\mathbf{r} = 0$.

The line integral of a closed path can be found by dividing the path into a series of sub-paths. The line integral is now simply the sum of individual sub-path line integrals. For the example shown in Figure 4.5(c):

$$\oint_H \boldsymbol{\sigma}^x \cdot d\mathbf{r} = \int_A^D \boldsymbol{\sigma}^x \cdot d\mathbf{r} + \int_D^C \boldsymbol{\sigma}^x \cdot d\mathbf{r} + \int_C^B \boldsymbol{\sigma}^x \cdot d\mathbf{r} + \int_B^A \boldsymbol{\sigma}^x \cdot d\mathbf{r}, \quad (4.28)$$

$$\oint_H \boldsymbol{\sigma}^y \cdot d\mathbf{r} = \int_A^D \boldsymbol{\sigma}^y \cdot d\mathbf{r} + \int_D^C \boldsymbol{\sigma}^y \cdot d\mathbf{r} + \int_C^B \boldsymbol{\sigma}^y \cdot d\mathbf{r} + \int_B^A \boldsymbol{\sigma}^y \cdot d\mathbf{r}, \quad (4.29)$$

$$\oint_H \mathbf{P}^x \cdot d\mathbf{r} = \int_A^D \mathbf{P}^x \cdot d\mathbf{r} + \int_D^C \mathbf{P}^x \cdot d\mathbf{r} + \int_C^B \mathbf{P}^x \cdot d\mathbf{r} + \int_B^A \mathbf{P}^x \cdot d\mathbf{r}, \quad (4.30)$$

$$\oint_H \mathbf{P}^y \cdot d\mathbf{r} = \int_A^D \mathbf{P}^y \cdot d\mathbf{r} + \int_D^C \mathbf{P}^y \cdot d\mathbf{r} + \int_C^B \mathbf{P}^y \cdot d\mathbf{r} + \int_B^A \mathbf{P}^y \cdot d\mathbf{r}. \quad (4.31)$$

4.3.3 Applying loads

Discretely applied loads are present in many engineering problems. Therefore, a method capable of applying discrete loads other than distributed body forces is required. The integral forms developed in Section 4.3.2 allow discrete application of loads to a body via its boundaries (see Appendix E for further information).

Consider forces f^x and f^y applied discretely to a triangular body ABO via boundaries OA and BO , respectively, where BO and OA are parallel to the x and y axes, respectively, as shown in Figure 4.6(a). $\int_A^B \mathbf{P}^x \cdot d\mathbf{r}$, $\int_B^O \mathbf{P}^x d\mathbf{r}$ and $\int_O^A \mathbf{P}^x \cdot d\mathbf{r}$ can be interpreted as the loads on AB , BO and OA , respectively, in the x direction and $\int_A^B \mathbf{P}^y \cdot d\mathbf{r}$, $\int_B^O \mathbf{P}^y d\mathbf{r}$ and $\int_O^A \mathbf{P}^y \cdot d\mathbf{r}$ as the loads on AB , BO and OA respectively, in the y direction. Therefore, f^x and f^y can be applied perpendicular to boundaries AO and OC respectively, using, for example, the variations of ω^x , ε^x , ω^y and ε^y in Figures 4.6(b) and 4.6(c). Using the variations in Figures 4.6(b) and 4.6(c), $\omega^x = 0$, $\varepsilon^x = 0$, $\omega^y = 0$ and $\varepsilon^y = 0$ on AB , therefore,

$$\begin{aligned} \int_A^B \mathbf{P}^x \cdot d\mathbf{r} &= -\int_A^B \varepsilon^x dx + \int_A^B \omega^x dy \\ &= 0 \cdot \int_A^B 1 dx + 0 \cdot \int_A^B 1 dy = 0, \end{aligned} \quad (4.32)$$

$$\begin{aligned} \int_A^B \mathbf{P}^y \cdot d\mathbf{r} &= -\int_A^B \omega^y dx + \int_A^B \varepsilon^y dy \\ &= 0 \cdot \int_A^B 1 dx + 0 \cdot \int_A^B 1 dy = 0; \end{aligned} \quad (4.33)$$

$\omega^x = 0$, $\varepsilon^x = 0$, $\omega^y = \frac{f^y}{(x_B - x_O)}$ and $\varepsilon^y = 0$ on BO , therefore,

$$\begin{aligned} \int_B^O \mathbf{P}^x \cdot d\mathbf{r} &= -\int_B^O \varepsilon^x dx + \int_B^O \omega^x dy \\ &= 0 \cdot \int_B^O 1 dx + 0 \cdot \int_B^O 1 dy = 0, \end{aligned} \quad (4.34)$$

$$\begin{aligned} \int_B^O \mathbf{P}^y \cdot d\mathbf{r} &= -\int_B^O \omega^y dx + \int_B^O \varepsilon^y dy \\ &= -\frac{f^y}{(x_O - x_B)} \cdot \int_B^O 1 dx + 0 \cdot \int_B^O 1 dy \\ &= -\frac{f^y}{(x_B - x_O)} \cdot (x_O - x_B) = f^y, \end{aligned} \quad (4.35)$$

resulting in a load f^y applied across BO ; $\omega^x = 0$, $\varepsilon^x = -\frac{f^x}{(y_O - y_A)}$, $\omega^y = 0$ and $\varepsilon^y = 0$ on OA , therefore,

$$\begin{aligned} \int_O^A \mathbf{P}^x \cdot d\mathbf{r} &= -\int_O^A \varepsilon^x dx + \int_O^A \omega^x dy & (4.36) \\ &= 0 \cdot \int_O^A 1 dx - \frac{f^x}{(y_O - y_A)} \cdot \int_O^A 1 dy \\ &= -\frac{f^x}{(y_O - y_A)} \cdot (y_A - y_O) = f^x, \end{aligned}$$

$$\begin{aligned} \int_O^A \mathbf{P}^y \cdot d\mathbf{r} &= -\int_O^A \omega^y dx + \int_O^A \varepsilon^y dy \\ &= 0 \cdot \int_O^A 1 dx + 0 \cdot \int_O^A 1 dy = 0, & (4.37) \end{aligned}$$

resulting in a load f^x applied across OA .

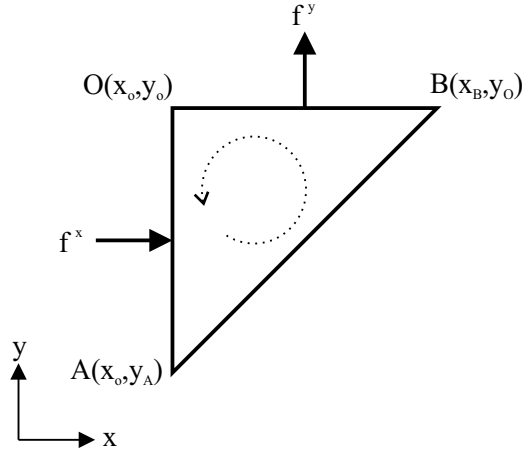
Using equations (4.24) and (4.25), the total applied loads f_{ABO}^x and f_{ABO}^y on ABO in the x and y directions, respectively, can be found.

$$f_{ABO}^x = \int_A^B \mathbf{P}^x \cdot d\mathbf{r} + \int_B^O \mathbf{P}^x \cdot d\mathbf{r} + \int_O^A \mathbf{P}^x \cdot d\mathbf{r} = f^x \quad (4.38)$$

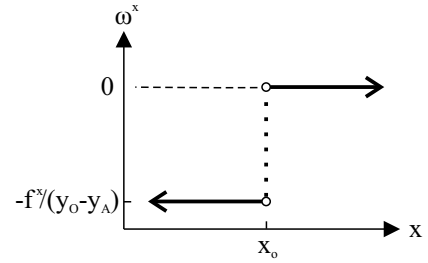
$$f_{ABO}^y = \int_A^B \mathbf{P}^y \cdot d\mathbf{r} + \int_B^O \mathbf{P}^y \cdot d\mathbf{r} + \int_O^A \mathbf{P}^y \cdot d\mathbf{r} = f^y \quad (4.39)$$

Similarly, f^x and f^y can be applied as tractions (shown in Figure 4.6(d)) to BO and OA , respectively, using, for example, the variations of ω^x , ε^x , ω^y and ε^y in Figures 4.6(e) and 4.6(f). This therefore confirms the definitions of ω^x , ε^x , ω^y and ε^y given in Figure 4.4.

Consider an arbitrary path i , inclined at an angle θ_i . Take, for example, path AB in Figure 4.7(a). Loads f_i^x and f_i^y in Figure 4.7(b) can be applied to a body ABC via path AB by line integrals $\int_A^B \mathbf{P}^x \cdot d\mathbf{r} = f_i^x$ and $\int_A^B \mathbf{P}^y \cdot d\mathbf{r} = f_i^y$. Assuming $\mathbf{P}^x = \mathbf{P}^y = 0$ at every point not located on AB , the total applied loads on ABC in the x and y directions must equal f_i^x and f_i^y , respectively. This can easily be demonstrated using equations (4.24) and (4.25).



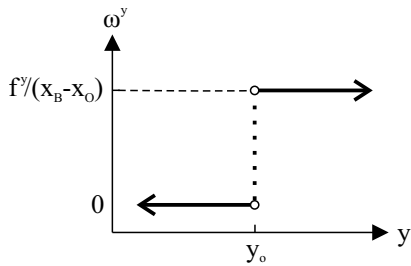
(a) f^x and f^y applied perpendicularly to OA and BO , respectively.



$$\omega^x(x) = \begin{cases} -f^y/(y_0 - y_A) & \text{for } x \leq x_0 \\ 0 & \text{for } x > x_0 \end{cases}$$

$$\varepsilon^x(x, y) = 0 \quad \text{for all } x, y$$

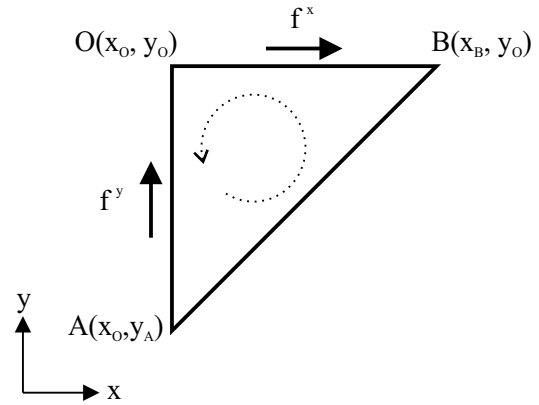
(b) ω^x and ε^x applying load f^x in (a).



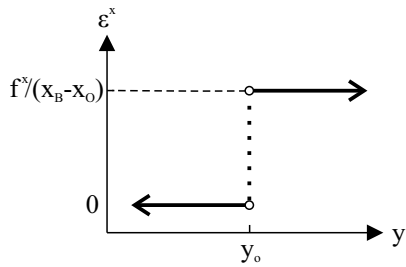
$$\omega^y(y) = \begin{cases} f^y/(x_B - x_0) & \text{for } y \geq y_0 \\ 0 & \text{for } y < y_0 \end{cases}$$

$$\varepsilon^y(x, y) = 0 \quad \text{for all } x, y$$

(c) ω^y and ε^y applying load f^y in (a).



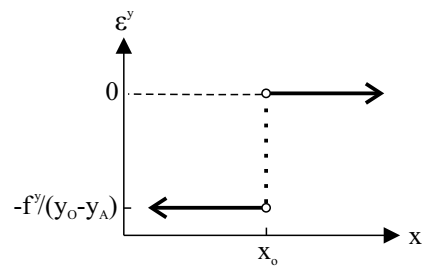
(d) f^x and f^y applied parallel to BO and OA , respectively.



$$\varepsilon^x(x) = \begin{cases} f^y/(x_B - x_0) & \text{for } y \geq y_0 \\ 0 & \text{for } y < y_0 \end{cases}$$

$$\omega^x(x, y) = 0 \quad \text{for all } x, y$$

(e) ω^x and ε^x applying load f^x in (b).

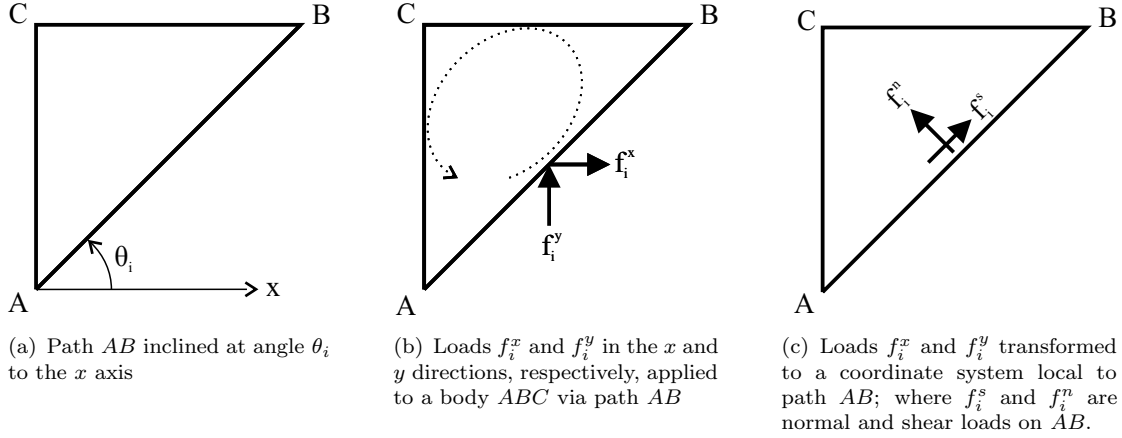


$$\varepsilon^y(x) = \begin{cases} -f^y/(y_0 - y_A) & \text{for } x \leq x_0 \\ 0 & \text{for } x > x_0 \end{cases}$$

$$\omega^y(x, y) = 0 \quad \text{for all } x, y$$

(f) ω^y and ε^y applying load f^y in (b).

FIGURE 4.6: Application of loads f^x and f^y to body ABO

FIGURE 4.7: Loads applied to an inclined path AB

As shown in Figure 4.7(c), loads f_i^x and f_i^y can be transformed to a coordinate system local to path i (in this case AB):

$$\begin{bmatrix} f_i^s \\ f_i^n \end{bmatrix} = \begin{bmatrix} \alpha_i & \beta_i \\ -\beta_i & \alpha_i \end{bmatrix} \begin{bmatrix} f_i^x \\ f_i^y \end{bmatrix} = \begin{bmatrix} \alpha_i & \beta_i \\ -\beta_i & \alpha_i \end{bmatrix} \begin{bmatrix} \int_A^B \mathbf{P}^x \cdot d\mathbf{r} \\ \int_A^B \mathbf{P}^y \cdot d\mathbf{r} \end{bmatrix}; \quad (4.40)$$

where $\alpha_i = \cos\theta_i$ and $\beta_i = \sin\theta_i$; f_i^s and f_i^n are normal and shear loads on i , respectively. f_i^n is positive in tension and f_i^s is positive when applied clockwise.

f_i^s and f_i^n can be split into dead and live load components

$$\begin{bmatrix} f_i^s \\ f_i^n \end{bmatrix} = \begin{bmatrix} f_{Di}^s \\ f_{Di}^n \end{bmatrix} + \lambda \begin{bmatrix} f_{Li}^s \\ f_{Li}^n \end{bmatrix} \quad (4.41)$$

where f_{Di}^s and f_{Li}^s are dead and live shear loads, respectively, on i ; f_{Di}^n and f_{Li}^n are dead and live normal loads, respectively, on i ; and λ is an adequacy factor on the live load. If path i is an internal boundary, f_i^s and f_i^n must be the sum of the total load applied between the path and an external boundary (see Appendix E.2 and E.4), excluding any load applied to the external boundary (see Appendix E.3). The direction of this summation is arbitrary, but must be consistent for all paths considered. This definition of f_i^s and f_i^n is consistent with that given in Section 2.6.2.4.

4.3.4 Internal forces on a path

In the following section, the forces on a path i due to the internal stresses will be determined. In Section 4.3.5, these internal forces will be used to enforce the Mohr-Coulomb yield condition.

Firstly, consider an arbitrary path i , inclined at an angle θ_i . Take, for example, path AB in Figure 4.8(a), bounding an infinitesimal element. Examining equations (4.26) and (4.27) and the gradient theorem (see Appendix D.1.3.1), it is clear that

$$F_i^x = \int_A^B \boldsymbol{\sigma}^x \cdot d\mathbf{r} = - \int_A^B \sigma_{yx} dx + \int_A^B \sigma_{xx} dy = t_B^x - t_A^x - \int_A^B \mathbf{P}^x \cdot d\mathbf{r} \quad (4.42)$$

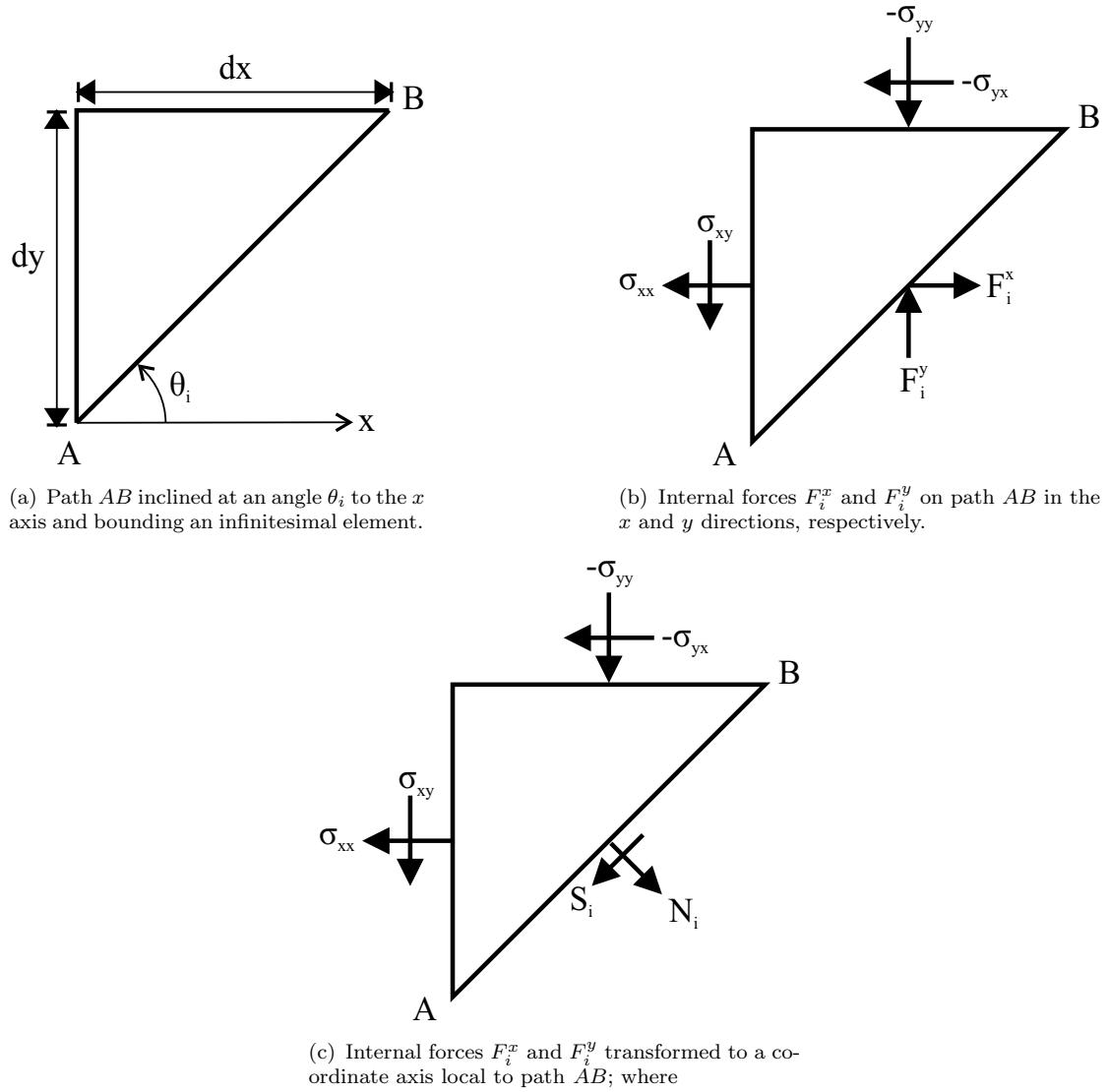
$$F_i^y = \int_A^B \boldsymbol{\sigma}^y \cdot d\mathbf{r} = - \int_A^B \sigma_{yy} dx + \int_A^B \sigma_{xy} dy = t_B^y - t_A^y - \int_A^B \mathbf{P}^y \cdot d\mathbf{r} \quad (4.43)$$

where F_i^x and F_i^y (see Figure 4.8(b)) are the forces in the x and y direction respectively, due to the internal stresses on AB ; t_A^x , t_A^y and t_B^x , t_B^y are the magnitudes of t^x and t^y at A and B , respectively. In the absence of body forces, line integrals F^x and F^y are path independent and remain unchanged for any path joining A and B ; for example, those shown in Figure 4.5(d).

Equations (4.42) and (4.43) can be transformed to the local coordinate system in Figure 4.8(c) as follows:

$$\begin{bmatrix} S_i \\ N_i \end{bmatrix} = \begin{bmatrix} \alpha_i & \beta_i & -\alpha_i & -\beta_i \\ -\beta_i & \alpha_i & \beta_i & -\alpha_i \end{bmatrix} \begin{bmatrix} t_A^x \\ t_A^y \\ t_B^x \\ t_B^y \end{bmatrix} + \begin{bmatrix} \alpha_i & \beta_i \\ -\beta_i & \alpha_i \end{bmatrix} \begin{bmatrix} \int_A^B \mathbf{P}^x \cdot d\mathbf{r} \\ \int_A^B \mathbf{P}^y \cdot d\mathbf{r} \end{bmatrix}; \quad (4.45)$$

where S_i and N_i are internal shear and normal forces on i , respectively. S_i is positive when clockwise and N_i is tensile positive. After rearranging and substituting in f_{Li}^s , f_{Li}^n , f_{Di}^s , f_{Di}^n and λ (see equations (4.40) and (4.41)), the following equation



$$\begin{bmatrix} S_i \\ N_i \end{bmatrix} = \begin{bmatrix} -\alpha_i & -\beta_i \\ \beta_i & -\alpha_i \end{bmatrix} \begin{bmatrix} F_i^x \\ F_i^y \end{bmatrix} \quad (4.44)$$

FIGURE 4.8: Internal forces on a path AB (where $\alpha_i = \cos \theta_i$ and $\beta_i = \sin \theta_i$)

is obtained:

$$\begin{bmatrix} \alpha_i & \beta_i & -\alpha_i & -\beta_i \\ -\beta_i & \alpha_i & \beta_i & -\alpha_i \end{bmatrix} \begin{bmatrix} t_A^x \\ t_A^y \\ t_B^x \\ t_B^y \end{bmatrix} + \lambda \begin{bmatrix} f_{Li}^s \\ f_{Li}^n \end{bmatrix} - \begin{bmatrix} S_i \\ N_i \end{bmatrix} = - \begin{bmatrix} f_{Di}^s \\ f_{Di}^n \end{bmatrix} \quad (4.46)$$

This is identical to equation (2.37).

4.3.5 Enforcing the Mohr-Coulomb yield condition on a path

Generally, direct methods require the yield function or flow rule to be enforced at least in a relaxed form. In this section, the internal forces obtained for an arbitrary path i will be used to enforce yield in a relaxed (averaged) sense.

In the uniform distribution of stresses in Figure 4.9, the normal σ_n and shear τ stresses must equal the average normal and shear stresses, respectively, along the whole length of i . Assuming failure occurs along i , the Mohr-Coulomb yield condition can be enforced for uniform distributions of σ_n and τ as follows:

$$\begin{bmatrix} 1 & \tan \phi_i \\ -1 & \tan \phi_i \end{bmatrix} \begin{bmatrix} S_i \\ N_i \end{bmatrix} \leq \begin{bmatrix} c_i l_i \\ c_i l_i \end{bmatrix}; \quad (4.47)$$

where l_i is the length of path i ; c_i is the cohesive strength on i ; and ϕ_i is angle of friction on i .

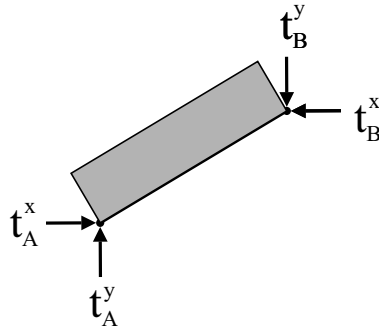


FIGURE 4.9: Uniform distribution of shear τ and normal stresses σ_n across a discontinuity i

4.3.6 Discretization

Assuming that the magnitude of t^x and t^y can only be determined at a specific number of locations, n , or at nodes within the domain (see Figure 4.5(e), for example). Suppose also that the nodes are connected by m number of straight line paths (see Figure 4.5(f), for example) and that f_{Li}^s , f_{Li}^n , f_{Di}^s and f_{Di}^n are known for all paths, $i = 1, 2, 3 \dots, m$. Applying equations (4.46) and (4.47) for all m paths as constraints, an optimization problem, determining the maximum adequacy factor λ , can be set up. In matrix form, this is the equilibrium form of DLO:

$$\max \lambda \quad (4.48)$$

subject to

$$\mathbf{B}^T \mathbf{t} + \lambda \mathbf{f}_L - \mathbf{q} = -\mathbf{f}_D \quad (4.49)$$

$$\mathbf{N}^T \mathbf{q} \leq \mathbf{g} \quad (4.50)$$

where $\mathbf{t} = \{t_1^x, t_1^y, t_2^x, t_2^y, \dots, t_n^y\}$; $\mathbf{q}^T = \{S_1, N_1, S_2, N_2, \dots, N_m\}$; $\mathbf{f}_L^T = \{f_{L1}^s, f_{L1}^n, f_{L2}^s, f_{L2}^n, \dots, f_{Lm}^n\}$; $\mathbf{f}_D^T = \{f_{D1}^s, f_{D1}^n, f_{D2}^s, f_{D2}^n, \dots, f_{Dm}^n\}$ and $\mathbf{g}^T = \{c_1 l_1, c_1 l_1, c_2 l_2, \dots, c_m l_m\}$. \mathbf{B} is a $2m \times 2n$ matrix containing direction cosines α_i and β_i . \mathbf{N} is a $2m \times 2m$ matrix enforcing equation (4.47) on all paths $i(i = 1, 2, \dots, m)$.

4.3.7 Discussion

The form of equilibrium formulation above is similar to that of lower bound formulation (see Section 2.2.4). However, duality theory clearly states that this equilibrium formulation must be an upper bound. The upper bound nature of the equilibrium formulation can be explained by the following insights obtained during the preceding derivations:

- (i) The stress functions used to derive the formulation do not enforce rotational equilibrium.

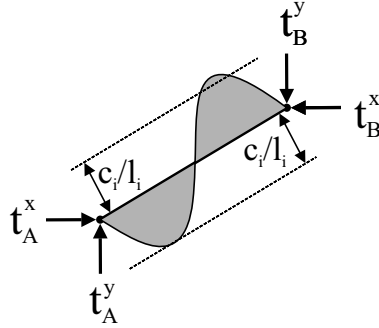


FIGURE 4.10: Distribution of shear stress τ exceeding the Tresca yield condition ($c_i > 0, \phi_i = 0$) locally on a discontinuity i , but satisfying equation (4.47) across its length l_i

- (ii) The yield condition is not enforced in the interior of the bodies bounded by paths i ($i = 1, 2, \dots, m$).
- (iii) As shown in Figure 4.3.7, the distribution of σ_n and τ across i will not necessarily be uniform. Furthermore, equation (4.47) may be satisfied, but yield may be exceeded locally. An equality in equation (4.47) can only occur when yield is exceeded at at least one point along path i . Therefore, equation (4.47) can be said to satisfy the upper bound theorem.
- (iv) A stress field is only generated within the domain populated by the nodes. The method does extend the stress field to ensure a statically admissible field outside this domain.

These insights clearly demonstrate the upper bound nature of the aforementioned equilibrium DLO formulation. However, it seems possible that a modified formulation capable of obtaining lower bound solutions could be developed.

4.4 Pseudo lower bounds

In Section 4.3.7, the upper bound nature of the DLO equilibrium formulation was examined, and the possibility of modifying the formulation so as to be able to

obtain lower bound solutions was raised. In the following section, relaxed lower bound methods, capable of obtaining ‘pseudo lower bounds’ on the true solution, will be developed for weightless Tresca materials using the stress functions t^x and t^y considered in Section 4.3.1. The methods described relax the lower bound theorem (see Section 2.2.4) as follows:

- (i) In a strict lower bound, the stress field must be statically admissible everywhere. This condition is relaxed so that the stress field is only required to be statically admissible over a defined domain. The stress field outside the domain need not be statically admissible and is ignored. Provided care is taken to define a sufficiently large domain, this relaxation should not significantly influence results. (Obviously, problems involving finite domains are clearly unaffected by this assumption.)
- (ii) Statical admissibility is relaxed. In particular, rotational equilibrium is no longer required, recalling that t^x and t^y only satisfy translational equilibrium. Therefore, these pseudo lower bounds can be used to bound the best solution attainable using upper bound translational limit analysis. Many important geotechnical problems involve translational mechanisms, and in such cases not enforcing rotational equilibrium is unlikely to significantly affect the results obtained (see Section 4.2.2).

Pseudo lower bounds can be obtained, for example, by dividing the domain into a mesh of triangular elements (for example, the mesh in Figure 4.11(a)). t^x and t^y are assumed to vary linearly across each triangular element. A linear variation of t^x and t^y across element j (shown Figure 4.11) is defined by

$$t^x = a_{j1}x + a_{j2}y + a_{j3}, \quad (4.51)$$

$$t^y = a_{j4}x + a_{j5}y + a_{j6}; \quad (4.52)$$

where a_{j1} - a_{j6} are scalar coefficients and can be obtained from standard shape function theory (e.g. Chakrabarty (2006)). Assuming no body forces or loads are applied to internal boundaries, the stress tensor σ_j on j can be found from

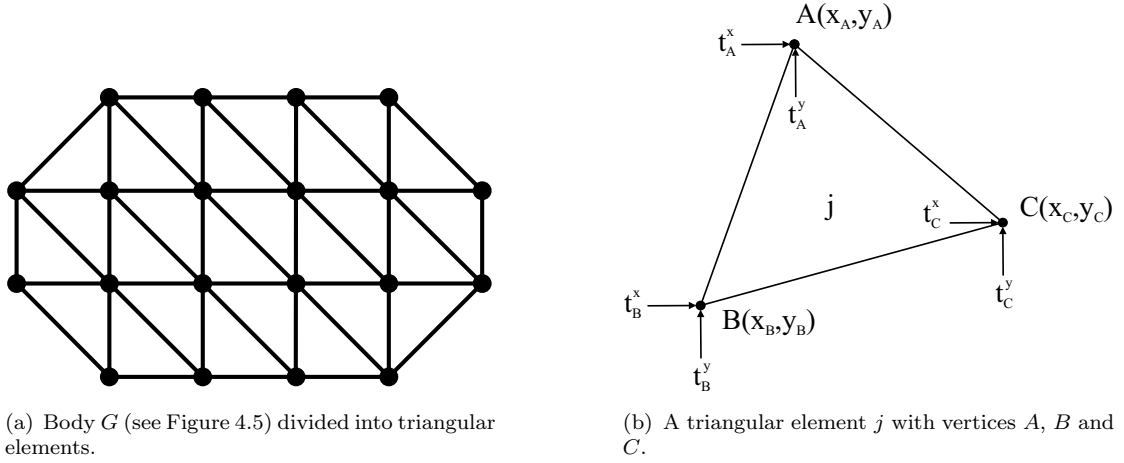


FIGURE 4.11: Pseudo lower bound mesh and element

equation (4.19) and must be constant as demonstrated by equation (4.53).

$$\boldsymbol{\sigma}_j = \begin{bmatrix} \frac{\partial t^x}{\partial y} & -\frac{\partial t^x}{\partial x} \\ \frac{\partial t^y}{\partial y} & -\frac{\partial t^y}{\partial x} \end{bmatrix} = \begin{bmatrix} a_{j2} & -a_{j1} \\ a_{j5} & -a_{j4} \end{bmatrix} \quad (4.53)$$

$\boldsymbol{\sigma}_j$ will, generally, not be antisymmetric and can be represented using a Mohr's circle displaced a distance $h_j = 0.5(a_{j1} + a_{j5})$ from the σ -axis (see Figure 4.3 and Equation 4.9). The maximum shear stress τ_j^{max} on j is, therefore,

$$\tau_j^{max} = r_j + |h_j| = \frac{1}{2} \sqrt{(a_{j2} + a_{j4})^2 + (a_{j5} - a_{j1})^2} + \frac{1}{2} |a_{j1} + a_{j5}|; \quad (4.54)$$

where r_j is the radius of the Mohr's circle. Assuming a weightless Tresca material, equation (4.54) allows the yield condition, $\tau_j^{max} \leq c_j$, to be checked, where c_j is the shear strength of the material on j .

If t^x and t^y at the vertices are known, this results in six simultaneous equations and six unknowns, allowing a_{j1} - a_{j6} to be determined from shape function theory.

$$\begin{bmatrix} t_A^x \\ t_A^y \\ t_B^x \\ t_B^y \\ t_C^x \\ t_C^y \end{bmatrix} = \begin{bmatrix} x_A & y_A & 1 & 0 & 0 & 0 \\ 0 & 0 & 0 & x_A & y_A & 1 \\ x_B & y_B & 1 & 0 & 0 & 0 \\ 0 & 0 & 0 & x_B & y_B & 1 \\ x_C & y_C & 1 & 0 & 0 & 0 \\ 0 & 0 & 0 & x_C & y_C & 1 \end{bmatrix} \begin{bmatrix} a_{j1} \\ a_{j2} \\ a_{j3} \\ a_{j4} \\ a_{j5} \\ a_{j6} \end{bmatrix} \quad (4.55a)$$

$$\mathbf{t}_j = \mathbf{P}_j \boldsymbol{\zeta}_j \quad (4.55b)$$

Equation (4.55) applies equations (4.51) and (4.52) at the vertices of element j , where \mathbf{P}_j , $\boldsymbol{\zeta}_j$ and \mathbf{t}_j are local vectors and matrices defined as indicated. In Sections 4.4.1 and 4.4.2, two pseudo lower bound methods, employing different methods of determining t^x and t^y at the vertices, will be developed.

4.4.1 Method I

The equilibrium (or ‘dual’) DLO formulation is defined in terms of t^x and t^y values at specified nodal points. Assuming a mesh of κ triangular elements, whose vertices coincide with nodal points in an equivalent upper bound DLO analysis, the t^x and t^y values from a DLO analysis can be used to obtain a_{j1} - a_{j6} for $j = 1, 2, \dots, \kappa$ (Smith, 2011b). For each element j ($j=1, 2, \dots, \kappa$), a factor

$$F_j = \frac{r_j + |h_j|}{c_j} \quad (4.56)$$

on yield can be obtained, where yield is violated for any $F_j > 1$. An overall factor

$$F = \max(\{F_1, F_2, \dots, F_\kappa\}) \quad (4.57)$$

can be obtained. Scaling all t^x and t^y values by F produces a new solution satisfying the yield condition everywhere and meeting the requirements for a pseudo lower

bound solution. The pseudo lower bound adequacy factor λ_l is simply $\lambda_l = \lambda / F$, where λ is the upper bound adequacy factor.

4.4.2 Method II

In method I, t^x and t^y are determined from an upper bound analysis. In method II, the t^x and t^y values at the element vertices are optimized directly to obtain the best possible lower bound solution for the given mesh employed. The optimized solution must satisfy equations (4.58-4.61) enforcing the Tresca yield condition and linear variation of t^x and t^y on each element j (see Figure 4.11).

$$\mathbf{0} = \mathbf{P}_j \boldsymbol{\zeta}_j - \mathbf{t}_j \quad (4.58)$$

$$\begin{bmatrix} 0 \\ 0 \\ 0 \\ 0 \end{bmatrix} = \begin{bmatrix} -0.5 & 0 & 0 & -0.5 & 0 & 0 \\ 0.5 & 0 & 0 & 0.5 & 0 & 0 \\ -1 & 0 & 0 & 1 & 0 & 0 \\ 0 & 1 & 0 & 0 & 1 & 0 \end{bmatrix} \begin{bmatrix} a_{j1} \\ a_{j2} \\ a_{j3} \\ a_{j4} \\ a_{j5} \\ a_{j6} \end{bmatrix} - \begin{bmatrix} h_{j1} \\ h_{j2} \\ f_{j1} \\ f_{j2} \end{bmatrix} \quad (4.59a)$$

$$= \mathbf{Q}_j \boldsymbol{\zeta}_j - \boldsymbol{\mu}_j \quad (4.59b)$$

$$c_j \geq \begin{bmatrix} 1 & 1 & 0 & 0 \end{bmatrix} \begin{bmatrix} h_{j1} \\ h_{j2} \\ f_{j1} \\ f_{j2} \end{bmatrix} + 0.5\vartheta_j \quad (4.60a)$$

$$\geq \mathbf{R}_j \boldsymbol{\mu}_j + 0.5\vartheta_j \quad (4.60b)$$

$$\vartheta_j \geq \sqrt{(f_{j1})^2 + (f_{j2})^2} \quad (4.61)$$

Equation (4.58) is simply a rearranged equation (4.55). Equations (4.59-4.61) apply the Tresca yield criteria using equation (4.54), where \mathbf{Q}_j , \mathbf{R}_j and $\boldsymbol{\mu}_j$ are local

vectors and matrices, defined within equations (4.59) and (4.60); also $h_{j1}, h_{j2} \geq 0$. ϑ_j is an upper bound on the diameter of the Mohr's circle. (Note the inequality in equation (4.61)). However, as the stress state on element j approaches yield, the optimizer will ensure ϑ_j approaches the diameter of the Mohr's circle. External boundary conditions and loads can also be applied as constraints using equations (4.46), where λ is replaced by λ_l to emphasize its pseudo lower bound nature.

Assuming a mesh comprising κ elements, equations (4.58-4.61) for all elements j ($j = 1, 2, \dots, \kappa$) are applied as constraints to an optimization problem, maximizing λ_l .

$$\max \lambda_l \quad (4.62)$$

subject to

$$\mathbf{B}_b \mathbf{t} + \lambda_l \mathbf{f}_{Lb} - \mathbf{q}_b = -\mathbf{f}_{Db} \quad (4.63)$$

$$\mathbf{N}_b \mathbf{q}_b \leq \mathbf{g}_b \quad (4.64)$$

$$\mathbf{P} \boldsymbol{\zeta} - \mathbf{t} = \mathbf{0} \quad (4.65)$$

$$\mathbf{Q} \boldsymbol{\zeta} - \boldsymbol{\mu} = \mathbf{0} \quad (4.66)$$

$$\mathbf{c} \geq \mathbf{R} \boldsymbol{\mu} + 0.5 \boldsymbol{\vartheta} \quad (4.67)$$

$$\vartheta_j \geq \sqrt{(f_{j1})^2 + (f_{j2})^2} \quad \forall j \in \{1, \dots, \kappa\} \quad (4.68)$$

$$\mathbf{h} \geq \mathbf{0} \quad (4.69)$$

where \mathbf{B}_b , \mathbf{f}_{Lb} , \mathbf{q}_b , \mathbf{f}_{Db} , \mathbf{N}_b and \mathbf{g}_b are the same as \mathbf{B} , \mathbf{f}_L , \mathbf{q} , \mathbf{f}_D , \mathbf{N} and \mathbf{g} , respectively (see equations (4.48-4.50)), but are only applied to the external boundaries. \mathbf{P} is a $6\kappa \times 6\kappa$ global matrix enforcing linear variation of t^x and t^y across elements $j = 1, 2, \dots, \kappa$. \mathbf{Q} is a $4\kappa \times 6\kappa$ global matrix containing the local \mathbf{Q}_j for all elements j ($j = 1, 2, \dots, \kappa$). \mathbf{R} is a $\kappa \times 4\kappa$ global matrix containing the local \mathbf{R}_j for all elements j ($j = 1, 2, \dots, \kappa$). $\boldsymbol{\zeta}^T = \{a_{11}, a_{12}, a_{13}, a_{14}, a_{15}, a_{16}, a_{21}, \dots, a_{\kappa 6}\}$, $\boldsymbol{\mu}^T = \{h_{11}, h_{12}, f_{11}, f_{12}, h_{21}, \dots, f_{\kappa 2}\}$, $\boldsymbol{\vartheta}^T = \{\vartheta_1, \vartheta_2, \dots, \vartheta_\kappa\}$ and $\mathbf{h}^T = \{h_{11}, h_{12}, h_{21}, \dots, h_{\kappa 2}\}$. Examining equations (4.62-4.69) reveals that the optimization problem can be solved using second order cone programming (SOCP). (Note plane strain

DLO results in a linear programming problem when applied to Mohr-Coulomb and Tresca materials.)

Comparison of this formulation with a conventional finite element limit analysis (FELA) formulation (see for example: Lysmer (1970); Lyamin and Sloan (2002a); Makrodimopoulos and Martin (2006)) reveals many similarities. However, unlike a FELA formulation, the problem is formulated in terms of stress functions automatically satisfying translational equilibrium. As a consequence, it is not necessary to explicitly enforce translational equilibrium as in FELA. However, additional constraints are needed to determine the components of the stress tensors on each element. Additional constraints are also necessary to determine \mathbf{h} as in a standard FELA formulation both rotational and translational equilibrium is generally enforced.

4.5 Numerical examples

The performance of the pseudo lower bound methods was evaluated by considering two examples. All computations were performed using a 3.0GHz Intel Dual Core E8400 processor with 3.5GB RAM and running Windows XP. Both pseudo lower bound methods were implemented using MATLAB 7.12. t^x and t^y for use with method I were obtained from a customized version of LimitState:GEO v. 3.0 Beta, a commercial DLO software application (LimitState, 2012). For method II, MOSEK v. 6.0, an interior point algorithm with SOCP capability, was used (Mosek, 2011).

For each example, LimitState:GEO was used to identify upper bound failure mechanisms for uniform rectangular nodal grids of increasing nodal density. LimitState:GEO identifies the rigid polygonal solids forming each failure mechanism. To allow the forces along the sides of the solids forming the mechanism to be established additional ‘crossover nodes’, not present in the original rectangular nodal grid, are frequently created in LimitState:GEO. In each case, the original rectangular nodal grid will be referred to as the ‘original grid’. Additionally, ‘kinks’ can

occur due to the use of a finite cutoff to filter out inactive discontinuities. (Note the solid identification procedure is primarily intended for visualization purposes and is approximate in nature.) A ‘kink’ is defined as a nodal point where a boundary separating two solids changes direction, but the nodal point is not a vertex of a third solid.

Making use of the solids forming the mechanism and the constrained Delaunay triangulation function in MATLAB, four different meshes were generated for each ‘original grid’ (see *e.g.* Figures 4.12 and 4.15).

- (i) Mesh A – is formed using the vertices of the solids forming the mechanism as the vertices of the elements. The remaining nodal points and corresponding t^x and t^y values are discarded. Individual elements are not allowed to cross the boundaries of solids.
- (ii) Mesh B – is similar to mesh A except ‘kinks’ in the solid boundaries are removed. The vertices of the solids forming the mechanism, excluding any ‘kinks’, are used as the vertices of the elements. The remaining nodal points are discarded as are the corresponding t^x and t^y values. Individual finite elements are not allowed to cross the boundaries of solids (with ‘kinks’ removed).
- (iii) Mesh C – is formed using the ‘original grid’ plus any additional ‘crossover nodes’ as the vertices of the finite elements. Individual finite elements are not allowed to cross the boundaries of solids.
- (iv) Mesh D – is formed using the ‘original grid’ as the vertices of the elements. ‘Crossover nodes’ and corresponding t^x and t^y values are discarded. Individual elements are free to cross the boundaries of solids.

For each example, method I was applied using meshes A-C and method II was applied using meshes A-D. A weightless Tresca material with a shear strength c was used in both examples and in each case the upper bounds for the corresponding LimitState:GEO grid are reported.

Note that to maintain consistency with the conventions adopted in LimitState:GEO, compressive normal stresses and anticlockwise shear stresses are taken as positive throughout.

4.5.1 Compression of a block

In the following section, the unconfined compression of a rectangular block between two perfectly rough rigid platens is considered. A block with height h and width $w = 2h$ is considered. Taking advantage of symmetry, only the upper left hand corner needs to be considered. The exact solution to this problem is $q/c = 2.42768$ (Saleçon, 1967; Chakrabarty, 2006), where q is the average pressure on the platens. In Figure 4.12, a representative ‘original grid’ and the meshes described in the preceding section are presented.

Pseudo lower bounds using method I have been computed for a number of ‘original grids’ and are presented in Table 4.1. The distributions of yield violations, prior to scaling by F , are presented in Figure 4.13 for the representative meshes shown in Figure 4.12.

Pseudo lower bounds using method II have also been computed and are presented in Table 4.2. The proximity to yield on individual elements is presented in Figure 4.14.

4.5.2 Prandtl problem

In the following section, the well known Prandtl problem is considered. A problem domain with height h and width $w = 7h/4$ is used. A perfectly rough indenter of width $2h$ is used throughout, unless otherwise stated. Taking advantage of symmetry about the centreline of the indenter, only the right hand side of the domain needs to be considered. The exact bearing capacity factor N_c for both rough and smooth indentors is $N_c = \pi + 2$.

TABLE 4.1: Compression of a plate – pseudo lower bound method I

nodes*	upper bound [‡]		pseudo lower bound					
	no.	q/c	$e(\%)$	mesh A		mesh B		mesh C
q/c				$e(\%)$	q/c	$e(\%)$	q/c	$e(\%)$
66	2.442	0.598	1.878	22.6	1.059	56.4	0.5646	76.7
231	2.434	0.256	1.880	22.6	2.271	6.44	0.3323	86.3
496	2.432	0.157	2.115	12.9	2.364	2.64	0.4616	81.0
861	2.430	0.104	2.125	12.5	2.334	3.85	0.1120	95.4
1,326	2.430	0.0791	2.060	15.1	2.381	1.91	0.07700	96.8
1,830	2.429	0.0626	1.472	39.4	2.361	2.75	0.3114	87.2
2,556	2.429	0.0544	1.810	25.4	1.832	24.5	0.1646	93.2

Key: * in ‘original grid’ ; [‡] from LimitState:GEO; e percentage error.

The solution to the Prandtl problem involves a fan shaped mechanism overlying a stationary region. In Figure 4.15, a representative ‘original grid’ and corresponding meshes A-D are presented. Meshes A and B are identical for all the ‘original grids’ considered, since no ‘kinks’ were present in the upper bound failure mechanisms. Additionally, meshes \tilde{A} , \tilde{B} and \tilde{C} were considered; where \tilde{A} , \tilde{B} and \tilde{C} are identical to meshes A, B and C respectively, but discard the stationary region and consider the mechanism only.

Pseudo lower bounds using method I have been computed for a number of ‘original grids’ and are presented in Table 4.3. The distributions of yield violations, prior to scaling by F, are presented in Figure 4.16 for the representative meshes in Figure 4.15.

Pseudo lower bounds using method II have also been computed and are presented in Table 4.4. The proximity to yield on individual elements, in the representative meshes in Figure 4.15, is presented graphically in Figure 4.17.

Figure 4.18 presents some selected results using mesh \tilde{A} for an ‘original grid’ with 1,075 nodes. These selected results illustrate the difference between method I solutions for the smooth and rough indenter but also the difference between the

solutions for methods I and II, respectively. (In Figure 4.18, the furthest right of the Mohr's circles correspond to the furthest left of the elements and vice versa.)

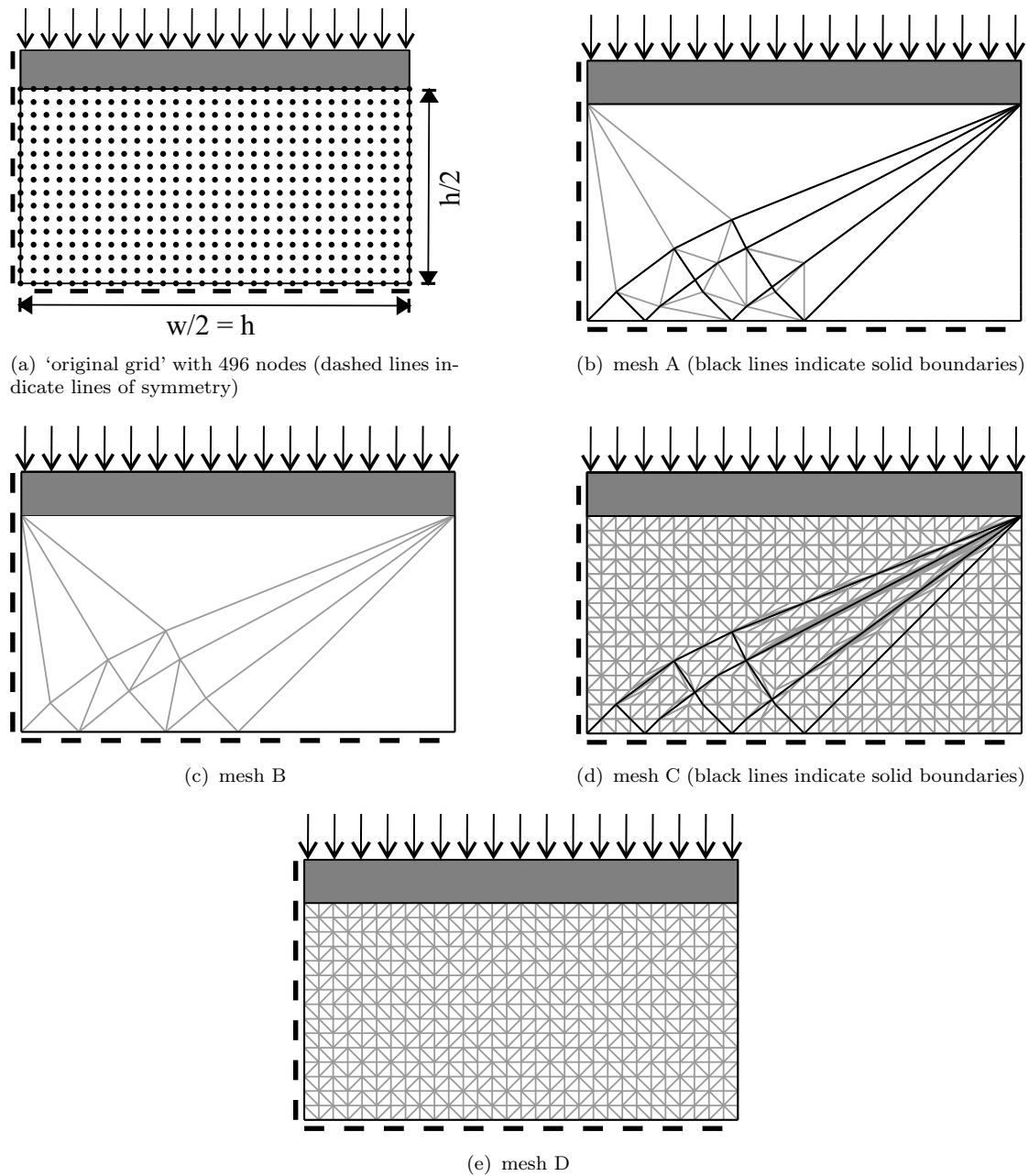


FIGURE 4.12: Compression of a block – 'original grid' and corresponding meshes

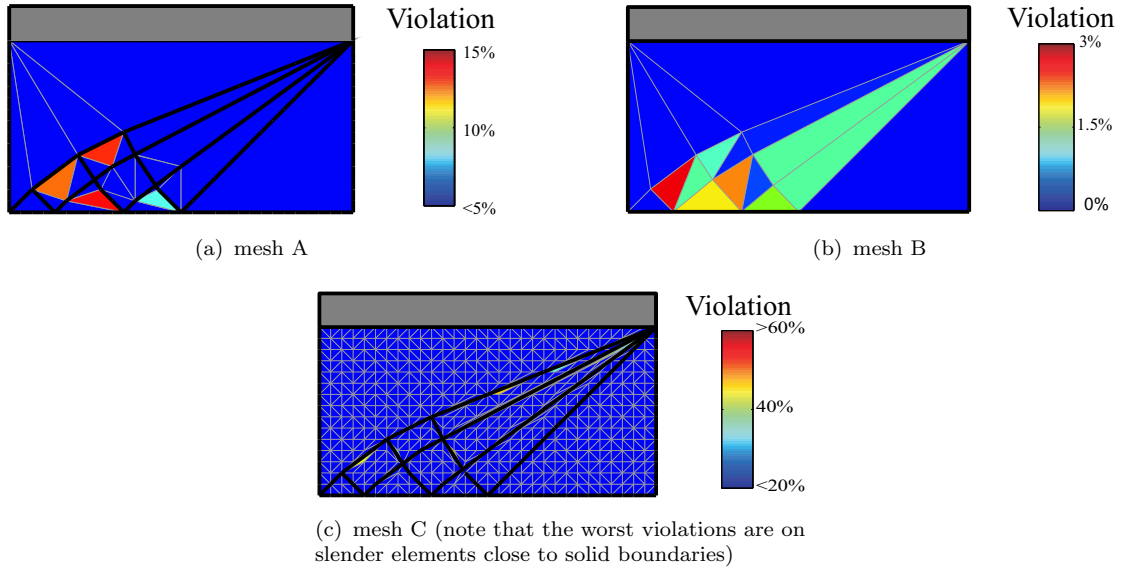


FIGURE 4.13: Compression of a block – distribution of yield violation, prior to scaling, using method I for the representative meshes shown in Figure 4.12

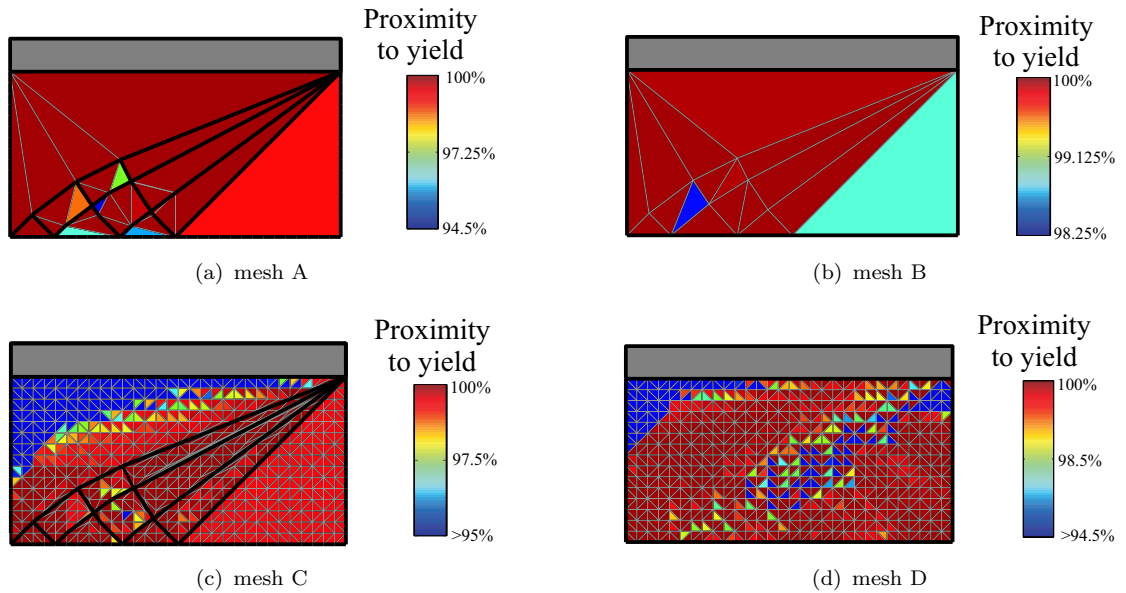


FIGURE 4.14: Compression of a block – proximity to yield on individual elements using method II for the representative meshes shown in Figure 4.12

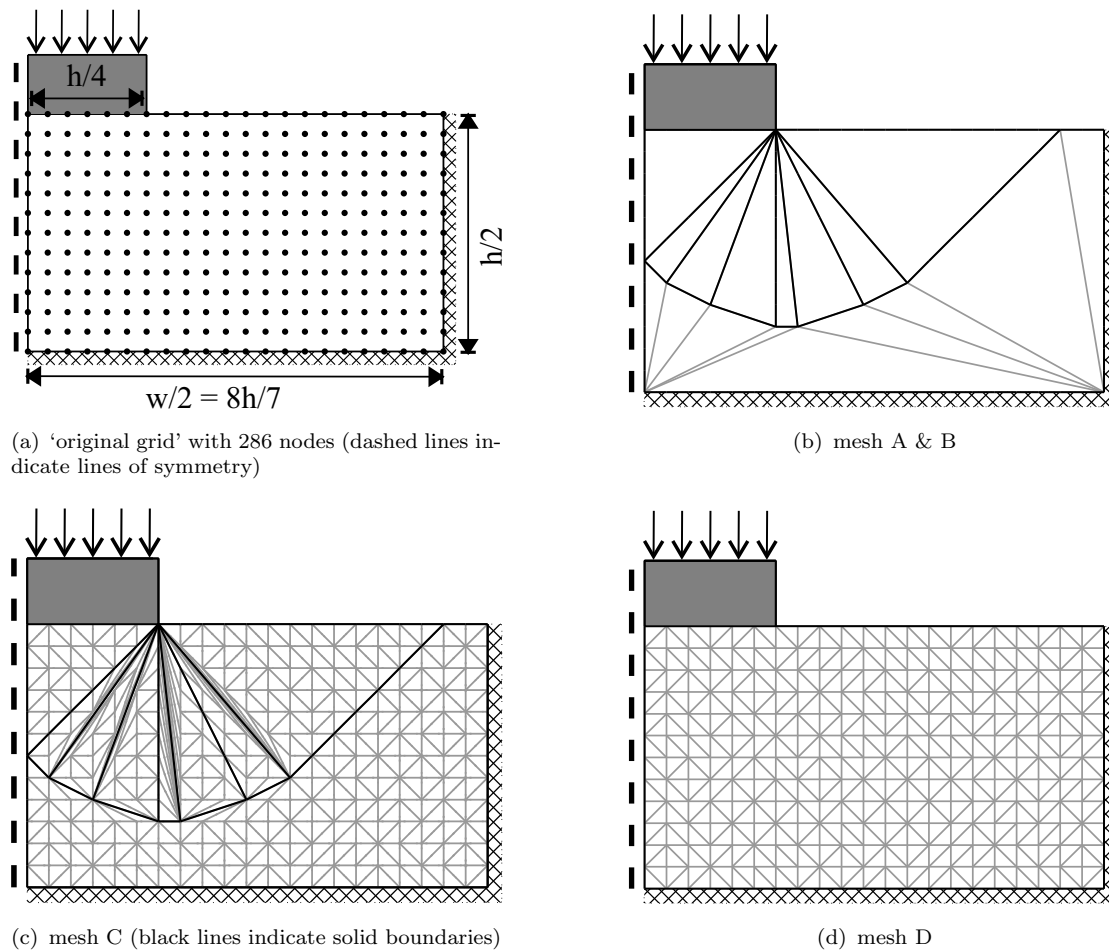


FIGURE 4.15: Prandtl punch – 'original grid' and corresponding meshes

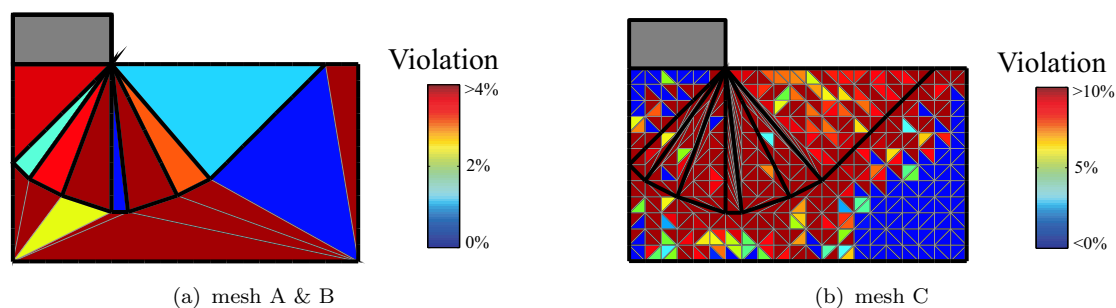


FIGURE 4.16: Prandtl punch – distribution of yield violation, prior to scaling, using method I for the representative meshes shown in Figure 4.15

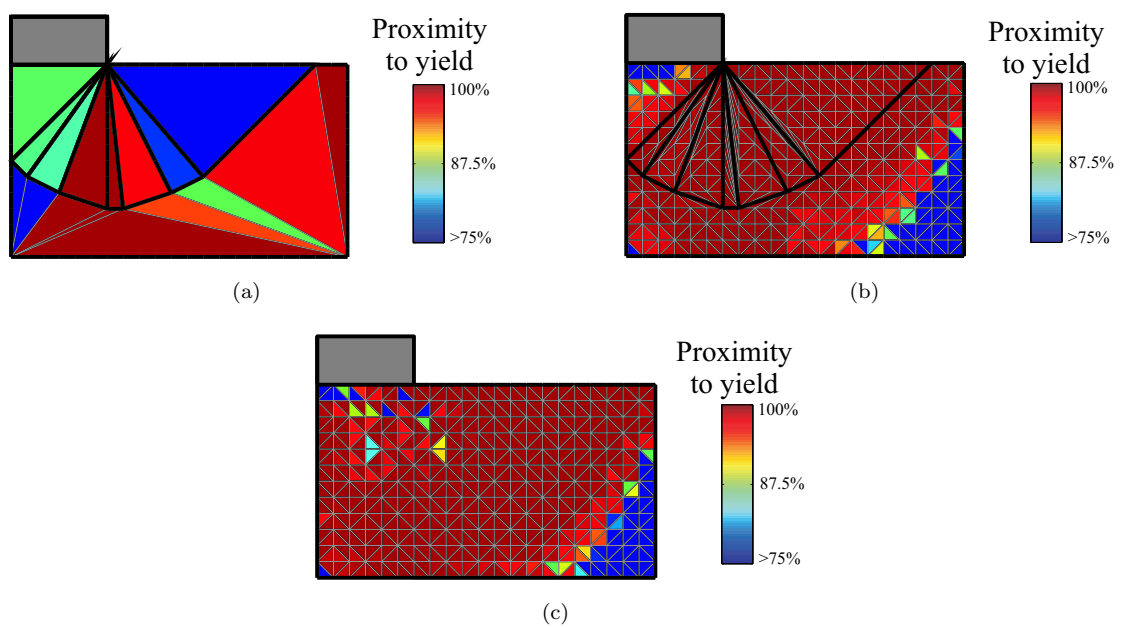


FIGURE 4.17: Prandtl punch – proximity to yield on individual elements using method II for the representative meshes shown in Figure 4.15

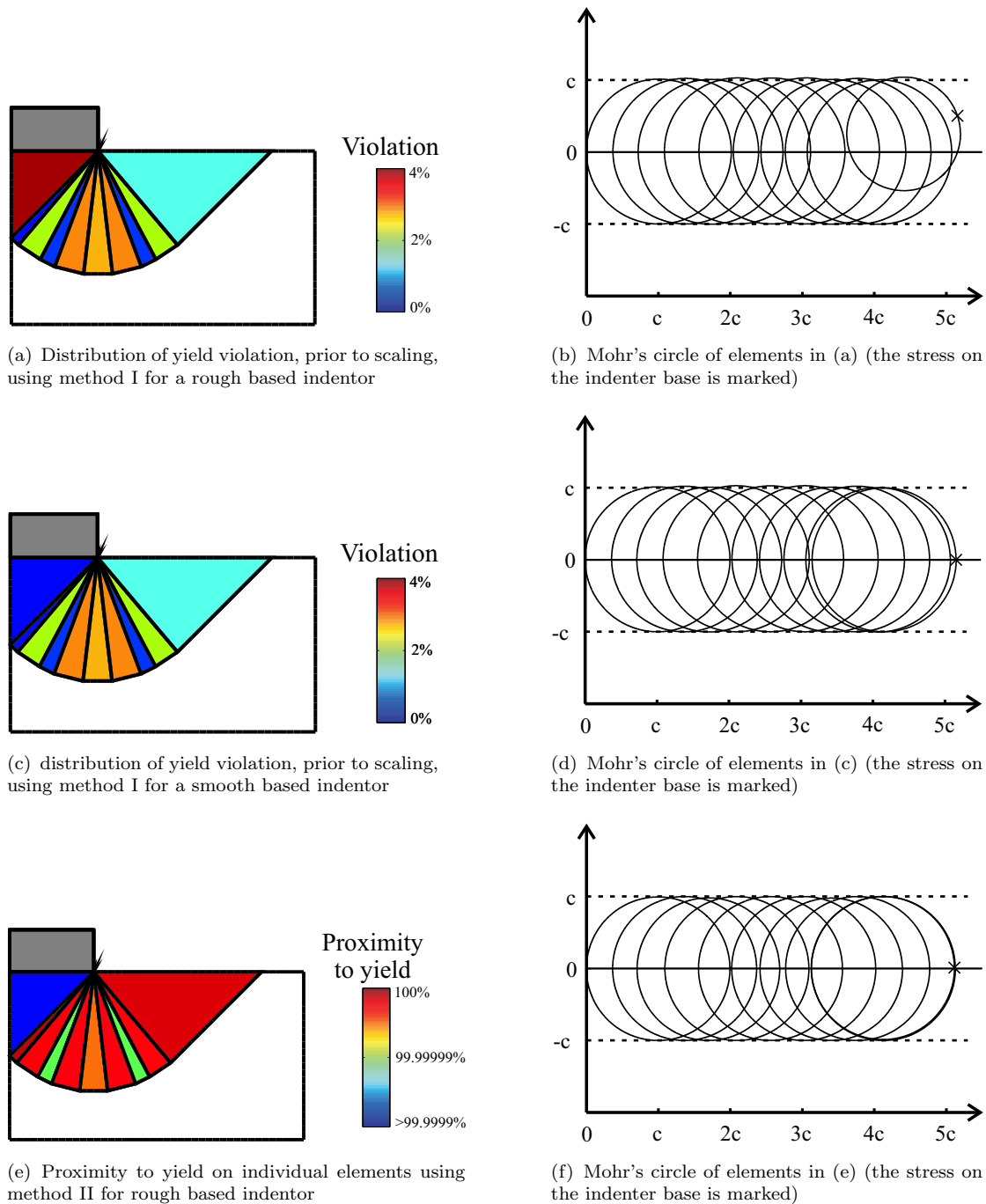


FIGURE 4.18: Selected results for Prandtl punch – mesh \tilde{A} for 'original grid' comprising 1,075 nodes

TABLE 4.2: Compression of a plate – pseudo lower bound method II

nodes*	upper bound [‡]		pseudo lower bound							
	q/c	e (%)	mesh A		mesh B		mesh C		mesh D	
no.	q/c	e (%)	q/c	e (%)	q/c	e (%)	q/c	e (%)	q/c	e (%)
66	2.442	0.598	2.405	0.952	2.321	4.39	2.405	0.950	2.326	4.18
231	2.434	0.256	2.393	1.45	2.399 [†]	1.20 [†]	2.412 [†]	0.661 [†]	2.314	4.67
496	2.432	0.157	2.415	0.525	2.419 [†]	0.367 [†]	2.417 [†]	0.421 [†]	2.349 [†]	3.25 [†]
864	2.430	0.104 [†]	2.407	0.854	2.407 [†]	0.859 [†]	2.414 [†]	0.567 [†]	2.385 [†]	1.77 [†]
1,326	2.430	0.0791	2.420 [†]	0.330 [†]	2.422	0.253 [†]	2.422 [†]	0.247 [†]	2.388 [†]	1.63 [†]
1,830	2.429	0.0626	2.416	0.469	2.421	0.272	2.419 [†]	0.347 [†]	2.396 [†]	1.31 [†]
2,556	2.429	0.0544	2.411 [†]	0.685 [†]	2.411 [†]	0.699 [†]	2.417 [†]	0.439 [†]	2.398	1.21

Key: * in 'original grid'; [‡] from LimitState:GEO; e percentage error; [†] MOSEK reported a near optimal solution.

TABLE 4.3: Prandtl punch – pseudo lower bound method I

Nodes*	Upper bound [†]		Pseudo lower bound							
	N_c	e (%)	mesh A & B		mesh \tilde{A} & \tilde{B}		mesh \tilde{A} & \tilde{B} (smooth indenter)		mesh C & \tilde{C}	
No.	N_c	e (%)	N_c	e (%)	N_c	e (%)	N_c	e (%)	N_c	e (%)
286	5.191	0.955	1.248	75.7	4.864	5.40	4.864	5.40	1.116	78.3
493	5.170	0.554	1.468	71.5	4.849	5.68	4.849	5.68	1.327	74.2
756	5.164	0.426	1.425	72.3	4.951	3.70	4.951	3.70	0.8160	84.2
1,075	5.154	0.243	1.407	72.6	4.949	3.75	5.006	2.63	0.7787	84.9
1,450	5.157	0.290	1.393	72.9	4.940	3.92	5.027	2.23	0.7134	86.1
1,881	5.152	0.204	1.383	73.1	4.934	4.04	5.026	2.25	0.8671	83.1
2,368	5.152	0.197	1.373	73.3	4.916	4.39	5.053	1.73	0.2937	94.3
2,911	5.149	0.152	1.436	72.1	4.920	4.32	5.034	2.10	0.5544	89.2
3,510	5.150	0.164	1.248	75.7	4.911	4.49	5.031	2.15	0.4256	91.7

Key: * in 'original grid'; [†] from LimitState:GEO (both smooth and rough indenter); e percentage error;

[†] MOSEK reported a near optimal solution; all results for a rough indenter, unless otherwise indicated.

TABLE 4.4: Prandtl punch – pseudo lower bound method II

Nodes*	Upper bound [‡]		Pseudo lower bound									
	N_c	e (%)	Mesh A & B N_c	e (%)	Mesh \tilde{A} & \tilde{B} N_c	e (%)	Mesh C N_c	e (%)	Mesh \tilde{C} N_c	e (%)	Mesh D N_c	e (%)
286	5.191	0.955	3.585	30.3	5.082	1.16	5.079 [†]	1.21 [†]	5.082	1.16	4.785 [†]	6.94 [†]
493	5.170	0.554	3.585	30.3	5.099	0.829	5.103 [†]	0.742 [†]	5.108	0.656	4.814	6.36
756	5.164	0.426	3.585	30.3	5.103	0.754	5.095 [†]	0.905 [†]	5.103	0.742	4.984 [†]	3.06 [†]
1,075	5.154	0.243	3.585	30.3	5.112	0.575	5.104 [†]	0.730 [†]	5.112 [†]	0.584 [†]	4.927 [†]	4.17 [†]
1,450	5.157	0.290	3.585	30.3	5.119	0.436	5.112 [†]	0.583 [†]	5.120 [†]	0.414 [†]	4.957 [†]	3.59 [†]
1,881	5.152	0.204	3.585	30.3	5.121	0.405	5.118 [†]	0.464 [†]	5.120 [†]	0.413 [†]	4.968 [†]	3.38 [†]
2,368	5.152	0.197	3.585	30.3	5.120	0.417	5.109 [†]	0.627 [†]	5.115 [†]	0.526 [†]	4.983 [†]	3.09 [†]
2,911	5.149	0.152	3.585	30.3	5.124	0.352	5.115 [†]	0.512 [†]	5.121 [†]	0.396 [†]	5.013 [†]	2.51 [†]
3,510	5.150	0.164	3.585	30.3	5.120	0.430	5.103 [†]	0.750 [†]	5.114 [†]	0.532 [†]	5.003 [†]	2.70 [†]

Key: * in 'original grid'; [‡] from LimitState:GEO; e percentage error; [†] Mosek reported a near optimal solution; all results for a rough indenter.

4.5.3 Discussion

4.5.3.1 Method I

Examining Tables 4.1 and 4.3, it is obvious that method I compares poorly with equivalent upper bounds (errors are at least an order of magnitude greater). This discrepancy can be ascribed to factors, both stemming from nodal t^x and t^y values being obtained from upper bound analyses.

- (i) Take for example, the simple mechanism in Figure 4.19(a), resulting in an upper bound $N_c = 6.000$ (error 16.7%). Yield must occur on the active discontinuities (*i.e.* $\tau_1 = 0$, $\tau_2 = c$, $\tau_3 = c$, $\tau_4 = c$, $\tau_5 = 0$ and $\sigma_5 = 0$). $\sigma_1 = 6c$, $\sigma_2 = 4c$, $\sigma_3 = 3c$ and $\sigma_4 = 2c$ are determined from translational equilibrium. Assuming constant stress states on each block, the stress state on each is fully determined (see Figure 4.19(b)). By scaling the stress state, a pseudo lower bound $N_c = 2.883$ (error 43.9%, *i.e.* 2-3 that in the upper bound) is obtained. As the stress state is fully determined, an improved method I solution is not possible for this mesh. Scaling reduces the stresses so that yield is no longer violated but the relative magnitude of the stresses remains unchanged.
- (ii) The optimizer has little freedom in selecting t^x and t^y values at the intersections between active discontinuities but still has considerable freedom elsewhere. Consider the compression of a square block between two perfectly rough platens. In Figure 4.20(a), a simple mechanism is shown, resulting in the ‘exact’ solution $q/c = 2$. For the mechanism to develop, $\tau_2 = 0$, $\tau_3 = c$, $\tau_4 = 0$, $\tau_5 = 0$ and $\sigma_5 = 0$. $\sigma_2 = \sigma_4 = 2c$, $\sigma_3 = c$ and $\sigma_1 = 2c$ can be determined from translational equilibrium. However, τ_1 and σ_2 cannot be uniquely determined. Assuming constant stress states on each block, the stress state on the lower block is fully determined but not the stress state on the upper block. Figures 4.20(b) and 4.20(c) show two valid stress states, satisfying translational equilibrium, resulting in pseudo lower bounds $q/c = 2$ (error 0%) and $q/c = 1.913$ (error 4.35%), respectively. An upper bound analysis

is free to select t^x and t^y values resulting in either stress state. Therefore, upper bound analysis does not necessarily result in the best possible method I pseudo lower bound for a mesh.

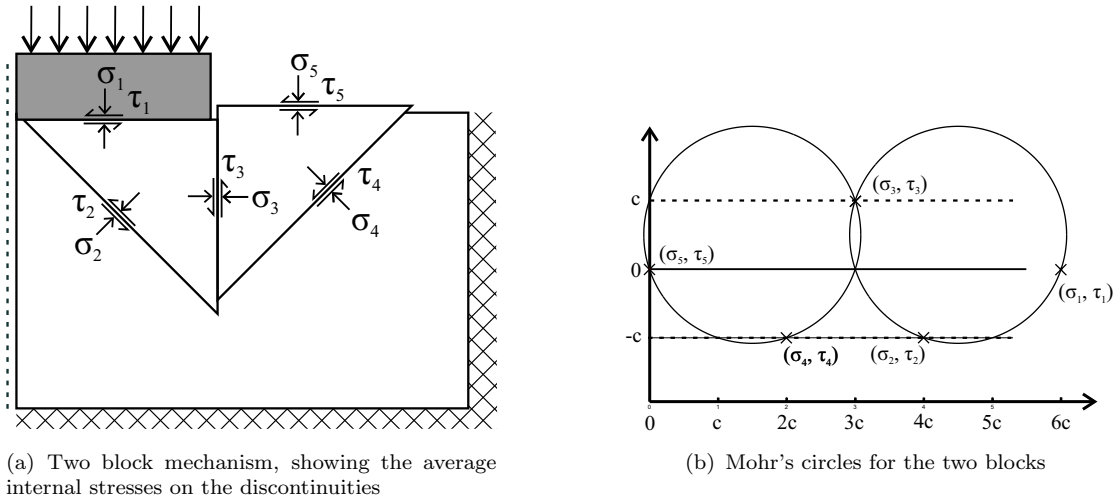


FIGURE 4.19: Solution to the Prandtl problem (assuming a smooth based indenter) using a simple two block mechanism

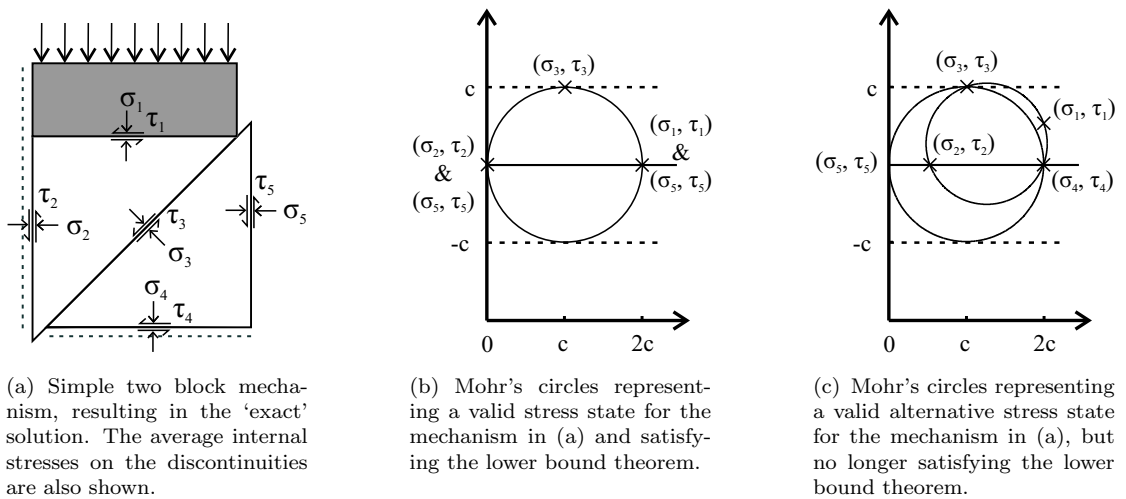


FIGURE 4.20: Compression of a plate of equal height and width between two rough platens

For meshes containing nodes with poorly constrained t^x and t^y values, F_j is likely to be large on at least a fraction of the elements (remember $F = \max(\{1, 2, \dots, F_\kappa\})$; hence, the largest F_j will govern). Take, for example, the results for the Prandtl problem using an ‘original grid’ with 1,075 nodes (see Figure 4.18). For a rough indenter, the most violating element, prior to scaling, is located directly under the indenter (see Figures 4.18(a) and 4.18(b)). The upper boundary of this element is not at yield; therefore, the optimizer has some freedom when selecting the t^x and t^y values at the vertices of this discontinuity. For a smooth indenter, a more accurate pseudo lower bound is obtained as the t^x and t^y values at the vertices of this discontinuity are well constrained (see Figures 4.18(c) and 4.18(d)). Clearly, the pseudo lower bound stress state for the smooth indenter is valid for a rough indenter. Similarly, the results for the compressed plate using mesh C (see Table 4.1 and Figure 4.13(c)) or the Prandtl problem using meshes A, B, C and \tilde{C} (see Table 4.3 and Figures 4.16(a), (b)) are poor. In contrast, the results for the compressed plate using meshes A and B (see Table 4.1 and Figures 4.13(a), (b)) or the Prandtl problem using meshes \tilde{A} and \tilde{B} (see Table 4.3 and Figures 4.16(a), (b)) are much more accurate.

For the compressed block, ‘kinks’ are observed in the mechanism identified by LimitState:GEO and clearly violate compatibility. The quality of the resulting meshes is, therefore, variable and is reflected in the results. Mesh B attempted to correct this deficiency by removing the ‘kinks’. However while better method I results were generally obtained using Mesh B, these results were still variable.

It would therefore appear that method I is not particularly promising, although better solid identification may improve accuracy.

4.5.3.2 Method II

In method II, the t^x and t^y values at the nodes are directly optimized to produce the best pseudo lower bound for a particular mesh. The principal factors resulting

in the poor performance of method I are thus avoided (contrast Figures 4.18(a)-(d) with Figures 4.18(e), (f)). Tables 4.1-4.4 reveal that method II does, indeed, perform much better; however, equivalent upper bounds are still more accurate.

Discontinua are only permitted at the boundary between predefined elements (*i.e.* very similar to the rigid finite element method (RFEM)). Consequently, mesh sensitivity was observed in the results presented in Tables 4.2 and 4.4 (see also Figure 4.17). This mesh sensitivity is the most likely cause of the larger errors (compared to equivalent upper bound solutions). Unsurprisingly, the best results were generally produced for those meshes based on DLO mechanisms (as DLO has the power to identify these reasonably accurately). As these mechanisms do not include stationary regions, further work is needed to identify optimal meshes in stationary regions (for example in the Prandtl problem). The similarity of method II to FELA suggests that FELA may be used with meshes generated from DLO mechanisms.

4.6 Conclusions

- (i) The equilibrium formulation of plane strain translational discontinuity layout optimization (DLO) has been derived using translational stress functions and vector calculus. It has been shown that the derivation allows a deeper understanding of the equilibrium formulation to be obtained. In particular, the reasons for the upper bound nature of the equilibrium formulation become clear.
- (ii) The equilibrium plane strain DLO formulation allows the total internal forces on the potential discontinuities to be determined from scalar values of translational stress functions t^x and t^y at the nodes.
- (iii) Translational stress functions have been used to derive two relaxed, pseudo lower bound methods. Solutions obtained are not required to satisfy rotational equilibrium and are, therefore, lower bounds on the translation only

limit analysis solution. In these methods, a linear variation of the stress functions is assumed across individual triangular elements, used to discretize the problem domain, resulting in a constant stress on individual elements. In method I, nodal t^x and t^y values are determined from an upper bound analysis and are used in the interpolation. The resulting field is scaled to find a pseudo lower bound satisfying the yield condition. In method II, nodal t^x and t^y values are optimized to directly obtain the best possible pseudo lower bound for a particular mesh.

- (iv) The errors in the pseudo lower bounds obtained using method I were much larger than the errors in the corresponding upper bound solutions obtained using LimitState:GEO. This is primarily due to the t^x and t^y values at the nodes being determined from an upper bound analysis.
- (v) Using identical meshes, method II generally obtained considerably better pseudo lower bounds. This can be explained by the direct optimization in method II of the nodal t^x and t^y values. This allows the best possible pseudo lower bound for a given mesh to be obtained. Pseudo lower bounds within 0.5% were obtained for some meshes using method II.
- (vi) However, the errors in the pseudo lower bounds obtained using method II are still larger than the errors in the corresponding upper bound solutions obtained using LimitState:GEO. A possible explanation for this discrepancy is mesh sensitivity. In general better pseudo lower bounds were obtained when using meshes based on mechanisms identified using LimitState:GEO. However, further work is needed to identify optimal meshes in stationary regions.

5 Three-dimensional stress functions

5.1 Introduction

Alternative but equivalent forms of the plane strain and three-dimensional discontinuity layout optimization (DLO) formulations can be obtained from duality principles. In Chapter 4, the dual plane strain formulation was derived from first principles using vector calculus and translational stress functions. This allowed a deeper understanding of the dual formulation and its upper bound status to be obtained. Furthermore, pseudo lower bound formulations which enabled the best translational solution to be bounded were also described in Chapter 4.

Building on this, in this chapter a three-dimensional equilibrium formulation is derived using vector calculus and translational stress functions, allowing further insights into the three-dimensional formulation to be obtained. Translational stress functions are also used to develop a three-dimensional pseudo lower bound formulation, similar to one of the formulations developed in Chapter 4.

5.2 Background

5.2.1 Equilibrium equations

For a three-dimensional body to be in equilibrium, it must satisfy the equilibrium equations

$$\nabla \cdot \boldsymbol{\sigma}^x + p_x = 0 \quad (5.1)$$

$$\nabla \cdot \boldsymbol{\sigma}^y + p_y = 0 \quad (5.2)$$

$$\nabla \cdot \boldsymbol{\sigma}^z + p_z = 0 \quad (5.3)$$

$$\sigma_{xy} = \sigma_{yx}; \quad \sigma_{xz} = \sigma_{zx}; \quad \sigma_{yz} = \sigma_{zy} \quad (5.4)$$

where p_x , p_y , p_z are body forces in the x , y and z directions, respectively;

$$\boldsymbol{\sigma}^x = \sigma_{xx}\mathbf{i} + \sigma_{yx}\mathbf{j} + \sigma_{zx}\mathbf{k}, \quad (5.5)$$

$$\boldsymbol{\sigma}^y = \sigma_{xy}\mathbf{i} + \sigma_{yy}\mathbf{j} + \sigma_{zy}\mathbf{k}, \quad (5.6)$$

$$\boldsymbol{\sigma}^z = \sigma_{xz}\mathbf{i} + \sigma_{yz}\mathbf{j} + \sigma_{zz}\mathbf{k}; \quad (5.7)$$

and where the sign convention is given by Figure 5.1.

The normal stress σ_n and shear stress τ on a plane can be determined from

$$\sigma_n = \mathbf{n}^T \boldsymbol{\sigma} \mathbf{n} \quad (5.8)$$

$$\tau = \sqrt{\mathbf{n}^T \boldsymbol{\sigma} \boldsymbol{\sigma}^T \mathbf{n} - \sigma_n^2} \quad (5.9)$$

where \mathbf{n} is a unit vector normal to the plane and

$$\boldsymbol{\sigma} = \begin{bmatrix} \sigma_{xx} & \sigma_{xy} & \sigma_{xz} \\ \sigma_{yx} & \sigma_{yy} & \sigma_{yz} \\ \sigma_{zx} & \sigma_{zy} & \sigma_{zz} \end{bmatrix} \quad (5.10)$$

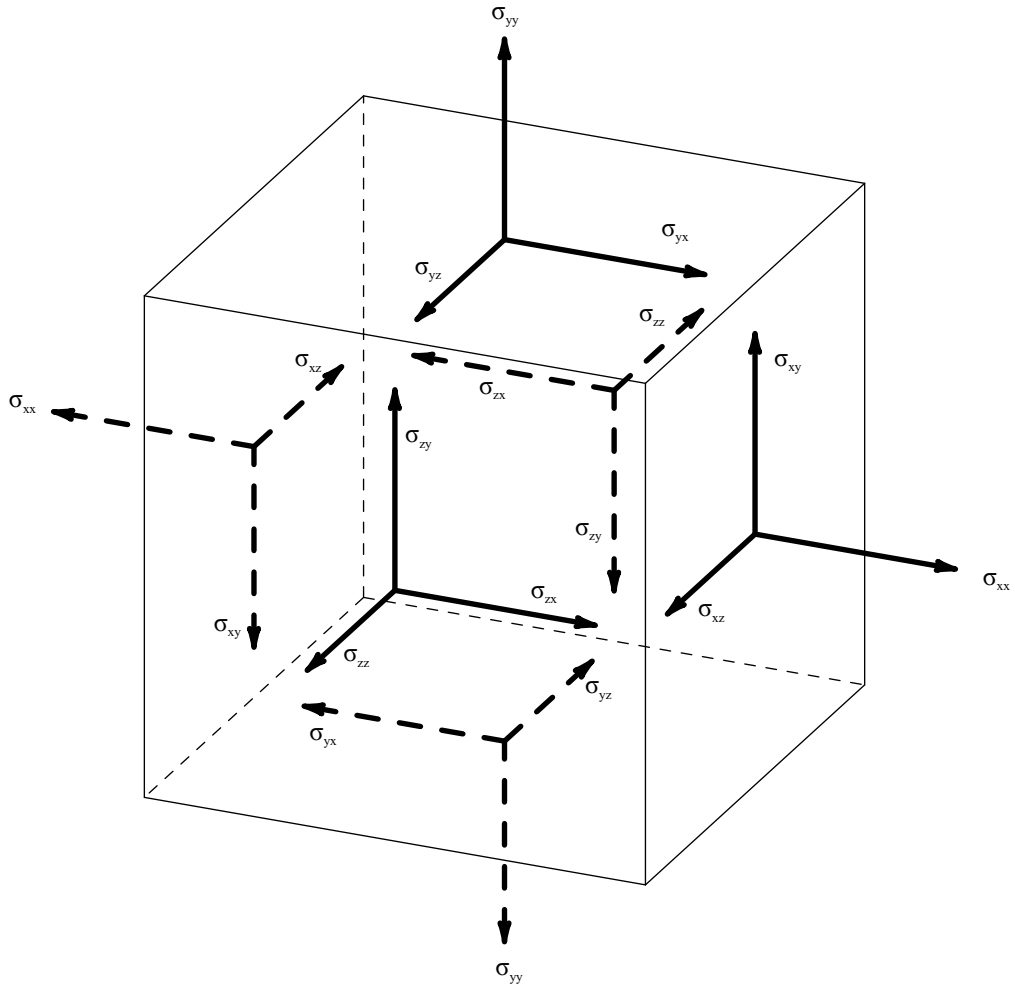


FIGURE 5.1: Sign convention: three-dimensional stress components

Equation (5.4) requires that the stress tensor $\boldsymbol{\sigma}$ is symmetric and can, therefore, be represented by the three Mohr's circles shown in Figure 5.2. In this case, the maximum shear stress τ_{max} can be determined from

$$\tau_{max} = (\sigma_1 - \sigma_3)/2; \quad (5.11)$$

where σ_1 and σ_3 are the maximum and minimum principal stresses, respectively.

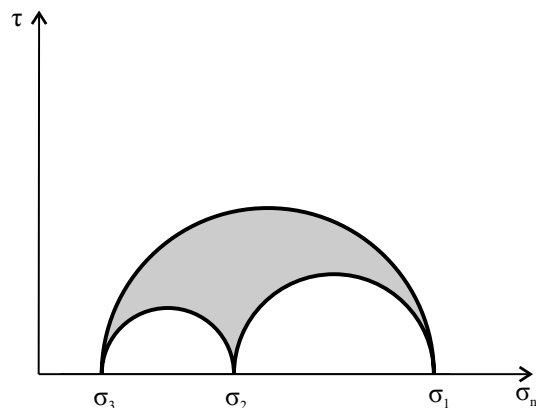


FIGURE 5.2: Mohr's circles representing a symmetric stress tensor; where σ_1 , σ_2 and σ_3 are the principal stresses.

5.2.2 Translational equilibrium

A body in translational equilibrium must satisfy equations (5.1-5.3) but rotational equilibrium, *i.e.* as enforced in equation (5.4), is not necessarily satisfied. Therefore the stress tensor is no longer required to be symmetric. A nonsymmetric stress tensor can no longer be represented by Mohr's circles, as demonstrated by the examples shown in Figure 5.3 (see also e.g. de Figueiredo et al. (2004)). Therefore, τ_{max} can no longer be determined from simple expressions such as equation (5.11). (Note that principal stresses no longer coincide with the extremal normal stresses.) τ_{max} must therefore be obtained by optimizing \mathbf{n} in equation (5.9). Generally, equation (5.9) is non-convex and has multiple local maxima. It is therefore impossible to guarantee that τ_{max} has indeed been found.

Upper bounds on the 'exact' limit load can be obtained by relaxing equilibrium and enforcing only translation equilibrium (see Section 4.2.2). Furthermore, the 'exact' limit load can be obtained for purely translational problems, representing an important subset of geotechnical problems.

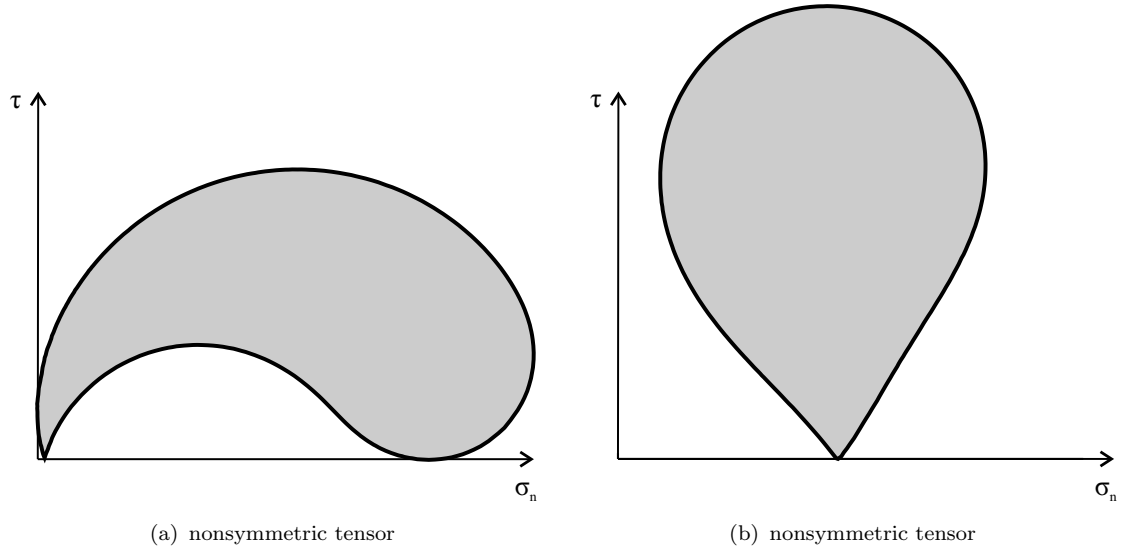


FIGURE 5.3: Shear stress τ plotted against normal stress σ_n for nonsymmetric tensors

5.2.3 Stress functions

In the absence of body forces, the most general three-dimensional stress function is the Beltrami stress function, expressed in tensor calculus form as

$$\boldsymbol{\sigma} = \nabla \times \nabla \times \boldsymbol{\Phi}_s \quad (5.12)$$

where $\boldsymbol{\Phi}_s$ is an arbitrary second-rank symmetric tensor (see Chou and Pagano (1967)). The well known Airy, Maxwell and Morera stress functions are all specialized versions of the Beltrami stress function.

Translational stress functions guarantee translational equilibrium, but do not necessarily satisfy rotational equilibrium. In the following sections, translational stress functions will be used to derive the translational equilibrium form of the three-dimensional DLO formulation.

5.3 Derivation of DLO equilibrium formulation

In the following sections, the three-dimensional equilibrium DLO formulation will be derived. Using an approach similar to that outlined in Section 4.3, the derivation will be framed in terms of vector calculus and stress functions. Firstly, a set of stress functions satisfying translation equilibrium will be derived in Section 5.3.1. In Section 5.3.2, the integral forms of the translational equilibrium equations and stress functions will be developed. In Sections 5.3.3 and 5.3.4, these integral forms will be used to find the applied loads and internal forces on a surface. (Note the term ‘surface’ is used for consistency with vector calculus, but the term ‘discontinuity’ could equally be used.) These internal forces will then be used to enforce the Mohr-Coulomb yield condition. Finally, the equilibrium formulation will be found by discretizing the problem domain and setting up a constrained optimization problem. In Section 5.3.7, insights gained from the derivation will be used to make some observations on the three-dimensional formulation.

5.3.1 Translational stress functions

To determine the total body forces acting on a body, and the total change in the internal stresses across a body, the integral form of the translational equilibrium equations will be used. Translational stress functions are required to achieve this, satisfying equations (5.1-5.3).

Assuming that

$$p_x = \nabla \cdot \mathbf{P}^x, \quad (5.13)$$

$$p_y = \nabla \cdot \mathbf{P}^y, \quad (5.14)$$

$$p_z = \nabla \cdot \mathbf{P}^z; \quad (5.15)$$

where

$$\mathbf{P}^x = \rho^{xx}\mathbf{i} + \rho^{xy}\mathbf{j} + \rho^{xz}\mathbf{k}, \quad (5.16)$$

$$\mathbf{P}^y = \rho^{yx}\mathbf{i} + \rho^{yy}\mathbf{j} + \rho^{yz}\mathbf{k}, \quad (5.17)$$

$$\mathbf{P}^z = \rho^{zx}\mathbf{i} + \rho^{zy}\mathbf{j} + \rho^{zz}\mathbf{k}. \quad (5.18)$$

ρ^{xx} , ρ^{yx} and ρ^{zx} are forces per unit area acting on the zy plane in the x , y and z directions, respectively. ρ^{xy} , ρ^{yy} and ρ^{zy} are forces per unit area acting on the xz plane in the x , y and z directions, respectively. ρ^{xz} , ρ^{yz} and ρ^{zz} are forces per unit area acting on the xy plane in the x , y and z directions, respectively. ρ^{xx} , ρ^{yx} , \dots , ρ^{zz} are analogous to ω^x , ε^x , ω^y and ε^y in Chapter 4.

Vector functions

$$\Phi^x = \phi^{xx}\mathbf{i} + \phi^{xy}\mathbf{j} + \phi^{xz}\mathbf{k}, \quad (5.19)$$

$$\Phi^y = \phi^{yx}\mathbf{i} + \phi^{yy}\mathbf{j} + \phi^{yz}\mathbf{k}, \quad (5.20)$$

$$\Phi^z = \phi^{zx}\mathbf{i} + \phi^{zy}\mathbf{j} + \phi^{zz}\mathbf{k}, \quad (5.21)$$

satisfying equations (5.1-5.3), must be translational stress functions (see Chou and Pagano (1967)); where

$$\boldsymbol{\sigma}^x = \nabla \times \Phi^x - \mathbf{P}^x, \quad (5.22)$$

$$\boldsymbol{\sigma}^y = \nabla \times \Phi^y - \mathbf{P}^y, \quad (5.23)$$

$$\boldsymbol{\sigma}^z = \nabla \times \Phi^z - \mathbf{P}^z. \quad (5.24)$$

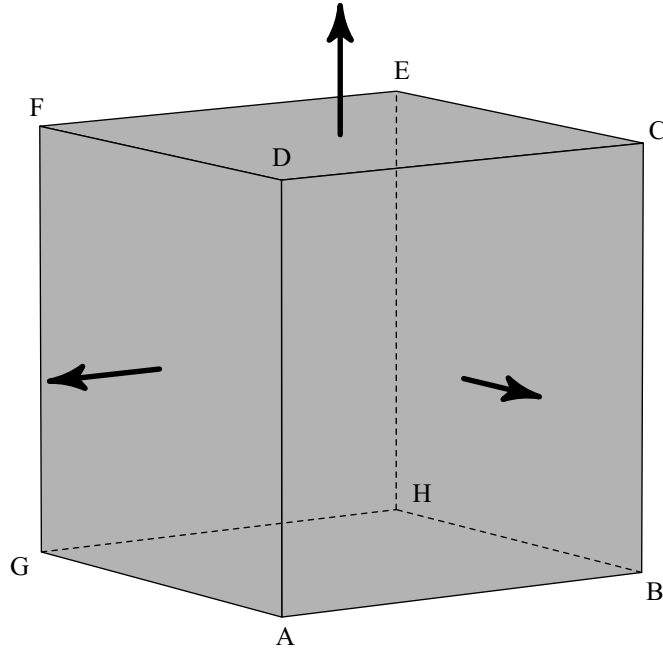
The stress tensor $\boldsymbol{\sigma}$ can now be rewritten as

$$\boldsymbol{\sigma} = \begin{bmatrix} \left(\frac{\partial \phi^{xz}}{\partial y} - \frac{\partial \phi^{xy}}{\partial z} \right) - \rho^{xx} & \left(\frac{\partial \phi^{yz}}{\partial y} - \frac{\partial \phi^{yy}}{\partial z} \right) - \rho^{yx} & \left(\frac{\partial \phi^{zz}}{\partial y} - \frac{\partial \phi^{zy}}{\partial z} \right) - \rho^{zx} \\ \left(\frac{\partial \phi^{xx}}{\partial z} - \frac{\partial \phi^{xz}}{\partial x} \right) - \rho^{xy} & \left(\frac{\partial \phi^{yx}}{\partial z} - \frac{\partial \phi^{yz}}{\partial x} \right) - \rho^{yy} & \left(\frac{\partial \phi^{zx}}{\partial z} - \frac{\partial \phi^{zz}}{\partial x} \right) - \rho^{zy} \\ \left(\frac{\partial \phi^{xy}}{\partial x} - \frac{\partial \phi^{xx}}{\partial y} \right) - \rho^{xz} & \left(\frac{\partial \phi^{yy}}{\partial x} - \frac{\partial \phi^{yx}}{\partial y} \right) - \rho^{yz} & \left(\frac{\partial \phi^{zy}}{\partial x} - \frac{\partial \phi^{zz}}{\partial y} \right) - \rho^{zz} \end{bmatrix} \quad (5.25)$$

where $\boldsymbol{\sigma}$ is, generally, nonsymmetric.

5.3.2 Integral form

The integral forms of equations (5.1-5.3) and, hence, of the stress functions can be found by considering a body U , shown in Figure 5.4. Body U is bounded by a closed surface V , comprised of surfaces $ABCD$, $CEFD$, $ADFG$, $AGHB$,

FIGURE 5.4: A body U bounded by a closed surface V

$EHGF$ and $BHEC$. These integral forms will be used in Sections 5.3.3 and 5.3.4 to determine the external and internal forces on an arbitrary surface.

Integrating equations (5.1-5.3) over U , equations (5.26-5.28) are obtained, where the right hand sides equal the total body forces on U in the x , y and z directions, respectively. The left hand sides of the equations equal the negative of the total change in the internal stress over U in the x , y and z directions, respectively.

$$- \iiint_U \nabla \cdot \boldsymbol{\sigma}^x dV = \iiint_U \nabla \cdot \mathbf{P}^x dV \quad (5.26)$$

$$- \iiint_U \nabla \cdot \boldsymbol{\sigma}^y dV = \iiint_U \nabla \cdot \mathbf{P}^y dV \quad (5.27)$$

$$- \iiint_U \nabla \cdot \boldsymbol{\sigma}^z dV = \iiint_U \nabla \cdot \mathbf{P}^z dV \quad (5.28)$$

Equations (5.26-5.28) are necessary, but not sufficient, to ensure translational equilibrium. As Φ^x , Φ^y , Φ^z , \mathbf{P}^x , \mathbf{P}^y and \mathbf{P}^z from Section 5.3.1 satisfy translational, these must also satisfy equations (5.26-5.28).

Considering the left hand and right hand sides separately, the total body forces on U can be found using Gauss's theorem (note that a closed surface with outward facing normals, as shown in Figure 5.4, is taken as positive throughout this chapter):

$$\iiint_U \nabla \cdot \mathbf{P}^x dV = \oiint_V \mathbf{P}^x \cdot d\mathbf{S}, \quad (5.29)$$

$$\iiint_U \nabla \cdot \mathbf{P}^y dV = \oiint_V \mathbf{P}^y \cdot d\mathbf{S}, \quad (5.30)$$

$$\iiint_U \nabla \cdot \mathbf{P}^z dV = \oiint_V \mathbf{P}^z \cdot d\mathbf{S}. \quad (5.31)$$

The total change in the internal stresses on U in the x , y and z directions, respectively, can also be found using Gauss's theorem:

$$\iiint_G \nabla \cdot \boldsymbol{\sigma}^x dV = \oiint_V \boldsymbol{\sigma}^x \cdot d\mathbf{S} = \oiint_V \nabla \times \boldsymbol{\Phi}^x \cdot d\mathbf{S} - \oiint_V \mathbf{P}^x \cdot d\mathbf{S}, \quad (5.32)$$

$$\iiint_G \nabla \cdot \boldsymbol{\sigma}^y dV = \oiint_V \boldsymbol{\sigma}^y \cdot d\mathbf{S} = \oiint_V \nabla \times \boldsymbol{\Phi}^y \cdot d\mathbf{S} - \oiint_V \mathbf{P}^y \cdot d\mathbf{S}, \quad (5.33)$$

$$\iiint_G \nabla \cdot \boldsymbol{\sigma}^z dV = \oiint_V \boldsymbol{\sigma}^z \cdot d\mathbf{S} = \oiint_V \nabla \times \boldsymbol{\Phi}^z \cdot d\mathbf{S} - \oiint_V \mathbf{P}^z \cdot d\mathbf{S} \quad (5.34)$$

revealing that

$$\oiint_V \nabla \times \boldsymbol{\sigma}^x \cdot d\mathbf{S} = 0, \quad \oiint_V \nabla \times \boldsymbol{\sigma}^y \cdot d\mathbf{S} = 0, \quad \oiint_V \nabla \times \boldsymbol{\sigma}^z \cdot d\mathbf{S} = 0$$

as would be expected from vector calculus.

The integral of a closed surface can be found by summing the integrals of component surfaces. For the example shown in Figure 5.4:

$$\begin{aligned} \oiint_V \boldsymbol{\sigma}^x \cdot d\mathbf{S} &= \iint_{ABCD} \boldsymbol{\sigma}^x \cdot d\mathbf{S} + \iint_{CEFD} \boldsymbol{\sigma}^x \cdot d\mathbf{S} + \iint_{ADFG} \boldsymbol{\sigma}^x \cdot d\mathbf{S} \\ &+ \iint_{AGHB} \boldsymbol{\sigma}^x \cdot d\mathbf{S} + \iint_{EHGF} \boldsymbol{\sigma}^x \cdot d\mathbf{S} + \iint_{BHEC} \boldsymbol{\sigma}^x \cdot d\mathbf{S}; \end{aligned}$$

where $ABCD$, $CEFD$, $ADFG$, $AGHB$, $EHGF$ and $BHEC$ all have outward normals.

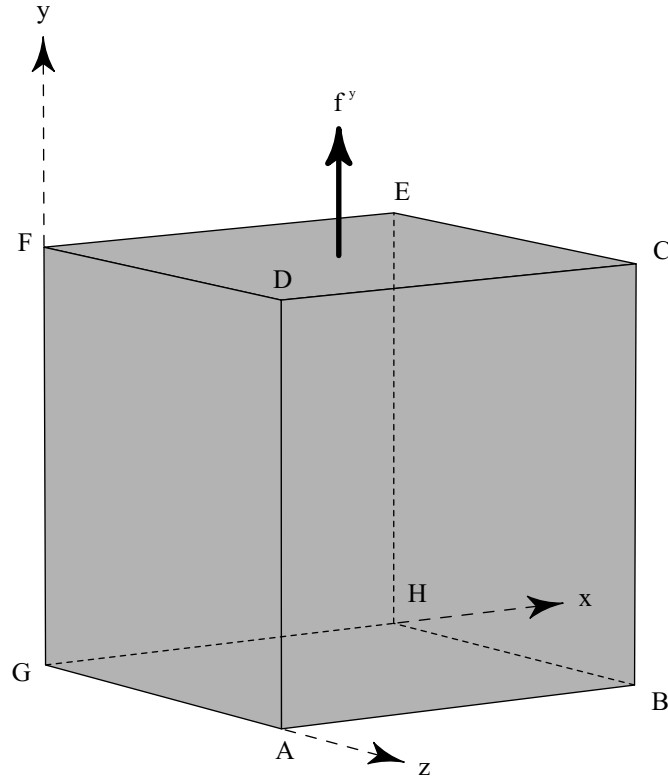
5.3.3 Application of loads

The integral forms, developed in Section 5.3.2, allow application of loads to a body via its boundaries in a manner similar to that outlined in Section 4.3.3. Consider the cuboidal body U shown in Figure 5.5. A load f^y in the positive y direction is applied to $CEFD$, where boundary $CEFD$ is parallel to the xz plane and has an outward facing normal vector $\{0, 1, 0\}^T$. Assuming $\mathbf{P}^y = 0$ at every point not located on $CEFD$, $\iint_{CEFD} \mathbf{P}^y \cdot d\mathbf{S} = f^y$. This can easily be demonstrated using equation (5.30). Observing that $CEFD$ is located on plane described by $0 \cdot x + 1 \cdot y + 0 \cdot z = 1$,

$$\begin{aligned} \iint_{CEFD} \mathbf{P}^y \cdot d\mathbf{S} &= \iint_{CEFD} \left(-\rho^{yx} \frac{\partial y}{\partial x} + \rho^{yy} - \rho^{yz} \frac{\partial y}{\partial z} \right) dx dz & (5.36) \\ &= \iint_{CEFD} (-\rho^{yx} \cdot 0 + \rho^{yy} - \rho^{yz} \cdot 0) dx dz \\ &= \iint_{CEFD} \rho^{yy} dx dz \end{aligned}$$

It can therefore be concluded from equation (5.36) that ρ^{yy} must be the force per unit area acting in the y direction on the xz plane. The definitions of ρ^{xx} , ρ^{xy} , ..., ρ^{zz} in Section 5.3.1 can be, similarly, confirmed.

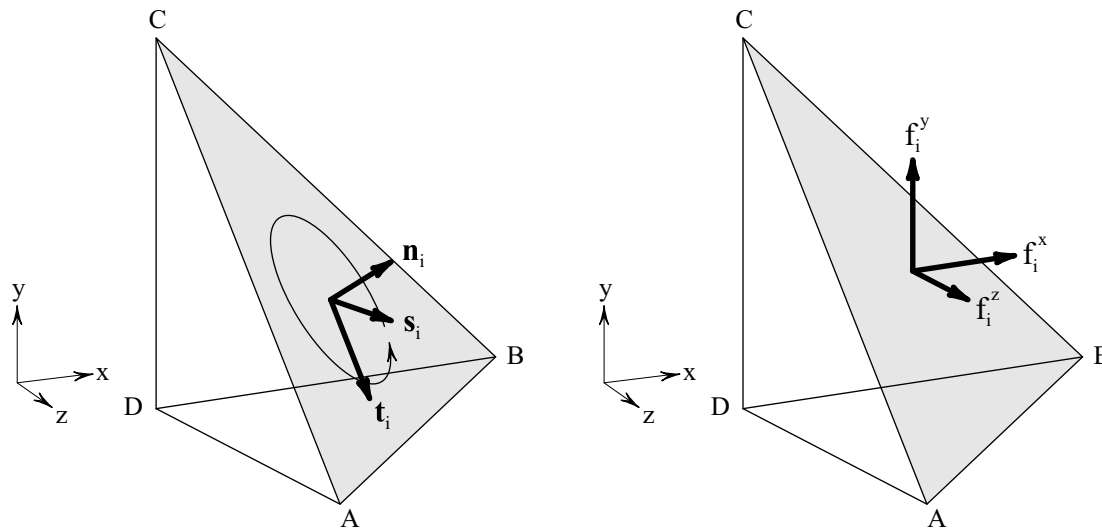
Consider an arbitrary internal surface i with a unit normal \mathbf{n}_i . Take, for example, the surface \overrightarrow{ABC} in Figure 5.6(a). Loads f_i^x , f_i^y and f_i^z in Figure 5.6(b) can be applied to body $ABCD$ via surface \overrightarrow{ABC} by surface integrals $\iint_{ABC} \mathbf{P}^x \cdot d\mathbf{S} = f_i^x$, $\iint_{ABC} \mathbf{P}^y \cdot d\mathbf{S} = f_i^y$ and $\iint_{ABC} \mathbf{P}^z \cdot d\mathbf{S} = f_i^z$. Assuming $\mathbf{P}^x = \mathbf{P}^y = \mathbf{P}^z = 0$ at every point not located on \overrightarrow{ABC} , the total applied loads on $ABCD$ in the x , y and z directions must equal f_i^x , f_i^y and f_i^z , respectively. This can easily be demonstrated using equations (5.29-5.31).

FIGURE 5.5: A body with load f^y applied to boundary $CEFD$

As shown in Figure 5.6(c), f_i^x , f_i^y and f_i^z can be transformed to a coordinate system local to surface i (in this case \overrightarrow{ABC}) as follows:

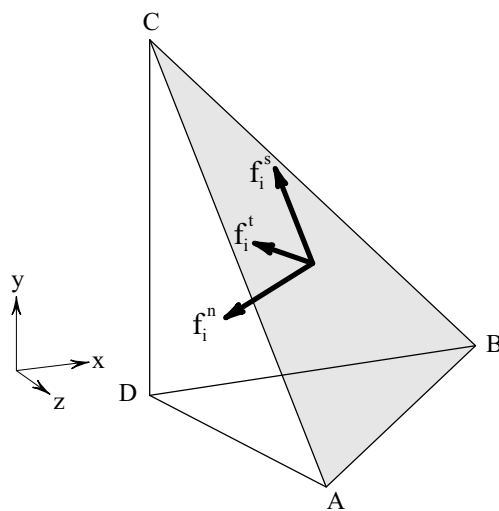
$$\begin{bmatrix} f_i^n \\ f_i^s \\ f_i^t \end{bmatrix} = - \begin{bmatrix} \mathbf{n}_i^T \\ \mathbf{s}_i^T \\ \mathbf{t}_i^T \end{bmatrix} \begin{bmatrix} \iint_{AHF} \mathbf{P}^x \cdot d\mathbf{S} \\ \iint_{AHF} \mathbf{P}^y \cdot d\mathbf{S} \\ \iint_{AHF} \mathbf{P}^z \cdot d\mathbf{S} \end{bmatrix} = -\mathbf{T}_i^T \begin{bmatrix} f_i^x \\ f_i^y \\ f_i^z \end{bmatrix} \quad (5.37)$$

where \mathbf{s}_i and \mathbf{t}_i are unit column vectors describing the local axes on the surface i , f_i^n , f_i^s and f_i^t are forces in the \mathbf{n}_i , \mathbf{s}_i and \mathbf{t}_i directions respectively and \mathbf{T}_i is the transformation matrix described in Section 3.2.1. In this coordinate system, positive f_i^x , f_i^y and f_i^z result in a tensile force f_i^n . Therefore, tensile forces f_i^n must be positive in this new coordinate system.



(a) Arbitrary surface \overline{ABC} with a normal \mathbf{n}_i (determined using the 'right hand screw rule'++). \mathbf{s}_i and \mathbf{t}_i are orthogonal axis in the plane of \overline{ABC} .

(b) Loads f_i^x , f_i^y and f_i^z applied to body $ABCD$ via \overline{ABC} .



(c) Loads f_i^x , f_i^y and f_i^z transformed to a coordinate system local to \overline{ABC} ; where f_i^n , f_i^s and f_i^t are loads in the \mathbf{n}_i , \mathbf{s}_i and \mathbf{t}_i directions, respectively.

FIGURE 5.6: Load applied to a surface \overline{ABC} .

Also f_i^n , f_i^s and f_i^t can be split into dead and live load components as follows:

$$\begin{bmatrix} f_i^n \\ f_i^s \\ f_i^t \end{bmatrix} = \begin{bmatrix} f_{Di}^n \\ f_{Di}^s \\ f_{Di}^t \end{bmatrix} + \lambda \begin{bmatrix} f_{Li}^n \\ f_{Li}^s \\ f_{Li}^t \end{bmatrix} \quad (5.38)$$

where $f_{Di}^n, f_{Li}^n; f_{Di}^s, f_{Li}^s$ and f_{Di}^t, f_{Li}^t are respectively the dead and live loads in the $\mathbf{n}_i, \mathbf{s}_i$ and \mathbf{t}_i directions, and λ is an adequacy factor on the live loads. If path i is an internal boundary, f_i^n, f_i^s , and f_i^t must be the sum of the total load applied between the path and an external boundary, excluding any load applied to the external boundary. The direction of this summation is arbitrary, but must be consistent for all paths considered. This definition of f_i^n, f_i^s and f_i^t is consistent with that described in Section 3.2.5 and can be derived using a similar approach to that outlined Appendix E.4.

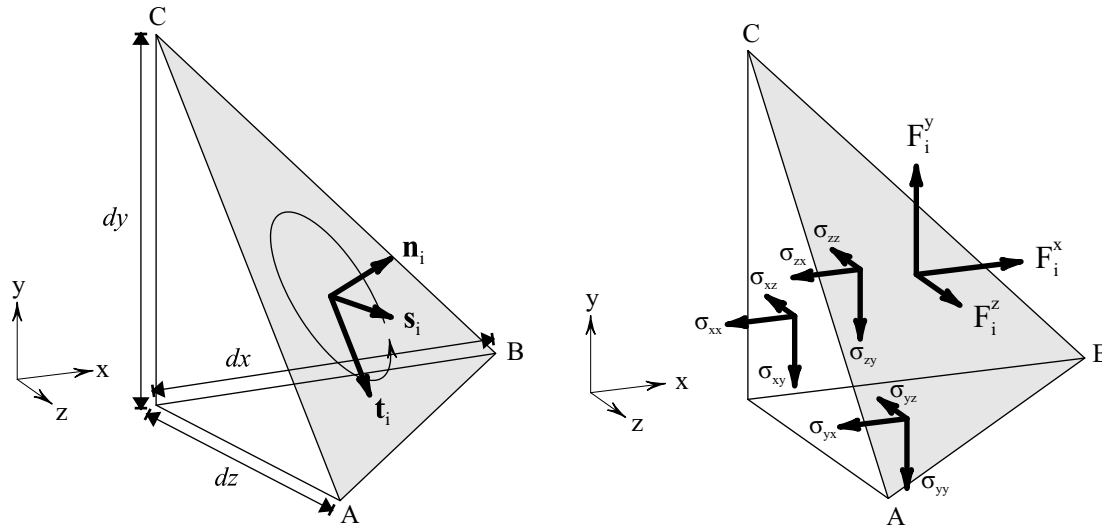
5.3.4 Internal forces on a surface

In the following section, the forces on an arbitrary internal surface i due to the internal stresses will be determined. In Section 5.3.5, these internal forces will be used to enforce the Mohr-Coulomb yield condition.

Firstly, consider an arbitrary surface i with a normal \mathbf{n}_i . Take, for example, surface \overrightarrow{ABC} in Figure 5.7(a), bounding an infinitesimal element. Examining equations (5.32-5.34), it is clear that

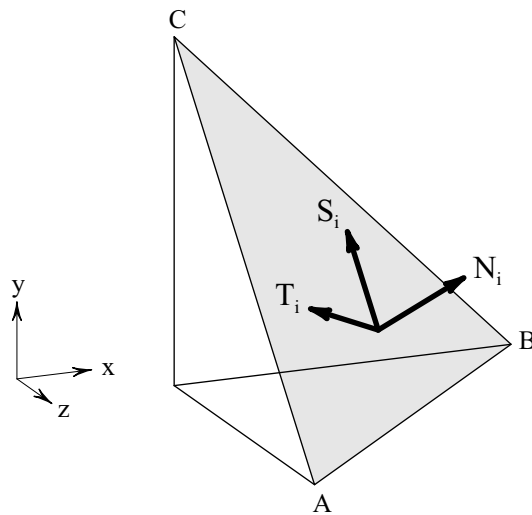
$$\begin{aligned} F_i^x &= \iint_{ABC} \boldsymbol{\sigma}^x \cdot d\mathbf{S} & (5.39) \\ &= \iint_{ABC} \sigma_{xx} \cdot dzdy + \iint_{ABC} \sigma_{yx} \cdot dzdx + \iint_{ABC} \sigma_{zx} \cdot dxdy \\ &= \iint_{ABC} \nabla \times \boldsymbol{\Phi}^x \cdot d\mathbf{S} - \iint_{ABC} \mathbf{P}^x \cdot d\mathbf{S}, \end{aligned}$$

$$\begin{aligned} F_i^y &= \iint_{ABC} \boldsymbol{\sigma}^y \cdot d\mathbf{S} & (5.40) \\ &= \iint_{ABC} \sigma_{xy} \cdot dzdy + \iint_{ABC} \sigma_{yy} \cdot dzdx + \iint_{ABC} \sigma_{zy} \cdot dxdy \\ &= \iint_{ABC} \nabla \times \boldsymbol{\Phi}^y \cdot d\mathbf{S} - \iint_{ABC} \mathbf{P}^y \cdot d\mathbf{S}, \end{aligned}$$



(a) Arbitrary surface \overline{ABC} , bounding an infinitesimal tetrahedral element, with a normal \mathbf{n}_i (determined using the 'righthand screw rule'). \mathbf{s}_i and \mathbf{t}_i are orthogonal axis in the plane of \overline{ABC} .

(b) Internal forces F_i^x , F_i^y and F_i^z on \overline{ABC} in the x , y and z directions, respectively. The internal stresses on the remaining faces of the element are also shown.



(c) Internal forces F_i^x , F_i^y and F_i^z transformed into a coordinate system local to \overline{ABC} ; where N_i is a force normal to \overline{ABC} and positive in tension; and S_i and T_i are shear forces on \overline{ABC} .

FIGURE 5.7: Internal forces on an arbitrary surface \overline{ABC}

$$\begin{aligned}
F_i^z &= \iint_{ABC} \boldsymbol{\sigma}^z \cdot d\mathbf{S} \\
&= \iint_{ABC} \sigma_{xz} \cdot dzdy + \iint_{ABC} \sigma_{yz} \cdot dzdx + \iint_{ABC} \sigma_{zz} \cdot dxdy \\
&= \iint_{ABC} \nabla \times \boldsymbol{\Phi}^z \cdot d\mathbf{S} - \iint_{ABC} \mathbf{P}^z \cdot d\mathbf{S};
\end{aligned} \tag{5.41}$$

where F_i^x , F_i^y and F_i^z (see Figure 5.7(b)) are the total forces on \overrightarrow{ABC} due to the internal stresses, in the x , y and z directions respectively.

The surface integrals $\iint_{ABC} \nabla \times \boldsymbol{\Phi}^x \cdot d\mathbf{S}$, $\iint_{ABC} \nabla \times \boldsymbol{\Phi}^y \cdot d\mathbf{S}$ and $\iint_{ABC} \nabla \times \boldsymbol{\Phi}^z \cdot d\mathbf{S}$ can be found using Stokes' theorem. $\iint_{ABC} \nabla \times \boldsymbol{\Phi}^x \cdot d\mathbf{S}$, for example, can be found as follows:

$$\iint_{ABC} \nabla \times \boldsymbol{\Phi}^x \cdot d\mathbf{S} = \oint_{ABC} \boldsymbol{\Phi}^x \cdot d\mathbf{r} = \int_A^B \boldsymbol{\Phi}^x \cdot d\mathbf{r} + \int_B^C \boldsymbol{\Phi}^x \cdot d\mathbf{r} + \int_C^A \boldsymbol{\Phi}^x \cdot d\mathbf{r}. \tag{5.42}$$

Therefore, equations (5.39-5.41) can be rewritten as

$$\begin{bmatrix} F_i^x \\ F_i^y \\ F_i^z \end{bmatrix} = \begin{bmatrix} t_{AB}^x & t_{BC}^x & t_{CA}^x \\ t_{AB}^y & t_{BC}^y & t_{CA}^y \\ t_{AB}^z & t_{BC}^z & t_{CA}^z \end{bmatrix} \begin{bmatrix} 1 \\ 1 \\ 1 \end{bmatrix} - \begin{bmatrix} f_i^x \\ f_i^y \\ f_i^z \end{bmatrix} \tag{5.43}$$

where t_{AB}^M , t_{BC}^M and t_{CA}^M equal the line integrals $\int_A^B \boldsymbol{\Phi}^M \cdot d\mathbf{r}$, $\int_B^C \boldsymbol{\Phi}^M \cdot d\mathbf{r}$ and $\int_C^A \boldsymbol{\Phi}^M \cdot d\mathbf{r}$, respectively, where $M = x, y$ or z . Also $\iint_{ABC} \mathbf{P}^x \cdot d\mathbf{S} = f_i^x$, $\iint_{ABC} \mathbf{P}^y \cdot d\mathbf{S} = f_i^y$ and $\iint_{ABC} \mathbf{P}^z \cdot d\mathbf{S} = f_i^z$ (see Section 5.3.3).

As shown in Figure 5.7(c), F_i^x , F_i^y and F_i^z can be transformed into a coordinate system local to surface i as follows:

$$\begin{bmatrix} N_i \\ -S_i \\ -T_i \end{bmatrix} = \mathbf{T}_i^T \begin{bmatrix} t_{AB}^x \\ t_{AB}^y \\ t_{AB}^z \end{bmatrix} + \mathbf{T}_i^T \begin{bmatrix} t_{BC}^x \\ t_{BC}^y \\ t_{BC}^z \end{bmatrix} + \mathbf{T}_i^T \begin{bmatrix} t_{CA}^x \\ t_{CA}^y \\ t_{CA}^z \end{bmatrix} - \mathbf{T}_i^T \begin{bmatrix} f_i^x \\ f_i^y \\ f_i^z \end{bmatrix} \tag{5.44}$$

where N_i is a normal force to surface i in the \mathbf{n}_i direction, S_i and T_i are shear loads in the $-\mathbf{s}_i$ and $-\mathbf{t}_i$ directions respectively, and N_i is taken as tensile positive. Equation (5.44) can be rewritten as

$$-\mathbf{f}_{Di} = \lambda \mathbf{f}_{Li} - \mathbf{q}_i + \sum_{j \in K_i} \mathbf{B}_{ij}^T \mathbf{t}_j; \quad (5.45)$$

where set $K_i = \{AB, BC, CA\}$, \mathbf{B}_{ij} is a local compatibility matrix defined in Appendix B and Section 3.2.1. Also $\mathbf{t}_j^T = \{t_j^x, t_j^y, t_j^z\}$, $\mathbf{q}_i^T = \{N_i, -S_i, -T_i\}$, $\mathbf{f}_{Di}^T = \{f_{Di}^n, f_{Di}^s, f_{Di}^t\}$ and $\mathbf{f}_{Li}^T = \{f_{Li}^n, f_{Li}^s, f_{Li}^t\}$ (see equations (5.37) and (5.38)).

5.3.5 Enforcing the Mohr-Coulomb yield condition on a surface

Assuming a uniform distribution of the stresses across surface i , the normal stress and the maximum shear stress must equal N_i/a_i and $(\sqrt{S_i^2 + T_i^2})/a_i$, respectively, where a_i is the area of surface i . Assuming also that failure occurs along i , the Mohr-Coulomb yield condition can be enforced as follows:

$$P_i + N_i \tan \phi_i \leq a_i c_i, \quad (5.46)$$

$$P_i = \sqrt{S_i^2 + T_i^2}; \quad (5.47)$$

where c_i and ϕ_i are respectively the cohesive strength and angle of friction on surface i , and P_i is the resultant shear force.

Equations (5.46) and (5.47) can be written as

$$P_i + \chi_i + N_i \tan \phi_i = a_i c_i, \quad (5.48)$$

$$P_i + \chi_i \geq \sqrt{S_i^2 + T_i^2}; \quad (5.49)$$

where $\chi_i \geq 0$ is a positive slack variable. Introducing a variable $L_i = P_i + \chi_i$, equations (5.48) and (5.49) become

$$L_i + N_i \tan \phi_i = a_i c_i, \quad (5.50)$$

$$L_i \geq \sqrt{S_i^2 + T_i^2}; \quad (5.51)$$

where equation (5.51) is a second order cone. As $L_i \geq 0$, equations (5.50) and (5.51) must be equivalent to equations (5.46) and (5.47).

5.3.6 Discretization

Given a problem domain with known boundary and loading conditions, a constrained optimization problem can be set up to find the maximum adequacy factor λ on the live loads. For this it is necessary to discretize the problem domain using n nodes and to assume that the line integrals t^x , t^y and t^z can only be determined along l paths, joining every unique pair of nodes. Suppose also that these paths are joined to create m simple polygonal surfaces and that f_{Li}^n , f_{Li}^s , f_{Li}^t , f_{Di}^n , f_{Di}^s and f_{Di}^t are known for all paths ($i = 1, 2, \dots, m$). Applying equations (5.45), (5.50) and (5.51) for all m surfaces leads to a constrained SOCP problem, identical to the dual of kinematic formulation outlined in Section 3.2.4. In matrix form, the dual equilibrium formulation is as follows:

$$\max \lambda \quad (5.52a)$$

subject to

$$\mathbf{B}^T \mathbf{t} + \lambda \mathbf{f}_L - \mathbf{q} = -\mathbf{f}_D \quad (5.52b)$$

$$\mathbf{N}^T \mathbf{t} + \mathbf{L} = 0 \quad (5.52c)$$

$$L_i \geq \sqrt{S_i^2 + T_i^2} \quad \forall i \in \{1, \dots, m\} \quad (5.52d)$$

where $\mathbf{t}^t = \{t_1^x, t_1^y, t_i^z, t_2^x, t_2^y, t_2^z, \dots, t_i^z\}^T$, $\mathbf{L} = \{L_1, L_2, \dots, L_m\}^T$, $\mathbf{q} = \{N_1, -S_1, -T_2, N_2, -S_2, -T_2, \dots, -T_m\}^T$ and where \mathbf{B} , \mathbf{f}_L , \mathbf{f}_D are identical to those described in Chapter 3.

5.3.7 Discussion

As confirmed by the derivation, the observations made in Section 4.3.7 on the upper bound nature of the DLO procedure are still valid. The observations are summarized below.

- (i) Rotational equilibrium is not enforced.
- (ii) The yield condition is only enforced on the (surface) discontinuities.
- (iii) The yield condition is only enforced in an average sense on the (surface) discontinuities.
- (iv) The stress field is not extended to ensure the stress field is admissible outside the discretized problem domain.

In the three-dimensional kinematic formulation, compatibility is enforced along the edges. In the dual the t values are similarly associated with edges rather nodes (as in the plane strain formulation). Consider for example the line integral $\int_A^B \boldsymbol{\sigma}^x \cdot d\mathbf{r}$ in the plane strain formulation (see Chapter 4):

$$\int_A^B \boldsymbol{\sigma}^x \cdot d\mathbf{r} = \int_A^B \nabla t^x \cdot d\mathbf{r} - \int_A^B \mathbf{P}^x \cdot d\mathbf{r} \quad (5.53a)$$

$$= t_B^x - t_A^x - f_i^x \quad (5.53b)$$

$f_i^x = \int_A^B \mathbf{P}^x \cdot d\mathbf{r}$ is path dependant, but is known *a priori*. $\int_A^B \nabla t^x \cdot d\mathbf{r}$, however, is not known *a priori*, but can be determined using the gradient theorem and from the t_B^x , t_A^x values associated with the nodes. In contrast, consider the line integral in the three-dimensional formulation:

$$\int_A^B \boldsymbol{\Phi}^x \cdot d\mathbf{r} = \int_A^B \phi^{xx} dx + \int_A^B \phi^{xy} dy + \int_A^B \phi^{xz} dz \quad (5.54)$$

In this case, the gradient theorem cannot be used and, therefore, $\int_A^B \boldsymbol{\Phi}^x \cdot d\mathbf{r}$ cannot be determined from the t values at the nodes. Consequently, $\int_A^B \boldsymbol{\Phi}^x \cdot d\mathbf{r}$ must be obtained by some other means. $\int_A^B \boldsymbol{\Phi}^x \cdot d\mathbf{r}$, for example, could be included directly as an optimization variable (as in the dual formulation described above). In the three-dimensional equilibrium formulation, line integrals along the edges are used to determine the internal forces on the discontinuities or surfaces.

5.4 Pseudo lower bound

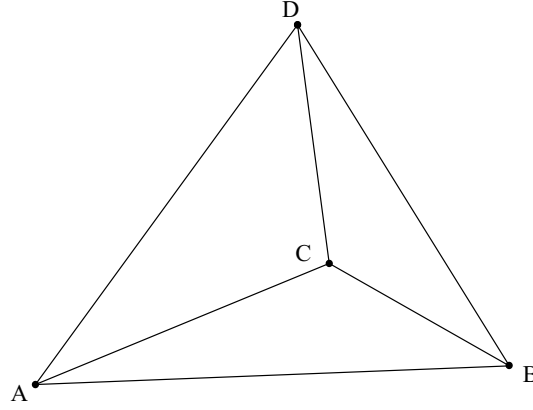


FIGURE 5.8: A tetrahedral element j with vertices A , B , C and D

In the following section, a three-dimensional method, similar to method I described in Section 4.4, will be developed for a weightless Tresca material. In this method, the problem domain is split into tetrahedral elements. The stress functions Φ^x , Φ^y and Φ^z from Section 5.3 are assumed to vary linearly across each element, resulting in a constant stress state on each tetrahedral element. The linear variation of the stress functions across the tetrahedral element j in Figure 5.8 are described by equation (5.55).

$$\begin{bmatrix} \Phi^x \\ \Phi^y \\ \Phi^z \end{bmatrix} = \begin{bmatrix} \phi^{xx} \\ \phi^{yx} \\ \phi^{zx} \end{bmatrix} \mathbf{i} + \begin{bmatrix} \phi^{xy} \\ \phi^{yy} \\ \phi^{zy} \end{bmatrix} \mathbf{j} + \begin{bmatrix} \phi^{xz} \\ \phi^{yz} \\ \phi^{zz} \end{bmatrix} \mathbf{j} \quad (5.55a)$$

$$\begin{bmatrix} \Phi^x \\ \Phi^y \\ \Phi^z \end{bmatrix} = \begin{bmatrix} a_{j1}^x & a_{j2}^x & a_{j3}^x & a_{j4}^x \\ a_{j1}^y & a_{j2}^y & a_{j3}^y & a_{j4}^y \\ a_{j1}^z & a_{j2}^z & a_{j3}^z & a_{j4}^z \end{bmatrix} \begin{bmatrix} x \\ y \\ z \\ 1 \end{bmatrix} \mathbf{i} + \begin{bmatrix} a_{j5}^x & a_{j6}^x & a_{j7}^x & a_{j8}^x \\ a_{j5}^y & a_{j6}^y & a_{j7}^y & a_{j8}^y \\ a_{j5}^z & a_{j6}^z & a_{j7}^z & a_{j8}^z \end{bmatrix} \begin{bmatrix} x \\ y \\ z \\ 1 \end{bmatrix} \mathbf{j} \\ + \begin{bmatrix} a_{j9}^x & a_{j10}^x & a_{j11}^x & a_{j12}^x \\ a_{j9}^y & a_{j10}^y & a_{j11}^y & a_{j12}^y \\ a_{j9}^z & a_{j10}^z & a_{j11}^z & a_{j12}^z \end{bmatrix} \begin{bmatrix} x \\ y \\ z \\ 1 \end{bmatrix} \mathbf{k} \quad (5.55b)$$

Assuming no forces are applied on the internal boundaries, the stress tensor

$$\boldsymbol{\sigma}_j = \begin{bmatrix} \left(\frac{\partial \phi^{xz}}{\partial y} - \frac{\partial \phi^{xy}}{\partial z} \right) & \left(\frac{\partial \phi^{yz}}{\partial y} - \frac{\partial \phi^{yy}}{\partial z} \right) & \left(\frac{\partial \phi^{zz}}{\partial y} - \frac{\partial \phi^{zy}}{\partial z} \right) \\ \left(\frac{\partial \phi^{xx}}{\partial z} - \frac{\partial \phi^{xz}}{\partial x} \right) & \left(\frac{\partial \phi^{yx}}{\partial z} - \frac{\partial \phi^{yz}}{\partial x} \right) & \left(\frac{\partial \phi^{zx}}{\partial z} - \frac{\partial \phi^{zz}}{\partial x} \right) \\ \left(\frac{\partial \phi^{xy}}{\partial x} - \frac{\partial \phi^{xx}}{\partial y} \right) & \left(\frac{\partial \phi^{yy}}{\partial x} - \frac{\partial \phi^{yx}}{\partial y} \right) & \left(\frac{\partial \phi^{zy}}{\partial x} - \frac{\partial \phi^{zx}}{\partial y} \right) \end{bmatrix} \quad (5.56a)$$

$$= \begin{bmatrix} (a_{j10}^x - a_{j7}^x) & (a_{j10}^y - a_{j7}^y) & (a_{j10}^z - a_{j7}^z) \\ (a_{j3}^x - a_{j9}^x) & (a_{j3}^y - a_{j9}^y) & (a_{j3}^z - a_{j9}^z) \\ (a_{j5}^x - a_{j2}^x) & (a_{j5}^y - a_{j2}^y) & (a_{j5}^z - a_{j2}^z) \end{bmatrix} \quad (5.56b)$$

on j , obtained from equation (5.25), must be both constant and nonsymmetric; therefore, obtaining the maximum shear stress is not straightforward (see Section 5.2.2).

If the t^x , t^y and t^z values along each edge of element j are known, the internal forces on surfaces \overrightarrow{ABC} , \overrightarrow{ABD} , \overrightarrow{ACD} and \overrightarrow{BCD} can be determined using equation (5.45). For example, the internal forces on surface \overrightarrow{ABC} (assuming no external loads are applied to surface \overrightarrow{ABC}) can be calculated from:

$$\begin{bmatrix} F_{ABC}^x \\ F_{ABC}^y \\ F_{ABC}^z \end{bmatrix} = \begin{bmatrix} t_{AB}^x + t_{BC}^x - t_{AC}^x \\ t_{AB}^y + t_{BC}^y - t_{AC}^y \\ t_{AB}^z + t_{BC}^z - t_{AC}^z \end{bmatrix} \quad (5.57a)$$

$$= \begin{bmatrix} \int_A^B \boldsymbol{\Phi}^x \cdot d\mathbf{r} + \int_B^C \boldsymbol{\Phi}^x \cdot d\mathbf{r} - \int_A^C \boldsymbol{\Phi}^x \cdot d\mathbf{r} \\ \int_A^B \boldsymbol{\Phi}^y \cdot d\mathbf{r} + \int_B^C \boldsymbol{\Phi}^y \cdot d\mathbf{r} - \int_A^C \boldsymbol{\Phi}^y \cdot d\mathbf{r} \\ \int_A^B \boldsymbol{\Phi}^z \cdot d\mathbf{r} + \int_B^C \boldsymbol{\Phi}^z \cdot d\mathbf{r} - \int_A^C \boldsymbol{\Phi}^z \cdot d\mathbf{r} \end{bmatrix} \quad (5.57b)$$

Assuming $\boldsymbol{\Phi}^x$, $\boldsymbol{\Phi}^y$ and $\boldsymbol{\Phi}^z$ vary linearly (see equation (5.55)), F_{ABC}^x , F_{ABC}^y and F_{ABC}^z are functions of stress tensor $\boldsymbol{\sigma}_j$ and the vertex coordinates.

$$\begin{bmatrix} F_{ABC}^x \\ F_{ABC}^y \\ F_{ABC}^z \end{bmatrix} = \boldsymbol{\sigma}_j \mathbf{G}; \quad (5.58a)$$

where

$$\mathbf{G} = \frac{1}{2} \begin{bmatrix} (z_B - z_C) y_A + (z_C - z_A) y_B + (z_A - z_B) y_C \\ (z_C - z_B) x_A + (z_A - z_C) x_B + (z_B - z_A) x_C \\ (y_B - y_C) x_A + (y_C - y_A) x_B + (x_A - y_B) x_C \end{bmatrix}$$

is obtained from evaluating line integrals and F_{ABC}^x , F_{ABC}^y and F_{ABC}^z are known. Equations relating internal forces to vertex coordinates (*i.e.* similar to equation (5.58)) can be obtained for three remaining boundaries of element j , resulting in twelve equations (three per boundary) in nine unknowns (*i.e.* the components of $\boldsymbol{\sigma}_j$). Therefore $\boldsymbol{\sigma}_j$ can be determined uniquely, revealing that three equations must be linearly dependent. (Note that the thirty-six coefficients in equation (5.55) are normally not uniquely defined.)

The equilibrium or dual formulation of three-dimensional DLO is defined in terms of t^x , t^y and t^z values along specific edges. Assuming a mesh of κ tetrahedral elements, whose edges coincide with edges in an equivalent upper bound DLO analysis, the t^x , t^y and t^z values from the DLO analysis can be used to obtain $\boldsymbol{\sigma}_j$ for $j = 1, 2, \dots, \kappa$. Assuming the maximum shear stress τ_j^{max} on element j can be determined, a factor F_j on yield can be determined for each element j ($j = 1, 2, \dots, \kappa$) from equation (5.59), where yield is violated for any $F_j > 1$.

$$F_j = \frac{\tau_j^{max}}{c_j} \quad (5.59)$$

An overall factor

$$F = \max(\{F_1, F_2, \dots, F_\kappa\}) \quad (5.60)$$

on yield can also be obtained. Scaling all t^x , t^y and t^z values by F produces a new solution satisfying the yield condition everywhere and meeting the requirements for a pseudo lower bound solution. The pseudo lower bound adequacy factor $\lambda_l = \lambda/F$; where λ is the upper bound adequacy factor.

5.5 Numerical Example

In Section 3.3.1, upper bound solutions for the compression of a weightless cohesive block between two rough platens were obtained. In the following section, the performance of the pseudo lower bound method is evaluated using this benchmark problem. Exploiting symmetry (see Figure 3.3), t^x , t^y and t^z values were determined using the basic three-dimensional formulation in Chapter 3. All computations were performed on a 3.0GHz Intel Dual Core E8400 processor with 3.5GB RAM and running Windows XP. The pseudo lower bound method was implemented using MATLAB 7.3.0.

In the absence of a rigorous procedure to determine τ_j^{max} , the following iterative procedure was adopted to estimate τ_j^{max} on a given element j .

- (i) Express the normal \mathbf{n} to an arbitrary plane in terms of solid angles θ_1 and θ_2 in Figure 5.9:

$$\mathbf{n} = \frac{1}{\sqrt{\cos^2 \theta_2 - \cos^2 \theta_2 \cos^2 \theta_1 + \cos^2 \theta_1}} \begin{bmatrix} \cos \theta_2 \sin \theta_1 \\ \sin \theta_2 \cos \theta_1 \\ -\cos \theta_2 \sin \theta_1 \end{bmatrix} \quad (5.61)$$

- (ii) Set $\tau_j^{max} = 0$, $\theta_1^{max} = 0$ and $\theta_2^{max} = 0$.
- (iii) Using equation (5.9), find τ for all combinations of $\theta_1 = \{-90, -89, -88, \dots, 0, \dots, 89, 90\}$ and $\theta_2 = \{-89, -88, -87, \dots, 0, \dots, 88, 89\}$. For all combinations, if $\tau > \tau_j^{max}$ then $\tau_j^{max} = \tau$, $\theta_1^{max} = \theta_1$ and $\theta_2^{max} = \theta_2$.
- (iv) Refine τ_j^{max} by finding the local maximum, satisfying $\frac{\partial \tau_j}{\partial \theta_1} = 0$ and $\frac{\partial \tau_j}{\partial \theta_2} = 0$, in the vicinity of θ_1^{max} and θ_2^{max} .

Pseudo lower bounds were obtained for two mesh types.

- (i) Mesh A – arbitrarily splits the cubes formed by neighbouring nodes into six tetrahedral elements.

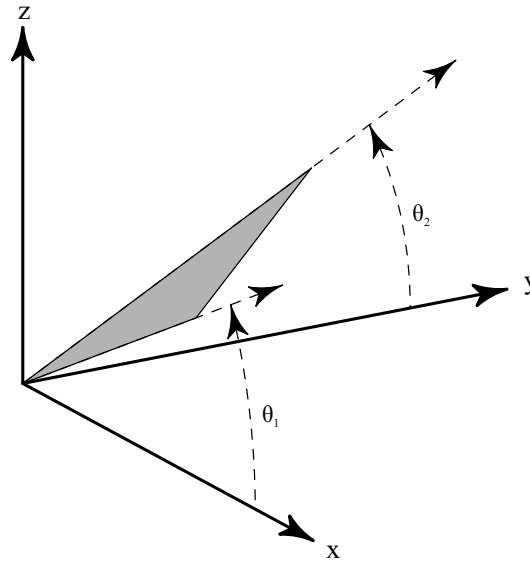


FIGURE 5.9: Solid angles θ_1 and θ_2 describing the inclination of an arbitrary plane with respect to the xy plane

- (ii) Mesh B – splits the individual solids forming the upper bound mechanism (and identified in the equivalent upper bound analysis) into tetrahedral elements. The vertices of these element must be vertices of the solids forming the mechanism. In some cases, the edges of the solids in the mechanism were not included in the original upper bound analysis. After adding of these missing edges and splitting any active discontinuities traversed by these edges, the upper bound analysis was repeated to obtain the missing t^x , t^y and t^z values.

5.5.1 Results

Pseudo lower bound results for the compression of a weightless cohesive block between two rough platens are present in Table 5.1. For the largest nodal grid considered, the solids forming the upper bound mechanism were not available due to limitations in the algorithm used to identify these.

TABLE 5.1: Compression of a block – pseudo lower bounds

Spacings*	upper bound*		pseudo lower bound			
	q/c	diff. † (%)	mesh A q/c	diff. ‡ (%)	mesh B q/c	diff. ‡ (%)
$1/2$	2.321	0.74	0.819	63	1.425	36
$1/2$	2.319(2.316 [◊])	0.65(0.52 [◊])	0.636	69	1.390	38
$1/6$	2.314	0.43	0.574	75	n/a	n/a

Key: $\Delta = \Delta x = \Delta y = \Delta z$ (see Figure 3.3); *from three-dimensional DLO; †relative to best upper bound from Chapter 3; ◊improved result after solid identification; ‡relative to best published lower bounds (see Table 2.4).

5.5.2 Discussion

- (i) The pseudo lower bound errors are much greater than the equivalent upper bound errors. As with method I described in Chapter 4, t^x , t^y and t^z values along the edges are determined from an upper bound analysis and are therefore not optimal for a pseudo lower bound analysis, at least partially explaining the poor results.
- (ii) A global optimization problem (or a three-dimensional equivalent to method II in Chapter 4) which automatically identifies the best pseudo lower bound for a given mesh was not considered practical as equation (5.9) and, consequently, the yield condition is non-convex for nonsymmetric tensors.

5.6 Conclusion

- (i) The equilibrium discontinuity layout optimization (DLO) formulation for three-dimensional problems has been derived using translational stress functions and vector calculus. It has been shown that the derivation allows a deeper understanding of the equilibrium formulation to be obtained. In particular, it has been shown that line integrals of the translational stress

functions Φ^x , Φ^y and Φ^z along the edges are used to obtain the internal forces on the discontinuities.

- (ii) Translational stress functions have been used to derive a relaxed, pseudo lower bound formulation. Linear variation of the stress functions Φ^x , Φ^y and Φ^z is assumed across tetrahedral constant stress elements, used to discretize the problem domain. t^x , t^y and t^z values from an upper bound analysis are used to find the stresses on these elements, and these stresses were then scaled to obtain a pseudo lower bound solution.
- (iii) However, the pseudo lower bound solutions obtained were found to be much poorer than corresponding upper bound solutions. This is at least partly explained by the fact that the t^x , t^y and t^z values along the edges were determined from an upper bound analysis.

6 Discussion

6.1 Introduction

DLO is a flexible, intuitive tool capable of considering complex problems; where the failure mechanism is not known beforehand (as illustrated by the pipeline and berm problem in Figure 1.2). Plane strain DLO is capable of obtaining accurate solutions at moderate computational expense. For example, solutions to the Prandtl problem obtained using LimitState:GEO 3.0 (LimitState, 2012), a commercial software implementation of DLO, are presented in Table 6.1. Solutions within 1% of the ‘exact’ solution, accurate enough for most engineering applications, are obtained in less than 4 seconds using a desktop computer with a 3.0 GHz Intel processor and running Windows XP.

TABLE 6.1: Prandtl punch problem – LimitState:GEO 3.0 results (using symmetry about the punch centerline)

Nodes no.	Discontinuities no.	N_c	Error %	Time s
224	18,732	5.194	1.02	1.42
483	81,826	5.175	0.642	3.02
949	298,258	5.158	0.323	9.63
1,898	1,075,576	5.155	0.255	49.6
3,962	3,785,468	5.151	0.173	335

In Chapter 3, a three-dimensional, kinematic formulation of the DLO procedure for translational problems was successfully developed. The new formulation is able to directly identify the discontinuities developing at failure and is posed entirely in

terms of potential discontinuities. These potential discontinuities are not restricted to the boundaries of predefined solid regions as in rigid finite element (RFEM) or finite element limit analysis (FELA); thus stress or strain singularities can be dealt with naturally without any need for special treatment. The formulation's ability to handle stress singularities has been demonstrated by the punch indentation example, considered in Section 3.3.2, and represents an important advantage as such singularities are commonly encountered. Volumetric locking is also avoided without need for special treatment. Furthermore, three-dimensional DLO is able to strictly enforce the associated Mohr-Coulomb flow rule using efficient SOCP; unlike three-dimensional FELA requiring more complex SDP.

Using the basic fully connected formulation, good correlation was found with benchmarks available in the literature. However, only relatively small nodal grids were considered due the rapid increase in the total number m_{all} of discontinuities with the number n of nodes. Assuming triangular discontinuities, the maximum number of potential discontinuities $m_{up} = n(n-1)(n-2)/6$ (cf. $m_{up} = n(n-1)/2$ for plane strain problems). Figure 6.1 compares the maximum number of discontinuities m_{up} for by the basic plane strain and three-dimensional formulations. In plane strain, accurate solutions require discretizations involving perhaps millions of potential discontinuities (Smith and Gilbert, 2007). In the three-dimensional formulation, m_{up} grows much more rapidly with n . Additionally, more nodes are, typically, required to discretize a three-dimensional problem. Therefore, the number of discontinuities required to obtain highly accurate solutions is likely to be much larger.

Direct solution of the resulting large SOCP problems is impractical. In fact, even direct solution of the resulting linear programming (LP) problem in the basic plane strain formulation quickly becomes impractical with increasing n . However, Smith and Gilbert (2007) observe that displacement typically only occurs on a small proportion of discontinuities, referred to as active discontinuities. Therefore, an identical solution can be obtained using only the active discontinuities thus significantly reducing the size of the resulting LP problem. A similar trend was observed in the three-dimensional examples even at the low nodal resolutions

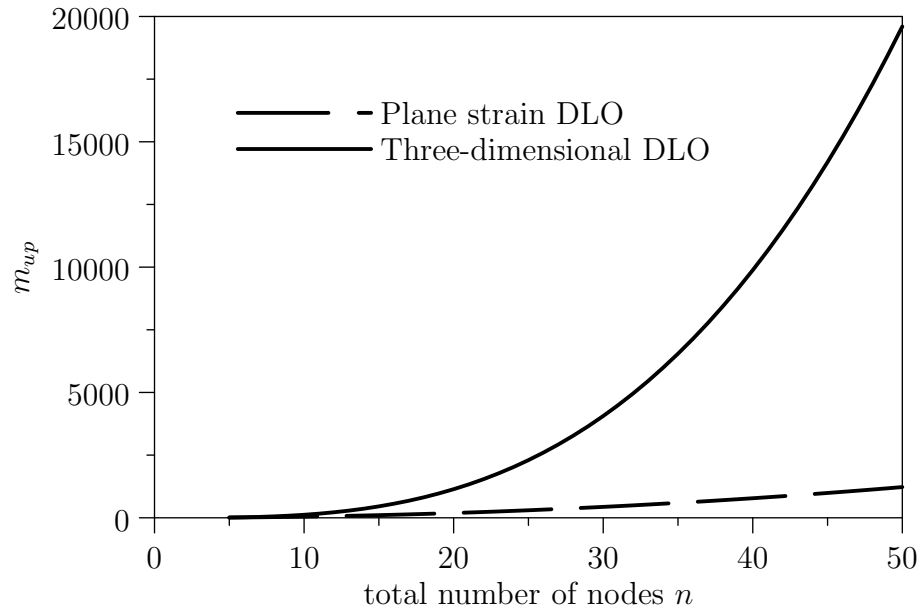


FIGURE 6.1: Maximum number of potential discontinuities m_{up} in basic plane strain and three-dimensional DLO formulations

considered. Furthermore, the proportion of active discontinuities was observed to reduce with increasing problem size.

In plane strain, Smith and Gilbert (2007) use this observation to develop an adaptive nodal connection scheme (see Section 2.6.3.1). The adaptive nodal connection scheme allows a subset of the total discontinuities, containing the critical set of active discontinuities, to be definitely identified without solving the basic fully connected problem directly. The subset identified will typically contain a number of nonactive discontinuities in addition to the active discontinuities, but remains a small proportion of the total. Smith and Gilbert (2007) have successfully used this adaptive scheme to solve problem involving millions of potential discontinuities. The proportion of active discontinuities in the three-dimensional formulation is similarly small suggesting an analogous scheme might be successful.

Understanding the plane strain dual, equilibrium formulation of DLO is central to the adaptive nodal connection scheme. Similarly, understanding the dual formulation is essential to developing an analogous three-dimensional scheme. Consequently, the plane strain and three-dimensional equilibrium formulations have been

derived from first principles in Chapters 4 and 5, respectively. These derivations have allowed a deeper understanding of the dual plane strain and three-dimensional formulations.

6.2 Equilibrium formulation of DLO and adaptive procedures

The plane strain and three-dimensional equilibrium formulations are given in Sections 5.3.6 and 2.6.3, respectively. Initial examination of these formulations reveals important similarities: an objective function maximizing a multiplier on the live load, constraints enforcing equilibrium and yield conditions. The internal forces $\tilde{\mathbf{q}}_i$ on a discontinuity i not contained in the original LP or SOCP problem can be found by rearranging the equilibrium constraint

$$\tilde{\mathbf{q}}_i = \lambda \mathbf{f}_{Li} + \mathbf{f}_{Di} + \mathbf{B}_i^T \mathbf{t}_i; \quad (6.1)$$

where \mathbf{f}_{Li} and \mathbf{f}_{Di} are the dead and live loads, respectively, on discontinuity i ; and \mathbf{B}_i contains the columns of global compatibility matrix \mathbf{B} corresponding to the displacement jumps across discontinuity i . An important distinction, however, is found upon examining the respective definitions of vector \mathbf{t}_i in the plane strain and three-dimensional formulations. In the plane strain formulation, \mathbf{t}_i contains values of scalar, translational stress functions t^x and t^y at the vertices of linear discontinuity i . In the three-dimensional formulation, \mathbf{t}_i now contains line integrals of vector, translational stress functions Φ^x , Φ^y and Φ^z along the edges of polygonal discontinuity i . Equivalently in the primal kinematic formulations, compatibility is enforced at the nodes and along the edges in the plane strain and three-dimensional formulations, respectively.

The plane strain adaptive nodal connection procedure, described in Section 2.6.3.1, uses the internal forces $\tilde{\mathbf{q}}_i$ determined from equation (6.1) to check the yield condition on potential discontinuities not included in the LP problem. t^x and t^y values

at every node must be available to allow determination of $\tilde{\mathbf{q}}_i$ values for all discontinuities i in the basic fully connected problem. Therefore, at least one discontinuity per node is necessary to guarantee a rigorous solution to the basic fully connected problem using the adaptive nodal connection procedure. Generally, it is necessary to include more than one discontinuity per node to ensure rapid convergence towards the final solution.

In the three-dimensional formulation, edges are connected to create polygonal discontinuities. The internal forces $\tilde{\mathbf{q}}_i$ on polygonal discontinuities not included in the SOCP problem can be calculated using equation (6.1) and t^x, t^y, t^z values attached to the edges. Therefore, an adaptive scheme, termed adaptive edge connection, analogous to adaptive nodal connection is possible for the three-dimensional formulation. The steps involved in this procedure are essentially the same, but existing t values along the edges are connected to find the internal forces on discontinuities not included in the SOCP problem. A rigorous solution using adaptive edge connection requires that line integrals t_j^x, t_j^y and t_j^z at every edge $j(j = 1, 2, \dots, l)$ must be available to allow determination of $\tilde{\mathbf{q}}_i$ for all discontinuities $i(i = 1, 2, \dots, m_{all})$; where l is the total number of edges used to discretize the problem. Therefore, at least one discontinuity at every edge must be included in the original SOCP problem. The maximum number of edges $l_{up} = n(n - 1)/2$. (Note l_{up} equals m_{up} for a plane strain problem with same number of nodes n .) Therefore, the size of the initial SOCP problem required for a rigorous solution quickly becomes impractical with increasing n . Generally, it is necessary to include more discontinuities to achieve rapid convergence towards the final solution. Initial studies have been undertaken using adaptive edge connection. These reveal that determining an initial subset balancing subset size against speed of convergence to be extremely challenging. In conclusion, the reductions in problem size achieved from adaptive edge connection are insufficient to allow highly accurate solutions. However, adaptive edge connection may be used in conjunction with other adaptive or decomposition procedures.

6.3 Potential enhancements

6.3.1 Introduction

The rapid increase in the number of discontinuities with the number of nodes calls for enhancements to the three-dimensional DLO procedure. These enhancements are needed to allow solution of larger problems, obtaining more accurate solutions. For the problems considered in Chapter 3, the stability and runtime of the SOCP optimizer limited the size of problem that could be considered. Therefore, the enhancements discussed in the following sections concentrate on either reducing the size of the problem passed to the optimizer or improving the performance of the optimizer. It is thought that the former approach has the greater potential to deliver improved performance.

6.3.2 Improving optimizer performance

For analyses larger than those reported in Chapter 3, the SOCP solver, MOSEK v. 6 (Mosek, 2011), terminated before converging, due to slow progress. Furthermore although the constraint matrix A generated is sparse, Cholesky decomposition of matrix AA^T during optimization resulted in considerable infill. However, SOCP is a rapidly developing field and further developments and/or better conditioning of A may deliver improved robustness. Gurobi v. 5 (Gurobi, 2012), for example, has recently been extended to include SOCP capability. Comparison of Gurobi v. 5 and MOSEK v. 6 for a LP slab problem suggests Gurobi v. 5 to be the more efficient algorithm (see Figure 6.2); while performance at low nodal resolutions is comparable, for larger problems MOSEK v. 6 runtimes vary hugely and are consistently longer than Gurobi v. 5 runtimes. Therefore, a similar study that in Figure 6.2 is recommended to compare the performance of the two solvers for three-dimensional DLO problems.

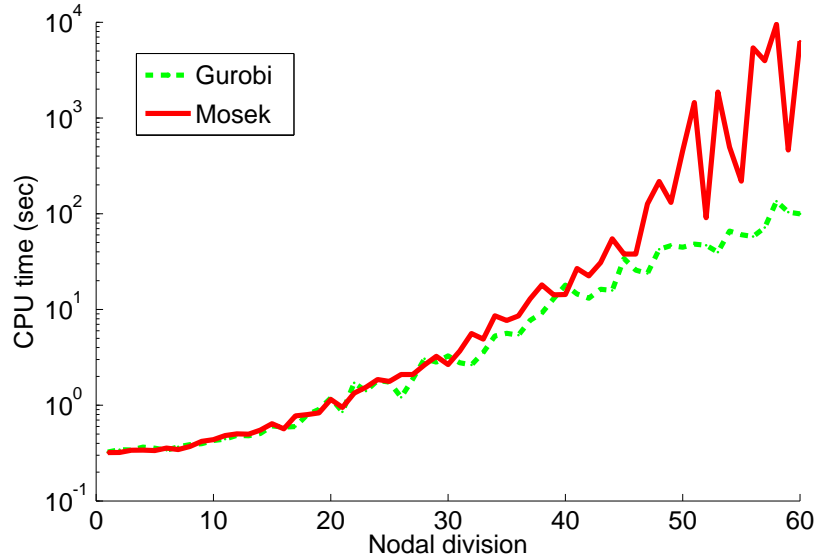


FIGURE 6.2: MOSEK v. 6 and Gurobi v. 5 performance for a linear programming slab problem (courtesy of Linwei He)

6.3.3 Alternative adaptive procedures

For the adaptive edge connection procedure described in Section 6.2, it is necessary to include at least one discontinuity at every edge in the initial iteration. Therefore, the solution of the initial optimization problem becomes impractical for even moderately sized nodal grids. However, other adaptive procedures are possible. As with adaptive edge connection, a solution based on an initial subset of discontinuities is determined. Discontinuities missing from the initial subset are then added to the subset based on specific criteria. An optimization problem based on the updated subset is then solved and the procedure repeated. If the criteria for adaptive procedure are no longer based on the t^x , t^y and t^z values, the initial subset may no longer be required to include a discontinuity at every edge. For example, the geometry of the critical failure mechanism from previous iterations may be used to grow the initial subset from one iteration to the next. The aim of these criteria is to add only those discontinuities which will result in an improved solution. However, these methods no longer guarantee that the global optimum is found for a particular nodal grid.

6.3.4 Decomposition

By splitting the problem domain into overlapping regions, a decompositional approach similar to that of Pastor et al. (2009) and Kammoun et al. (2010) could be developed (see Section 2.5.3). A potential decompositional procedure for DLO is illustrated in Figure 6.3 using a plane strain example and three overlapping regions but could equally be used with an arbitrary number of regions. (Note that the procedure is framed in terms of the equilibrium formulation and hence maximizes the load). The steps in a similar three-dimensional procedure would be identical except t^x , t^y and t^z values along the edges must now be fixed. Decompositional procedures are ideal for exploiting parallel processing. To facilitate parallel maximization of loads on regions I and II, discontinuities crossing the boundary between regions I and II are not permitted, as illustrated in Figure 6.3(d). Therefore, some of the flexibility inherent in the DLO procedure will be lost. However, this may not be significant if sufficiently large regions are employed. This decompositional procedure could allow larger problems to be considered. However, it cannot be guaranteed to converge towards the basic DLO solution for the nodal grid.

Numerous variations on the decompositional procedure described above can be envisioned. For example, the decompositional procedure described below using the plane strain example in Figure 6.4 .

- (i) Discretize the problem domain using a nodal grid and connecting discontinuities (see Figure 6.4(a)).
- (ii) Split discontinuities into a master subset (see Figure 6.4(b)), two slave subsets (see Figures 6.4(c) and 6.4(d)) and a subset containing the remaining discontinuities (see Figure 6.4(e)). The master and slave subsets must contain discontinuities joining every node.
- (iii) Use the equilibrium formulation to maximize the load on the master subset.
- (iv) Fix the t^x and t^y values on nodes in mater nodal subset ●.

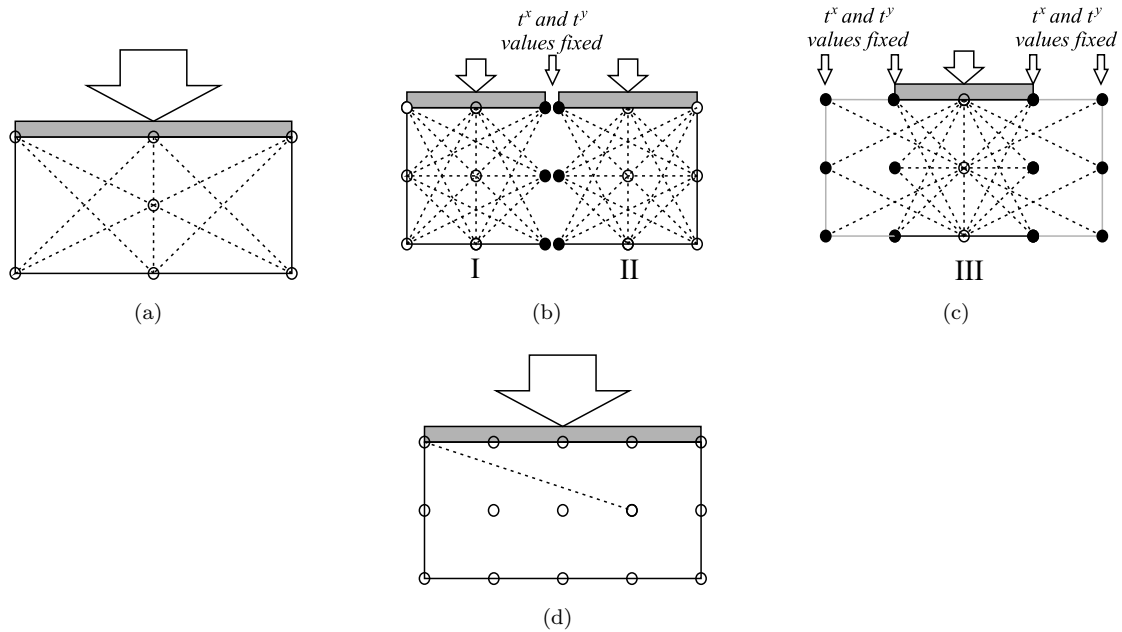


FIGURE 6.3: Plane strain example of decompositional procedure using overlapping regions: (a) solve small initial problem; (b) fix t^x and t^y values on boundary between regions I and II; maximize loads on regions I and II; (c) fix t^x and t^y values from (b) on boundary and outside of region III; maximize load on region III; repeat steps (b)-(c) or terminate. (d) example of a prohibited discontinuity crossing boundary between regions I and II.

- (v) Minimize the maximum violation on the slave subsets by varying the t^x and t^y values on nodal subsets \diamond and \square , respectively. These two operations could be done in parallel thus reducing runtime.
- (vi) Use the t^x and t^y values from (iii) and (v) to determined the maximum violation on the remain discontinuities (see Figure 6.4(e)).
- (vii) Transfer the most violating discontinuities from (v) and (vi) to the master subset (see Figure 6.4(f)). Removing any overlapping discontinuities.
- (viii) Transfer the vertices of discontinuities added to the master subset in (vii) from \diamond and \square to \bullet (see Figure 6.4(f)).
- (ix) Repeat from (iii) or terminate.

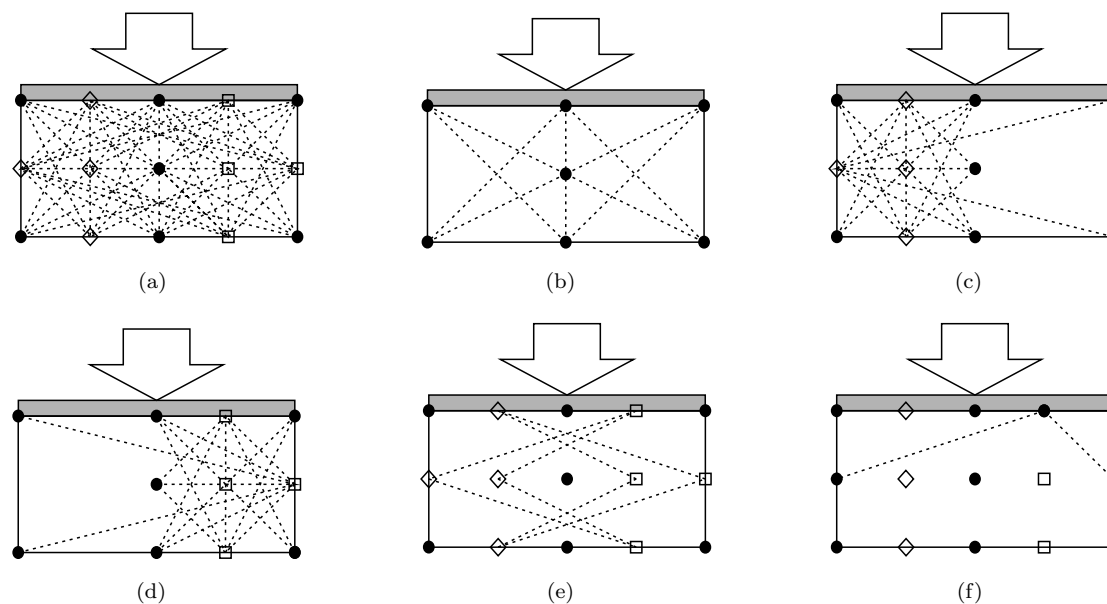


FIGURE 6.4: Plane strain example of decompositional procedure using master and slave subsets. (a) Discretize problem domain using nodes and discontinuities. (b-d) Split discontinuities into (b) a master subset, (c) and (d) slave subsets and (e) a subset containing the remaining discontinuities. Solve optimization problems based on master and slave subsets to determine t^x and t^y values at the nodes. (f) Transfer most violating discontinuities and corresponding vertices to the master subset and master nodal subset \bullet , respectively.

In the decompositional procedure described above, the slave subsets need not be constrained to a particular region but rather must join specific nodal subsets, such as \circ or \diamond in the example. Additionally, the slave subsets must link the nodal subsets to the master subset. The procedure described resembles adaptive nodal connection except the t^x and t^y values are determined by an alternative strategy. It may, therefore, be possible to prove convergence to the basic DLO solution for the nodal grid. A three-dimensional version of the procedure would use subsets of discontinuities joining subsets of edges.

It is recommended that the decompositional procedures described in this section be investigated in plane strain before proceeding to implement these in three-dimensions.

6.4 Pseudo lower bounds

In Chapters 4 and 5, relaxed, pseudo lower bound methods were developed for plane strain and three-dimensional problems, respectively. The aim was to develop lower bound type formulations incorporating the advantages of DLO. However, unlike DLO, discontinua were only permitted at the boundary between pre-defined solid regions (*i.e.* very similar to RFEM). Consequently, mesh sensitivity was observed to varying degrees for all three pseudo lower bound methods. Furthermore, the yield condition must be satisfied everywhere and not just along specific planes. Therefore, more complex algorithms are necessary (compared to upper bound discontinuous methods) to directly optimize t values (at the nodes or edges) for pseudo lower bound analysis. In plane strain, method II resulted in a SOCP rather than a LP problem. The three-dimensional equivalent to method II results in a complex non-convex, optimization problem and was, consequently, not developed further.

The possibility of automatically refining a DLO grid, based on an equivalent pseudo lower bound solution, to obtain an improved upper bound naturally arises. However, pseudo lower bounds for the examples considered compare poorly to equivalent DLO results. It is, therefore, the author's opinion that pseudo lower bounds are poor guides for nodal refinement. However, they can provide a valuable lower bound estimate on the best purely translational upper bound.

6.5 Rotations

The formulation developed in Chapter 3 does not consider rotations. This can be an important limitation for certain classes of problems. In plane strain DLO, rotations have been incorporated by including circular arcs or log spirals among the potential discontinuities (Gilbert et al., 2010a; Smith, 2012). A similar approach may be possible for including rotations in the three-dimensional formulation using non-planar discontinuities.

7 Conclusions and future work

7.1 Introduction

In this chapter, the key conclusions of this thesis are summarized and directions for future work suggested.

7.2 Conclusions

- (i) A new three-dimensional discontinuity layout optimization (DLO) formulation has been described that can be used to solve general three-dimensional plasticity problems. The upper bound formulation makes use of efficient second order cone programming (SOCP) to handle the Mohr-Coulomb flow rule and to directly determine optimal translational collapse mechanisms. These collapse mechanisms are based on an optimal subset of planar discontinuities drawn from a large set of potential polygonal discontinuities whose vertices are located on nodes within a three-dimensional grid of nodal points.
- (ii) The new three-dimensional formulation was validated against benchmarks available in the literature. Good correlation was found despite the low nodal resolutions employed. The best reported upper bound for the compression of a purely cohesive block between two perfectly rough platens was improved upon.

- (iii) In all the cases considered using the basic three-dimensional formulation, the percentage of active discontinuities in the critical mechanism was small; active discontinuities are defined as those discontinuities on which an actual jump in displacement occurs. This suggests an adaptive iterative procedure may be effective if it can identify these discontinuities and add them to an initial small subset of discontinuities; while keeping non-active discontinuities in the optimization to a minimum.
- (iv) The dual, equilibrium formulation of plane strain DLO has been derived from first principles making use of translational stress functions and vector calculus, allowing a deeper insight into the nature of DLO solutions. Importantly, the dual formulation allows the total internal forces on discontinuities to be determined. In the dual, these forces are determined from scalar values of stress functions at the nodes. In previous work, the dual formulation had been derived from duality principles.
- (v) The dual, equilibrium formulation of three-dimensional DLO has also been derived from first principles making use of translational stress functions and vector calculus, revealing important differences with plain strain DLO. Unlike plane strain DLO, the line integrals of vector, stress functions along the edges are used to determine the total internal forces on the potential discontinuities.
- (vi) Preliminary investigation of an adaptive scheme, termed adaptive edge connection, for three-dimensional DLO has been undertaken. The adaptive scheme relies on line integrals of stress functions along the edges, determined from an original optimization problem. Therefore, discontinuities must be included at every edge in the original optimization problem, in order to allow the line integrals to be determined along every edge. It was found that the number of edges grows rapidly with the number of nodes. Consequently, it was found that the original optimization quickly becomes impractical with increasing problem size.

- (vii) Plane strain and three-dimensional relaxed lower bound methods, ignoring rotational equilibrium, have been developed using translational stress functions. Unlike in DLO, the yield condition is exactly satisfied everywhere within the problem domain. Therefore, these lower bounds can provide a bound on the best translational upper bound. However, results were less accurate than equivalent upper bounds obtained using DLO. Mesh sensitivity was also observed in the numerical examples due to stress discontinuities only being permitted at the boundaries of predefined solid regions.

7.3 Suggestions for future work

A new three-dimensional formulation of the DLO procedure for translational problems has been successfully developed. The new formulation is widely applicable and handles stress singularities without any need for special treatment. However, it is only practical to determine the collapse loads for relatively small nodal grids due to the rapid increase in the number of discontinuities with the number of nodes. The robustness and long runtimes of the optimizer were found to be limiting factors. Therefore, future work should focus on improving the optimizer performance and/or reducing the size of problem passed to the optimizer. The following are recommended for future consideration.

- (i) Improvements to the structure and conditioning of the constraint matrix passed to the optimizer.
- (ii) Investigate the performance of available SOCP optimizers including Gurobi v. 5.
- (iii) Decompositional procedures that split the problem into smaller subproblems. Decomposition allows the problem to be considered as a series of smaller optimization problems rather than a single larger optimization problem. These smaller problems can be solved in parallel using powerful parallel processing technologies.

Additionally, rotations could be incorporated into the formulation by including non-planar discontinuities. These would extend the applicability of the new procedure to rotational problems but would not enhance computational efficiency.

References

- Alwis, W. (2000), “Discrete element slip model of plasticity”, *Eng. Struct.* , Vol. 23, pp. 1494–1504.
- Antão, A., Vicente da Silva, M., Guerra, N. and Delgado, R. (2012), “An upper bound-based solution for the shape factors of bearing capacity of footings under drained conditions using a parallelized mixed f.e. formulation with quadratic velocity fields”, *Comput. Geotech.* , Vol. 41, pp. 5788–5804.
- Belytschko, T., Lu, Y. and Gu, L. (1994), “Element-free Galerkin methods”, *Int. J. Numer. Methods Eng.* , Vol. 37, pp. 229–256.
- Borges, L., Zouain, N., Costa, C. and Feijóo, R. (2001), “An adaptive approach to limit analysis”, *Int. J. Solids Struct.* , Vol. 38, pp. 1707–1720.
- Bottero, A., Negre, R., Pastor, J. and Turgeman, S. (1980), “Finite element method and limit analysis theory for soil mechanics problems”, *Comput. Methods Appl. Mech. Eng.* , Vol. 22.
- Boyd, S. and Vandenberghe, L. (2004), *Convex Optimization*, Cambridge University Press, Cambridge.
- Capsoni, A. and Corradi, L. (1997), “A finite element formulation of the rigid-plastic limit analysis problem”, *Int. J. Numer. Methods Eng.* , Vol. 40, pp. 2063–2086.
- Casciaro, R. and Cascini, L. (1982), “A mixed formulation and mixed finite elements for limit analysis”, *Int. J. Numer. Methods Eng.* , Vol. 18, pp. 211–243.

- Chakrabarty, J. (2006), *The theory of plasticity*, 3rd edn, Oxford, UK: Butterworth-Heinemann.
- Chen, J., Yin, J. and Lee, C. (2003), “Upper bound limit analysis of slope stability using rigid elements and nonlinear programming”, *Can. Geotech. J.* , Vol. 40, pp. 472–752.
- Chen, W. (1975), *Limit Analysis and Soil Plasticity. Developments in Geotechnical Engineering*, Vol. 7, Amsterdam, The Netherlands: Elsevier.
- Chou, P. C. and Pagano, N. (1967), *Elasticity: tensor, dyadic and engineering approaches*, London, UK: D. Van Nostrand Co.
- Christiansen, E. (1981), “Computations of limit loads”, *Int. J. Numer. Methods Eng.* , Vol. 17, pp. 1547–1570.
- Christiansen, E. and Pedersen, O. S. (2001), “Automatic mesh refinement in limit analysis”, *Int. J. Numer. Methods Eng.* , Vol. 50, pp. 1331–1346.
- Clarke, S. (2009), *Enhancement of the BRICK constitutive model to incorporate viscous soil behaviour*, PhD Thesis, The University of Sheffield.
- Coelho, S. and C., P. (2008), “Mohr-cyclides, a 3d representation of geological tensors: The examples of stress and flow”, *J. Struct. Geol.* , Vol. 30, pp. 580–601.
- Coulomb, C. (1776), “Essai sur une application des regles des maximis et minimis a quelques problemes de statique relatifs a l’architecture.”, *Memoires de l’Academie Royale pres Divers Savants* , Vol. 7.
- de Figueiredo, R., Vargas, E. and Moraes, A. (2004), “Analysis of bookshelf mechanisms using the mechanics of Cosserat generalized continua”, *J. Struct. Geol.* , Vol. 26, pp. 1931–1943.
- Drucker, D., Greenberg, H. and Prager, W. (1952), “Extended limit design theorems for continuous media”, *Quart. Appl. Math.* , Vol. 9, pp. 381–389.

- Gilbert, M., Smith, C., Haslam, I. and Pritchard, T. (2010b), Application of discontinuity layout optimization to geotechnical limit analysis problems, *in* ‘Proc. 7th European Confer. Numeri. Methods Geotech. Eng., Trondheim, Norway’, pp. 169–174.
- Gilbert, M., Smith, C. and Pritchard, T. (2010a), “Masonry arch analysis using discontinuity layout optimization”, *Proc. Inst. Civ. Eng.: Eng. Comput. Mech.*, Vol. 163, pp. 155–166.
- Gilbert, M. and Tyas, A. (2003), “Layout optimization of large-scale pin-jointed frames”, *Eng. Comput.*, Vol. 20, pp. 1044–1064.
- Gurobi (2012), *Gurobi optimizer reference manual, Version 5.0. See www.gurobi.com.*
- Hill, R. (1950), *The mathematical theory of plasticity*, Oxford, UK: Clarendon Press.
- Iordache, M. and Willam, K. (1998), “Localized failure analysis in elastoplastic cosserat continua”, *Comput. Methods Appl. Mech. Eng.*, Vol. 151, pp. 559–586.
- James, G. (1999), *Advanced modern engineering mathematics*, 2nd edn, London, UK: Prentice Hall.
- Kammoun, Z., Pastor, F., Smaoui, H. and Pastor, J. (2010), “Large static problem in numerical limit analysis: A decompositional approach”, *Int. J. Numer. Anal. Methods Geomech.*, Vol. 34, pp. 1960–1980.
- Kelley, J. E. J. (1960), “The cutting-plane method for solving convex programs”, *J. Soc. Ind. Appl. Math.*, Vol. 8, pp. 703–712.
- Koopman, D. C. A. and Lance, R. (1965), “On linear programming and plastic limit”, *J. Mech. Phys. Solids*, Vol. 13, pp. 77–87.
- Krabbenhøft, K. and Damkilde, L. (2000), Limit analysis based on lower-bound solutions and nonlinear yield criteria., *in* B. Topping, ed., ‘Finite Elements: Techniques and developments’, Edinburgh, UK: CIVIL-COMP Ltd., pp. 117–129.

- Krabbenhøft, K. and Damkilde, L. (2003), “A general non-linear optimization algorithm for lower bound limit analysis”, *Int. J. Numer. Methods Eng.*, Vol. 56, pp. 165–184.
- Krabbenhøft, K., Lyamin, A. and Sloan, S. (2008), “Three-dimensional Mohr-Coulomb limit analysis using semidefinite programming”, *Commun. Numer. Methods Eng.*, Vol. 24, pp. 1107–1119.
- Krabbenhøft, K., Lyamin, A. and Sloan, S. (2007), “Formulation and solution of some plasticity problems as conic programs”, *Int. J. Solids Struct.*, Vol. 44, p. 15331549.
- Le, C., Askes, H. and Gilbert, M. (2012), “A locking-free stabilized kinematic EFG model for plane strain limit analysis”, *Comput. Struct.*, Vol. 106-107, pp. 1–8.
- Le, C. V. (2009), *Novel numerical procedures for limit analysis of structures: mesh-free methods and mathematical programming*, PhD Thesis, The University of Sheffield.
- Lee, C. and Kobayashi, S. (1973), “New solutions to rigid-plastic deformation problems using a matrix method”, *Trans. ASME, J. Eng. Ind.*, Vol. 95, pp. 865–873.
- Li, A., Merifield, R. and Lyamin, A. (2009), “Limit analysis solutions for three dimensional undrained slopes”, *Comput. Geotech.*, Vol. 36, pp. 1330–1351.
- LimitState (2012), “LimitState:GEO. see <http://www.limitstate.com/>”.
- Lyamin, A., Salgado, R., Sloan, S. and Prezzi, M. (2007), “Two- and three-dimensional bearing capacity of footings in sand”, *Géotechnique*, Vol. 57, pp. 647–662.
- Lyamin, A. and Sloan, S. (2002a), “Lower bound limit analysis using non-linear programming”, *Int. J. Numer. Methods Eng.*, Vol. 55, pp. 573–611.
- Lyamin, A. and Sloan, S. (2002b), “Upper bound limit analysis using linear finite elements and non-linear programming”, *Int. J. Numer. Anal. Methods Geomech.*, Vol. 29, pp. 181–216.

- Lyamin, A., SW, S., Krabbenhøft, K. and Hijiaj (2005), “Lower bound limit analysis with adaptive remeshing”, *Int. J. Numer. Methods Eng.* , Vol. 63(14).
- Lysmer, J. (1970), “Limit analysis of plane problems in soil mechanics”, *J. Soil Mech. Found. Div. ASCE* , Vol. 96, pp. 1311–1334.
- Makrodimopoulos, A. (2010), “Remarks on some conic yield restrictions in limit analysis”, *Int. J. Numer. Meth. Biomed. Eng.* , Vol. 26, pp. 1449–1461.
- Makrodimopoulos, A. and Martin, C. (2008), “Upper bound limit analysis using discontinuous quadratic displacement fields”, *Commun. Numer. Methods Eng.* , Vol. 24, pp. 911–927.
- Makrodimopoulos, A. and Martin, C. M. (2006), “Lower bound limit analysis of cohesive-frictional materials using second-order cone programming”, *Int. J. Numer. Methods Eng.* , p. 604634.
- Makrodimopoulos, A. and Martin, C. M. (2007), “Upper bound limit analysis using simplex strain elements and second-order cone programming”, *Int. J. Numer. Anal. Methods Geomech.* , Vol. 2007, pp. 835–865.
- Martin, C. (2011), “The use of adaptive finite-element limit analysis to reveal slip-line fields”, *Géotechnique Lett.* , Vol. 1, pp. 23–29.
- Martin, C. and Makrodimopoulos, A. (2008), “Finite-element limit analysis of Mohr-Coulomb materials in 3D using semidefinite programming”, *J. Eng. Mech. ASCE* , Vol. 134, pp. 339–347.
- Merifield, R., Lyamin, A. and Sloan, S. (2006), “Three dimensional lower-bound solutions for the stability of plate anchors in sand”, *Géotechnique* , Vol. 56, pp. 123–132.
- Merifield, R., Lyamin, A., Sloan, S. and Yu, H. (2003), “Three-dimensional lower bound solutions for stability of plate anchors in clay”, *J. Geotech. Geoenvironmental Eng. ASCE* , Vol. 129, pp. 243–253.
- Michalowski, R. (2001), “Upper-bound load estimates on square and rectangular footings”, *Géotechnique* , Vol. 51, pp. 787–798.

- Michalowski, R. (2010), “Limit analysis and stability charts for 3D slope failures”, *J. Geotech. Geoenviron. ASCE*, Vol. 136, pp. 583–593.
- Michalowski, R. and Drescher, A. (2009), “Three-dimensional stability of slopes and excavations”, *Géotechnique*, Vol. 59, pp. 839–850.
- Mosek (2011), *The MOSEK optimization tools manual*. See <http://www.mosek.com>, version 6.0 (revision 119), Mosek ApS.
- Muñoz, J., Bonet, J., Huerta, A. and Peraire, J. (2009), “Upper and lower bounds in limit analysis: Adaptive meshing strategies and discontinuous loading”, *Int. J. Numer. Methods Eng.*, Vol. 77, pp. 471–501.
- Murray, E. and Geddes, J. (1987), “Uplift of anchor plates in sand”, *J. Geotech. Eng. ASCE*, Vol. 113, pp. 202–215.
- Nagtegaal, J., Parks, D. and Rice, J. (1974), “On numerically accurate finite element solutions in the fully plastic range”, *Comput. Methods Appl. Mech. Eng.*, Vol. 4, pp. 153–177.
- Park, J. and Kobayashi, S. (1984), “Three-dimensional finite element analysis of block compression”, *Int. J. Mech. Sci.*, Vol. 26(3), pp. 165–176.
- Pastor, F., Loute, E. and Pastor, J. (2009), “Limit analysis and convex programming: A decopositional approach of the kinematic method”, *Int. J. Numer. Methods Eng.*, Vol. 78, pp. 254–274.
- Ponter, A. and Carter, K. (1997), “Limit state solutions, based on linear elastic solutions with spatially varying elastic modulus”, *Comput. Methods Appl. Eng.*, Vol. 140, pp. 237–258.
- Ponter, A., Fuschi, P. and Engelhardt, M. (2000), “Limit analysis for a general class of yield conditions”, *European J. Mech. A/Solids*, Vol. 19, pp. 401–421.
- Puzrin, A. and Randolph, M. (2003), “Generalized framework for three-dimensional upper bound limit analysis in a Tresca material”, *J. App. Mech. ASME*, Vol. 70, pp. 91–100.

- Rankine, W. (1857), “On the stability of loose earth”, *Phil. Trans. R. Soc.* .
- Saleçon, J. (1967), “Théorie des charges limites: poinçonnement dune plaque par deux poinçons symétriques en déformation plane.”, *Comptes Rendus Mécanique, Académie des Sciences Paris* , Vol. 265, pp. 869–872.
- Salgado, R., Lyamin, A., Sloan, S. and Yu, H. (2004), “Two and three-dimensional bearing capacity of foundations on clay”, *Géotechnique* , Vol. 54, pp. 297–306.
- Sloan, S. (1988), “Lower bound limit analysis using finite elements and linear programming”, *J. Numer. Anal. Methods Geomech.* , Vol. 12, pp. 61–77.
- Sloan, S. (1989), “Upper bound limit analysis using finite elements and linear programming”, *J. Numer. Anal. Methods Geomech.* , Vol. 13, pp. 263–282.
- Smith, C. (2011b), “Derived lower bounds from DLO”, *unpublished* .
- Smith, C. (2012), “Identification of rotational failure mechanisms in cohesive media”, *unpublished* .
- Smith, C. and Cubrinovski, M. (2011a), “Pseudo-static limit analysis by discontinuity layout optimization: Application to seismic analysis of retaining walls”, *Soil Dyn. Earthq. Eng.* , Vol. 31, pp. 1311–1323.
- Smith, C. and Gilbert, M. (2007), “Application of discontinuity layout optimization to plane plasticity problems”, *Proc. R. Soc. A* , Vol. 463, pp. 2461–2484.
- Sokolovski, V. (1965), *Static of soil media*, New York, UK: Pergamon Press.
- Tamura, T., Kobayashi, S. and Sumi, T. (1984), “Limit analysis of soil structure by rigid plastic finite element method”, *Soils Found.* , Vol. 24, pp. 34–42.
- van Rij, H. and Hodge, P. (1978), “A slip model for finite-element plasticity.”, *ASME J. Appl. Mech.* , Vol. 45, pp. 527–532.
- Vicente da Silva, M. and Antão, A. (2007), “A non-linear programming method approach for upper bound limit analysis”, *Int. J. Numer. Methods Eng.* , Vol. 72, pp. 1192–1218.

-
- Vicente da Silva, M. and Antão, A. (2008), “Upper bound limit analysis with a parallel mixed finite element formulation”, *Int. J. Solids Struct.* , Vol. 45, pp. 5788–5804.
- Yu, H., Sloan, S. and Kleeman, P. (1994), “A quadratic element for upper bound limit analysis”, *Eng. Comput.* , Vol. 11, pp. 195–212.
- Zouain, N. and Herskovits, J. (1993), “An iterative algorithm for numerical limit analysis with nonlinear yield functions”, *Int. J. Solids Struct.* , Vol. 30, pp. 1397–1417.

A Sign convention for jumps in displacement

In DLO, the optimization problem is formulated purely in terms of the displacement jump across a set of potential discontinuities. This requires a consistent sign convention to be adopted. Figure A.1(a) shows two triangular prisms separated by a discontinuity ABC and with absolute displacements \mathbf{v}_1 and \mathbf{v}_2 respectively. The displacement jump $\Delta\mathbf{v}_{ABC}$ across discontinuity ABC must equal either $\mathbf{v}_1 - \mathbf{v}_2$ or $\mathbf{v}_2 - \mathbf{v}_1$. Using the ‘right hand screw rule’, the normal \mathbf{n} to the discontinuity can be determined for a particular ordering of the vertices as demonstrated in Figures A.1(b & c) for discontinuity ABC . $\Delta\mathbf{v}_{ABC}$ is simply defined as $\mathbf{v}_+ - \mathbf{v}_-$, where \mathbf{v}_+ and \mathbf{v}_- are the velocities of the blocks on the \mathbf{n} positive and \mathbf{n} negative sides of the discontinuity respectively for a chosen ordering of the vertices. Any ordering of a particular discontinuity’s vertices is permitted provided this remains fixed throughout the analysis and adjacent vertices remain adjacent in the chosen ordering.

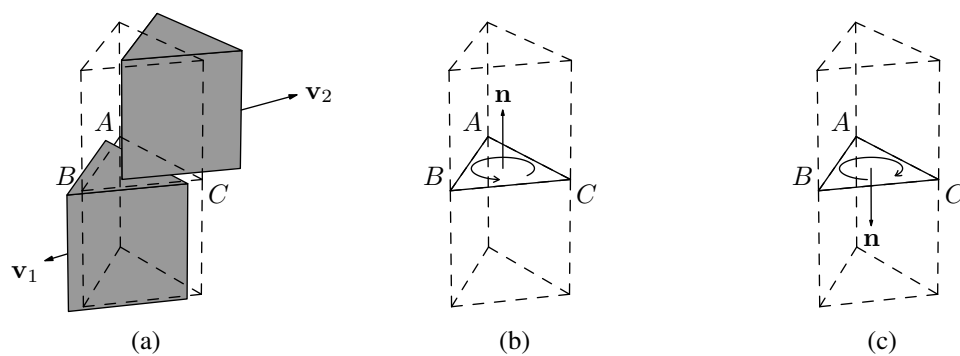


FIGURE A.1: Sign convention: (a) two triangular prisms separated by a discontinuity ABC , the dashed outline shows the prisms' original position; (b) discontinuity vertex ordering \overrightarrow{ABC} ; (c) discontinuity vertex ordering \overrightarrow{ACB} .

B Sign convention for compatibility

In general, a sign convention is necessary for equations (3.6) and (3.7) to be valid along edge j ; where $j = 1, 2, \dots, l$ and l is the total number of edges used to discretize the problem. Taking account of the sign convention these equations can be rewritten as follows:

$$\sum_{i \in S_j} k_{ij} \Delta \mathbf{v}_i = \mathbf{0}, \quad (\text{B.1})$$

$$\sum_{i \in S_j} k_{ij} \mathbf{T}_i \mathbf{d}_i = \sum_{i \in S_j} \mathbf{B}_{ij} \mathbf{d}_i = \mathbf{0} \quad (\text{B.2})$$

where S_j is the subset of all discontinuities meeting at edge j . $k_{ij} = \pm 1$ depends on the relative vertex orderings of discontinuity i and edge j .

Each discontinuity i ($i = 1, 2, \dots, m$) is defined by a subset D_i of the total nodes n ; where m is the total number of discontinuities and D_i contains the vertices of discontinuity i . Discontinuity i has a boundary formed by a subset K_i of the total number of edges l . Each edge j ($j = 1, 2, \dots, l$) is defined by subset E_j of the total nodes n ; where E_j contains the two vertices of edge j . The following is a suitable convention for selecting k_{ij} for all edges j ($j = 1, 2, \dots, m$) and all discontinuities i ($i = 1, 2, \dots, m$).

- (i) For each discontinuity i ($i = 1, 2, \dots, m$) define a positive ordering of the vertices in D_i . The two vertices of each edge j ($j \in K_i$) must be adjacent in this ordering. The ordering defined is cyclical (the first vertex is adjacent to the last) and is also used to define \mathbf{n}_i (see Appendix A).

-
- (ii) For each edge $j(j = 1, 2, \dots, l)$ define a particular ordering of the vertices E_j as positive.
 - (iii) For each edge $j(j = 1, 2, \dots, l)$ and discontinuity $i(i \in S_j)$ with common vertices $\{X, Y\} = D_i \cap E_j$ compare the orderings of X and Y in the positive orderings of E_j and D_i defined in (i) and (ii), respectively, remembering that the ordering of D_i in (i) is cyclical. If these orderings coincide, $k_{ij} = 1$; otherwise, $k_{ij} = -1$.

C Crossovers & Overlaps

C.1 Crossovers

Intersections between discontinuities can occur, much like in plane strain problems. The intersections between discontinuities on different planes are line segments or ‘crossovers’. Compatibility is implicitly ensured at these crossovers rather than being explicitly enforced. This can be demonstrated using the two intersecting rectangular discontinuities, shown in Figure C.1(a). In Figure C.1(b), the discontinuities are split into smaller discontinuities so that the crossover is eliminated. In DLO it is assumed that the displacement jump across each of these smaller discontinuities is equal to that of its parent, taking account of the conventions in Appendices A and B. It is clear that equation (B.1) is satisfied for the new edges and the original crossover itself must also be compatible.

C.2 Overlaps

Intersections also occur between discontinuities in the same plane, resulting in ‘overlaps’. As with crossovers, compatibility is implicitly ensured. In Figure C.2(a), two overlapping discontinuities are shown. These are divided in Figure C.2(b) so that the original overlap is eliminated, but two overlapping discontinuities $\overrightarrow{I_1 I_3 I_4 I_2}^{ABC}$ and $\overrightarrow{I_1 I_3 I_4 I_2}^{DEF}$ remain. Discontinuities located on different planes and sharing edges AB , BC , EF and FD are similarly divided (not shown in Figure C.2). The displacement jump for each new discontinuity equals that of

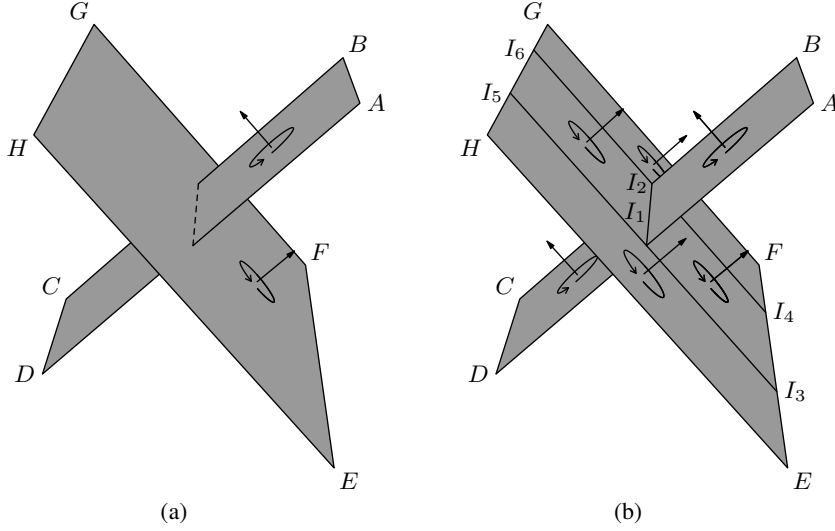


FIGURE C.1: Crossovers: (a) discontinuity \overrightarrow{ABCD} , displacement jump $\Delta \mathbf{v}_{ABCD}$, intersecting discontinuity \overrightarrow{EFGH} , displacement jump $\Delta \mathbf{v}_{EFGH}$; (b) \overrightarrow{ABCD} split into $\overrightarrow{ABI_2I_1}$ and $\overrightarrow{I_1I_2CD}$, both with a displacement jump $\Delta \mathbf{v}_{ABCD}$; \overrightarrow{EFGH} split into $\overrightarrow{I_1I_2I_6I_5}$, $\overrightarrow{I_3I_4I_2I_1}$, $\overrightarrow{EI_3I_1I_5H}$ and $\overrightarrow{I_4FGI_6I_2}$, all with a displacement jump $\Delta \mathbf{v}_{EFGH}$.

its parent discontinuity, taking account of the conventions in Appendices A and B. Using equation (B.1), it is simple to prove that compatibility is maintained and that the displacement jump $\Delta \mathbf{v}_I$ on the overlapping region $I_1I_3I_4I_2$ equals $\Delta \mathbf{v}_{ABC} + \Delta \mathbf{v}_{DEF}$.

Calculating p_{ABC} , p_{EDF} and p_I from equation (3.10), it is clear that $p_{ABC} + p_{DEF} \geq p_I$ since these terms are not added vectorially in the SOCP solver. It can, therefore, be concluded that overlaps will overestimate both the dilation and energy dissipated. This is equivalent to the overlapping region having a cohesive strength c and angle of friction ϕ greater than those of the original discontinuities, thus maintaining the upper bound nature of the solution. The solver will tend to avoid such overlaps where these result in more energy being dissipated. Therefore the significance of these overlaps is likely to reduce with increasing nodal resolution.

The load distribution across discontinuities ABC and DEF is unknown and can

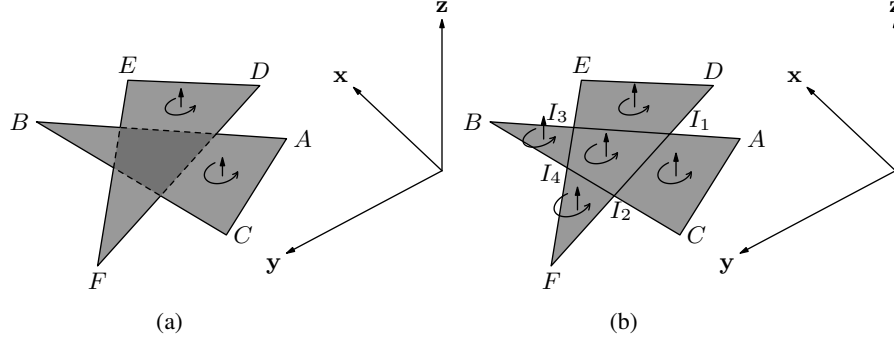


FIGURE C.2: Overlaps: (a) a discontinuity \overrightarrow{ABC} , displacement jump $\Delta\mathbf{v}_{ABC}$, overlapping a discontinuity \overrightarrow{DEF} , displacement jump $\Delta\mathbf{v}_{DEF}$; (b) \overrightarrow{ABC} split into $\overrightarrow{AI_1I_2C}$, $\overrightarrow{I_1I_3I_4I_2}^{ABC}$ and $\overrightarrow{I_3BI_4}$, each with a displacement jump $\pm\Delta\mathbf{v}_{ABC}$; \overrightarrow{DEF} split into $\overrightarrow{DEI_3I_1}$, $\overrightarrow{I_1I_3I_4I_2}^{DEF}$ (note there are two discontinuities $\overrightarrow{I_1I_3I_4I_2}$) and $\overrightarrow{I_2I_4F}$, each with a displacement jumps $\pm\Delta\mathbf{v}_{DEF}$.

be interpreted in any manner consistent with the work done by $\Delta\mathbf{v}_{ABC}$, $\Delta\mathbf{v}_{DEF}$ and $\Delta\mathbf{v}_I$. Note that the load on $I_1I_3I_4I_2$, L_I , cannot be the sum of the loads on $\overrightarrow{I_1I_3I_4I_2}^{ABC}$ and $\overrightarrow{I_1I_3I_4I_2}^{DEF}$, L_I^{ABC} and L_I^{DEF} respectively ($L_I \neq L_I^{ABC} + L_I^{DEF}$). Load distributions resulting in $L_I = L_I^{ABC} = L_I^{DEF}$ will always be consistent with the work done.

D Vector Calculus

D.1 Introduction

Vector calculus is a powerful mathematical toolbox used in Chapters 4 and 5 to derive the equilibrium formulation of discontinuity layout optimization (DLO) in two and three-dimensions, respectively. A basic introduction to the differential operators and theorems used in these derivations is presented in the following sections. Further background information can be found in James (1999).

A lower case letter or symbol with a normal typeface, for example f , will be used to represent a scalar function, unless otherwise indicated. A bold upper case letter or symbol, for example \mathbf{F} , will be used to represent a vector function. Two and three-dimensional vector functions are comprised of two or three components, respectively (see equations (D.1) and (D.2)).

$$\mathbf{F} = f_1\mathbf{i} + f_2\mathbf{j} \tag{D.1}$$

$$\mathbf{F} = f_1\mathbf{i} + f_2\mathbf{j} + f_3\mathbf{k} \tag{D.2}$$

Two-dimensional vector calculus differential operators will be presented in Section D.1.1. Three-dimensional vector calculus differential operators will be presented in Section D.1.2. Finally, vector calculus theorems applicable to both two and three-dimensions will be presented in Section D.1.3.

D.1.1 Two dimensional differential operators

The gradient of a two-dimensional scalar function f is a two-dimensional vector function given by equation (D.3).

$$\text{gradient of } f = \nabla f = \frac{\partial f}{\partial x} \mathbf{i} + \frac{\partial f}{\partial y} \mathbf{j} \quad (\text{D.3})$$

The divergence of a two-dimensional vector function \mathbf{F} is a scalar function given by equation (D.4).

$$\text{divergence of } \mathbf{F} = \nabla \cdot \mathbf{F} = \frac{\partial f_1}{\partial x} + \frac{\partial f_2}{\partial y} \quad (\text{D.4})$$

The curl of a two-dimensional vector function \mathbf{F} is a scalar function given by equation (D.5).

$$\text{curl of } \mathbf{F} = \nabla \times \mathbf{F} = \frac{\partial f_2}{\partial x} - \frac{\partial f_1}{\partial y} \quad (\text{D.5})$$

The line integral of a two dimensional vector function \mathbf{F} along a path AB can be found from equation (D.6).

$$\int_A^B \mathbf{F} \cdot d\mathbf{r} = \int_A^B f_1 dx + \int_A^B f_2 dy \quad (\text{D.6})$$

D.1.2 Three dimensional differential operators

The gradient of a three dimensional scalar function f is a three-dimensional vector function given by equation (D.7).

$$\text{gradient of } f = \nabla f = \frac{\partial f}{\partial x} \mathbf{i} + \frac{\partial f}{\partial y} \mathbf{j} + \frac{\partial f}{\partial z} \mathbf{k} \quad (\text{D.7})$$

The divergence of a three-dimensional vector function \mathbf{F} is a scalar function given by equation (D.8).

$$\text{divergence of } \mathbf{F} = \nabla \cdot \mathbf{F} = \frac{\partial f_1}{\partial x} + \frac{\partial f_2}{\partial y} + \frac{\partial f_3}{\partial z} \quad (\text{D.8})$$

The curl of a three-dimensional vector function \mathbf{F} is a three-dimensional vector function given by equation (D.9). Note that the three term is the curl of a two-dimensional vector in equation (D.5).

$$\text{curl of } \mathbf{F} = \nabla \times \mathbf{F} = \left(\frac{\partial f_3}{\partial y} - \frac{\partial f_2}{\partial z} \right) \mathbf{i} + \left(\frac{\partial f_1}{\partial z} - \frac{\partial f_3}{\partial x} \right) \mathbf{j} + \left(\frac{\partial f_2}{\partial x} - \frac{\partial f_1}{\partial y} \right) \mathbf{k} \quad (\text{D.9})$$

The line integral of a three-dimensional vector function \mathbf{F} along a path AB can be found from equation (D.10).

$$\int_A^B \mathbf{F} \cdot d\mathbf{r} = \int_A^B f_1 dx + \int_A^B f_2 dy + \int_A^B f_3 dz \quad (\text{D.10})$$

The surface integral of a three-dimensional vector function \mathbf{F} across a surface S , for example $y = y(x, z)$, can be found from equation (D.11); where $d\mathbf{S} = \mathbf{n} \cdot dS$ is the vector element of the surface area and \mathbf{n} is a unit vector normal to element S .

$$\iint_S \mathbf{F} \cdot d\mathbf{S} = \iint \left(-f_1 \frac{\partial y}{\partial x} + f_2 - f_2 \frac{\partial y}{\partial x} \right) dx dz \quad (\text{D.11})$$

D.1.3 Vector calculus theorems

The theorems presented in this section are applicable to both two and three-dimensional operators, unless otherwise indicated.

D.1.3.1 Gradient theorem

The line integral of a gradient along a path \overrightarrow{AB} can be found using the gradient theorem in equation (D.12).

$$\int_A^B \nabla f d\mathbf{r} = f(B) - f(A) \quad (\text{D.12})$$

D.1.3.2 Stokes' theorem

Stokes' theorem relates the integral of the curl of a function \mathbf{F} over a surface S to the line integral of \mathbf{F} along the surrounding closed path C via equation (D.13); where the symbol \oint indicates a closed path, $d\mathbf{S} = \mathbf{n} \cdot dS$ is the vector element of the surface area and \mathbf{n} is a unit vector normal to element S .

$$\iint_S \nabla \times \mathbf{F} \cdot d\mathbf{S} = \oint_C \mathbf{F} \cdot d\mathbf{r} \quad (\text{D.13})$$

In two-dimensions, Stokes' theorem becomes Green's theorem given in equation (D.14).

$$\iint_S \nabla \times \mathbf{F} \, dx dy = \oint_C \mathbf{F} \cdot d\mathbf{r} \quad (\text{D.14a})$$

$$\iint_S \left(\frac{\partial f_2}{\partial x} - \frac{\partial f_1}{\partial y} \right) dx dy = \oint_C f_1 dx + \oint_C f_2 dy \quad (\text{D.14b})$$

For a vector function $\mathbf{F} = \nabla f$, equation (D.15) must hold.

$$\iint_S \nabla \times \mathbf{F} \cdot d\mathbf{S} = \oint_C \nabla f \cdot d\mathbf{r} = 0 \quad (\text{D.15})$$

D.1.3.3 Gauss's theorem

The divergence (or Gauss's) theorem relates the integral of the divergence of a vector function \mathbf{F} over a volume V to the surface integrals integral over the surface S surrounding V via equation (D.16); where the symbol \oiint indicates a closed surface, $d\mathbf{S} = \mathbf{n} \cdot dS$ is the vector element of the surface area and \mathbf{n} is a unit vector normal to element S .

$$\oiint_S \mathbf{F} \cdot d\mathbf{S} = \iiint_V \nabla \cdot \mathbf{F} \, dV \quad (\text{D.16})$$

For a vector function $\mathbf{F} = \nabla \times \mathbf{F}_1$, equation (D.17) must hold.

$$\oiint_S \nabla \times \mathbf{F}_1 \cdot d\mathbf{S} = \iiint_V \nabla \cdot \mathbf{F} \, dV = 0 \quad (\text{D.17})$$

D.1.3.4 Miscellaneous relationships

$$\nabla \cdot (\nabla \times \mathbf{F}) = 0 \quad (\text{D.18})$$

$$\nabla \times (\nabla f) = 0 \quad (\text{D.19})$$

E Applying loads using functions \mathbf{P}^x and \mathbf{P}^y

E.1 Introduction

In the following appendix, the application of loads using functions \mathbf{P}^x and \mathbf{P}^y from Chapter 4 will be demonstrated. In many cases, loads are applied directly to an internal or external boundary (*i.e.* they are not body forces). An internal boundary is defined as a surface separating the problem domain into smaller bodies. External boundaries, on the other hand, are located on the boundary of the problem domain. In this appendix, the direct application of loads to internal and external boundaries will be explored. In addition, the application of body forces will be examined, confirming the summation in Section 2.6.2.4.

E.2 Loads applied to internal boundaries

Figure E.1(a) shows a problem domain comprising two bodies, P and Q , separated by an internal boundary AB ; where P and Q are bounded by closed paths M and N , respectively. Consider a load f^y applied in the positive y direction across AB to body P as shown in Figure E.1(b). This is distinct from the scenario shown in Figure E.1(c); where f^y is applied to Q . (Note that the scenario shown in Figure E.1(b) results in tensile stresses across AB ; while the scenario shown in Figure E.1(c) results in compressive stresses.)

f^y can be understood as the integral of the body force p_y across a body G (shown in Figure E.2) of length ds and infinitesimal width dt . (Note that $p_y = \nabla \times \mathbf{P}^y$, see equation (4.13)). Body G coincides with AB and is enclosed by an anticlockwise closed path $H = A'A''B''B'$.

$$\begin{aligned}
 f^y &= \iint_G p_y \, dx dy & (E.1) \\
 &= \iint_G \nabla \cdot \mathbf{P}^y \, dx dy \\
 &= \oint_H \mathbf{P}^y \, d\mathbf{r} \\
 &= \int_{A'}^{A''} \mathbf{P}^y \, d\mathbf{r} + \int_{A''}^{B''} \mathbf{P}^y \, d\mathbf{r} - \int_{B''}^{B'} \mathbf{P}^y \, d\mathbf{r} - \int_{B'}^{A'} \mathbf{P}^y \, d\mathbf{r}
 \end{aligned}$$

can be determined by applying equation (4.25) to G . Assuming \mathbf{P}^y changes only across the width dt and not along the length ds of G then $\int_{A'}^{A''} \mathbf{P}^y \, d\mathbf{r} = \int_{B'}^{B''} \mathbf{P}^y \, d\mathbf{r}$. Remembering the $A'B'$ must be the top boundary of Q and $A''B''$ the bottom boundary of P ; \mathbf{P}^y must equal \mathbf{P}_Q^y along $A'B'$ and \mathbf{P}_P^y along $A''B''$, resulting in

$$f^y = \int_{A''}^{B''} \mathbf{P}_Q^y \, d\mathbf{r} - \int_{A'}^{B'} \mathbf{P}_P^y \, d\mathbf{r}; \quad (E.2)$$

where \mathbf{P}_Q^y and \mathbf{P}_P^y are \mathbf{P}^y on Q and P , respectively. It can be concluded from equation (E.2) that load f^y can be applied by selecting appropriate values for \mathbf{P}_Q^y and \mathbf{P}_P^y . This will be demonstrated using some simple examples.

Assuming for simplicity that no body forces are applied to P and Q (*i.e.* $\nabla \cdot \mathbf{P}_Q^y = 0$ and $\nabla \cdot \mathbf{P}_P^y = 0$, see equations (4.12) and (4.13)), $y_A = y_B$ and $\varepsilon_Q^y = \varepsilon_P^y = 0$; $\mathbf{P}_Q^y = \omega_Q^y \mathbf{j}$ and $\mathbf{P}_P^y = \omega_P^y \mathbf{j}$. From equation (4.25), $\int_A^B \mathbf{P}_Q^y \, d\mathbf{r} = -\int_A^B \omega_Q^y \, dx$ and $\int_A^B \mathbf{P}_P^y \, d\mathbf{r} = -\int_A^B \omega_P^y \, dx$. (Note that as ds approaches zero, A' , A'' and B' , B'' approach A and B , respectively.)

Figure E.1(d) shows a choice of ω_Q^y and ω_P^y resulting in a load f^y on AB . (Note that $\omega_Q^y = f^y/(x_A - x_B)$ over shaped area and $\omega_Q^y = 0$ elsewhere.) From equation

(E.2) and Figure E.1(d),

$$\begin{aligned}
 f^y &= \int_{A'}^{B'} \mathbf{P}_Q^y \, d\mathbf{x} - \int_{A''}^{B''} \mathbf{P}_P^y \, d\mathbf{x} & (E.3) \\
 &= - \int_{A'}^{B'} \omega_Q^y \, dx + \int_{A''}^{B''} \omega_P^y \, dx \\
 &= -[x \cdot \omega_Q^y]_{A'}^{B'} + [x \cdot \omega_P^y]_{A''}^{B''} \\
 &= -(x_B - x_A) \cdot \omega_Q^y + (x_B - x_A) \cdot \omega_P^y \\
 &= (x_B - x_A) \cdot \frac{f^y}{(x_B - x_A)} - (x_B - x_A) \cdot 0 \\
 &= f^y - 0 = f^y.
 \end{aligned}$$

The loads f_P and f_Q in the y direction on P and Q , respectively, can be determined by applying equation (4.25) to P and Q , respectively.

$$\begin{aligned}
 f_P &= \iint_P \nabla \cdot \mathbf{P}^y \cdot d\mathbf{S} & (E.4) \\
 &= - \oint_M w^y \, dx + \oint_M \varepsilon^y \, dy \\
 &= - \int_A^B w^y \, dx - \int_B^F w^y \, dx - \int_F^E w^y \, dx - \int_E^A w^y \, dx
 \end{aligned}$$

and

$$\begin{aligned}
 f_Q &= \iint_Q \nabla \cdot \mathbf{P}^y \cdot d\mathbf{S} & (E.5) \\
 &= - \oint_N w^y \, dx + \oint_N \varepsilon^y \, dy \\
 &= - \int_B^A w^y \, dx - \int_A^C w^y \, dx - \int_C^D w^y \, dx - \int_D^B w^y \, dx.
 \end{aligned}$$

If ω_Q^y and ω_P^y have been chosen correctly then $f_P = f^y$ and $f_Q = 0$. w^y along AB , w_{AB}^y , could equal either ω_Q^y or ω_P^y . Assuming $\omega_{AB}^y = \omega_Q^y = -f^y/(x_B - x_A)$,

$$\begin{aligned} f_P &= -\int_A^B w^y dx - \int_B^F w^y dx - \int_F^E w^y dx - \int_E^A w^y dx \\ &= -\int_A^B \omega_Q^y dx - \int_B^F \omega_P^y dx - \int_F^E \omega_P^y dx - \int_E^A \omega_P^y dx \\ &= f^y - 0 - 0 - 0 \\ &= f^y \end{aligned}$$

and

$$\begin{aligned} f_Q &= -\int_B^A w^y dx - \int_A^C w^y dx - \int_C^D w^y dx - \int_D^B w^y dx \\ &= -\int_B^A \omega_Q^y dx - \int_A^C \omega_Q^y dx - \int_C^D \omega_Q^y dx - \int_D^B \omega_Q^y dx \\ &= -f^y(x_A - x_B)/(x_B - x_A) - 0 - 0 - f^y(x_D - x_C)/(x_B - x_A) \\ &= 0 \end{aligned}$$

thus proving this assumption correct. (Note that $x_A = x_C$ and $x_B = x_D$.)

The alternative field for w^y shown in Figure E.1(f) also satisfies $f_P = f^y$ and $f_Q = 0$ (note that $\omega_{AB}^y = \omega_Q^y = 0$); again this can be demonstrated by applying equation (4.25) to P and Q . Loads can be applied to internal boundaries in a similar manner using ε^y , ε^x and ω^x .

Numerous potential sub-paths are located within bodies Q and P ; \mathbf{P}_Q^y and \mathbf{P}_P^y will also be applied to these sub-paths. As demonstrated in Section 4.3.3, $\int \mathbf{P}^y d\mathbf{r}$ for a sub-path can be viewed as the force in the y direction applied on that sub-path. Therefore, it can be concluded that a load can only be applied to a body via an internal boundary by applying \mathbf{P}^x and \mathbf{P}^y not only to the internal boundary in question, but to all sub-paths located between the internal boundary and an external boundary. The choice of the external boundary is arbitrary as demonstrated by the fields in Figures E.1(d) and E.1(e).

To be consistent with the assumption of no body forces on P and Q , the load on closed paths (enclosing a sub-body) within P and Q must equal zero. For example, the forces on bodies U and V in Figure E.1(e) must equal zero. In fact, this is implicitly enforced and can be verified by applying equation (4.25) to U and W . Applying equations (4.25) to W , f_W must equal $f^y(x_H - x_G)/(x_B - x_A)$, where f_W is the load on W . In this case, f_W is entirely due to f^y and is, therefore, consistent with no body forces.

E.3 Loads applied to external boundaries

Figure E.3(a) shows a load f^y applied to a body P across an external boundary AB . Loads can be applied to AB by imagining a fictitious body E (shown in Figure E.3(b)). f^y can now be applied in much the same manner as described in Section E.2, assuming for simplicity that $y_A = y_B$. The loads f_P and f_E in the y direction on P and E , respectively, can be determined using equation (4.25). Figure E.3(d) shows a choice of ω_P^y and ω_E^y resulting in $f_P = f^y$ and $f_E = 0$. Alternative fields for ω^y applying f^y to AB are possible; however, the advantage of this field for ω^y is that no loading is applied to sub-paths within P as $\omega_P^y = 0$. Loads are applied to sub-paths within imaginary body E ; however, these can be ignored in any analysis (*i.e.* yield and equilibrium do not need to be checked).

E.4 Body forces

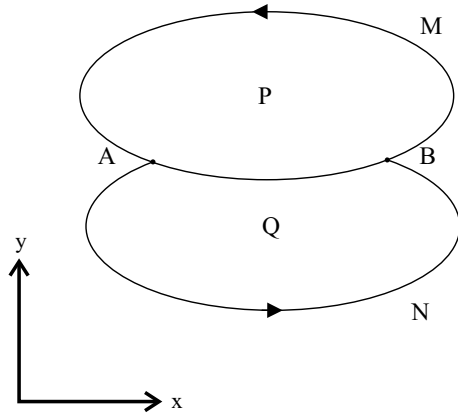
In many cases, loading results from body forces. Body forces can be readily be applied using functions $\mathbf{P}^x = \omega^x \mathbf{i} + \varepsilon^x \mathbf{j}$ and $\mathbf{P}^y = \varepsilon^y \mathbf{i} + \omega^y \mathbf{j}$, as demonstrated in the following example. Consider a column of material, shown in Figure E.4, bounded by a horizontal free surface YY' , a horizontal rigid surface CC' and two vertical rigid surfaces, AY and $A'Y'$. The column of material is split into three blocks, $YAA'Y'$, $ABB'A'$ and $BCC'B'$. A body force $p_y = \gamma$ due to gravity acts in the y

direction, where γ is the unit weight of the material. As a result, each block has an associated self-weight, w_1 , w_2 and w_3 , as shown in Figure E.4.

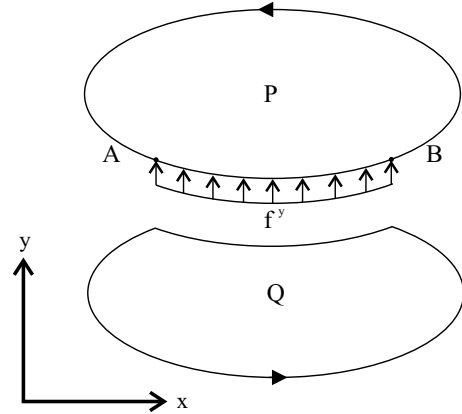
Self-weight can be applied by assuming $\omega^y = \gamma(y_Y - y)$ and $\varepsilon^y = 0$ across the column of material, y_Y is the y coordinate of YY' . In this case, equation (E.6) must be true and the self-weight of the individual blocks can be obtained by applying equation (4.25) to paths $YAA'Y'$, $ABB'A'$ and $BCC'B'$.

$$\begin{aligned} -\int_Y^{Y'} \omega^y dx = 0; & \quad -\int_A^{A'} \omega^y dx = w_1; & \quad -\int_B^{B'} \omega^y dx = w_1 + w_2; \\ & \quad -\int_C^{C'} \omega^y dx = w_1 + w_2 + w_3 \end{aligned} \tag{E.6}$$

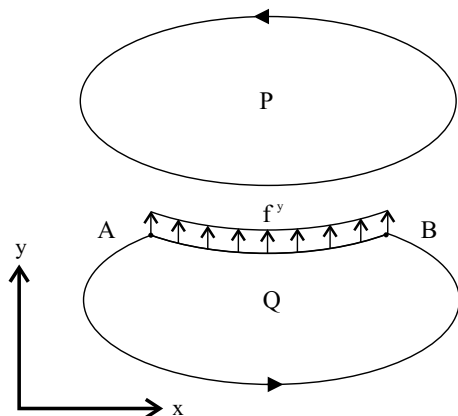
Setting the each of the integrals in equation (E.6) equal to $f_{D_i}^y$ and also setting $f_{D_i}^x = 0$, this clearly equivalent to the summation procedure described in Section 2.6.2.4 but in terms of global coordinates. The summation procedure could similarly be confirmed for loads applied to internal and external boundaries. However, the summation procedure becomes irrelevant for loads applied to external boundaries using fields such as that described in Section E.3 and Figure E.3(c).



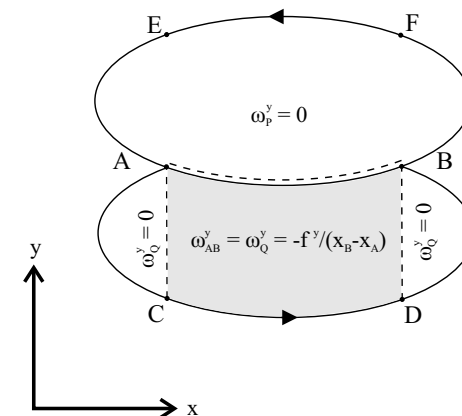
(a) Problem domain comprised of two bodies, P and Q , separated by internal boundary AB . Bodies P and Q are bounded by anticlockwise closed paths M and N , respectively.



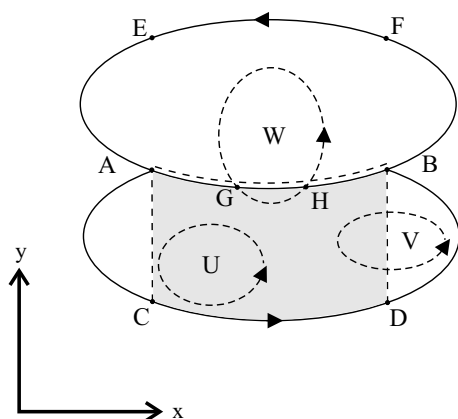
(b) Load f^y applied to P via AB .



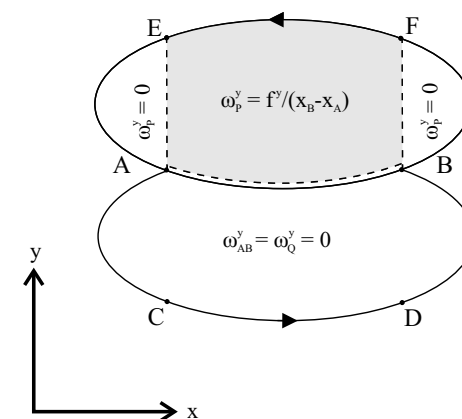
(c) Load f^y applied to Q via AB .



(d) Field ω^y applying f^y to P ; where ω_P^y , ω_Q^y and ω_{AB}^y are ω^y on P , Q and AB , respectively. (Note that $x_A = x_C$ and $x_B = x_D$.)



(e) Bodies U , V and V located within field ω^y in Figure E.1(d).



(f) Alternative field for ω^y applying f^y to P .

FIGURE E.1: Application of a load to an internal boundary

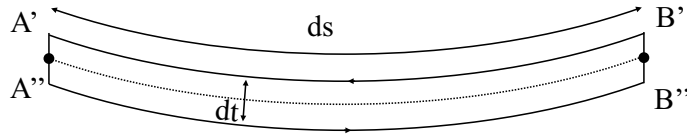
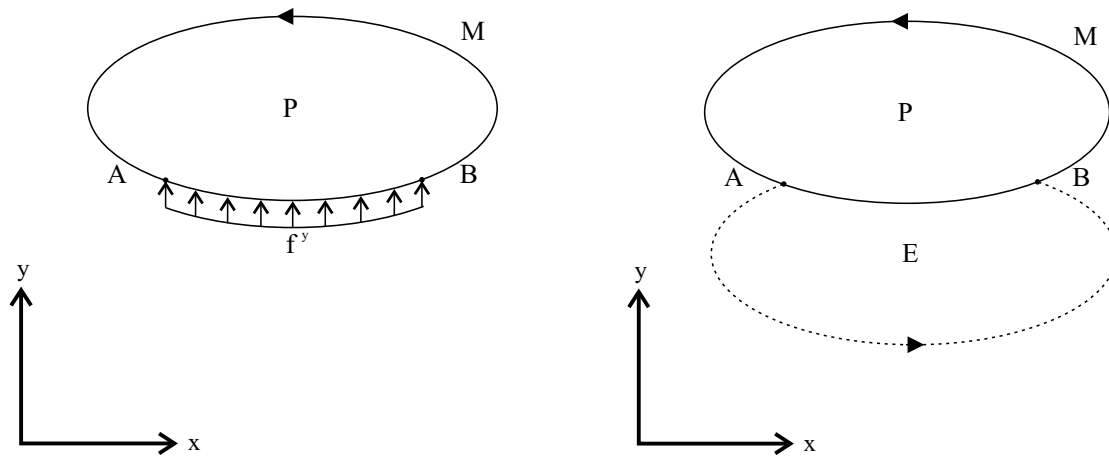
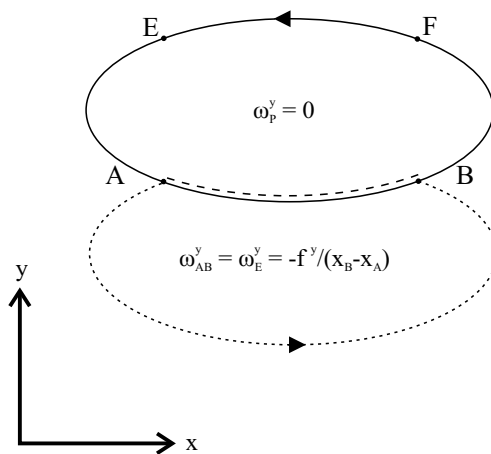


FIGURE E.2: Body G with length dt and infinitesimal width ds ; where G coincides with internal boundary AB and is bounded by a closed path $H = A'A''B''B'$.



(a) A load f^y applied to a body P surround by an external boundary M .

(b) A fictitious body E located below AB .



(c) Field for ω^y applying f^y to P ; where ω_p^y , ω_E^y and ω_{AB}^y are ω^y on P , E and AB , respectively.

FIGURE E.3: Application of a load to an external boundary

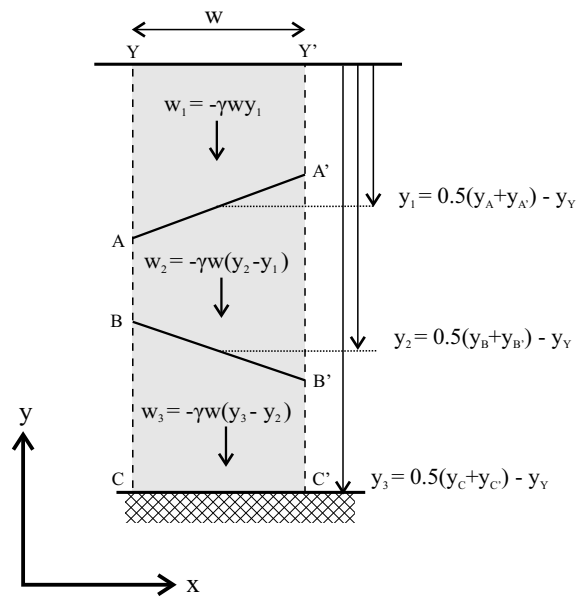


FIGURE E.4: Application of self-weight to a column of material

